

Exploring Tumbling Mill Dynamics Through Sensor Development

Sudarshan Martins

Doctor of Philosophy

Department of Mechanical Engineering

McGill University

Montreal, Quebec

May 9, 2011

A thesis submitted to McGill University in partial fulfillment of the requirements of
the degree of Doctor of Philosophy

© Sudarshan Martins 2011

DEDICATION

To Sonia Trudeau, Jacob Martins, Rachel Martins, David Martins, Oliver Martins and Grace Martins. Without you, these arms lack a purpose.

ACKNOWLEDGMENTS

I would like to express my gratitude to my supervisor, Peter Radziszewski, for his guidance and assistance. He brings out the best in students by fostering an environment where independence, teamwork, enthusiasm and creativity are welcome.

I must also acknowledge Wei Li, Arnaud Faucher, Sami Makni, Gary Savard, John Boisvert, Antonio Micozzi, Sam Minter, and David Speller for their invaluable assistance. Without their help, this work would not have been possible.

Finally, I thank my family for their love, support, patience and understanding. *Jamais je ne saurais exprimer toute ma gratitude.*

ABSTRACT

Though inefficient, tumbling mills play an important role in modern mineral processing. By virtue of the mill's action, the internal forces make instrumentation of the mill difficult. One solution to this problem is the use of an instrumented ball. An instrumented ball, equipped with an accelerometer, rotation rate sensors and a temperature sensor has been built. The instrumented ball and a camera system are used to measure the state of the charge within a laboratory mill. Also, a discrete element model (DEM) of the laboratory mill, a type of simulation, is written. From the distributions and moments of the energy terms of the charge (the material within the mill), the simulation and experimental results are analyzed and compared. The moments are used to tune the DEM, such that the simulation results are in agreement with the experimental results. A model order, a measure of DEM accuracy, is defined. Based on concepts borrowed from thermodynamics and statistical mechanics, mill entropy is calculated. Critical behavior, similar to a phase transition, is observed in the entropy, mean energy and energy fluctuation. From this, another definition of the critical speed is introduced. The critical speed of the mill is defined as the speed about which the entropy, mean energy and energy fluctuations exhibit critical behavior. Unlike other definitions, which rest on geometric and dynamic analyses of the charge, this new definition is based on distributions and moments. Finally, areas requiring more research and development are presented.

ABRÉGÉ

Bien qu'inefficace, les broyeurs jouent un rôle important dans la minéralurgie moderne. En vertu de l'action du broyer, les forces internes font en sorte que l'instrumentation du broyeur est difficile. Une solution à ce problème est l'utilisation d'un boulet instrumenté. Un boulet instrumenté, ayant un accéléromètre, des capteurs de vitesse de rotation et un capteur de température, est mis au point. Le boulet instrumenté et un système vidéo sont utilisés pour mesurer l'état de la charge (le matériel contenu par le broyeur) dans un moulin de laboratoire. Parallèlement, un modèle d'éléments discrets (DEM) du moulin, une sorte de simulation, est construit. À partir des distributions et des moments, tous dérivés des formes d'énergie de la charge, la simulation et les résultats expérimentaux sont analysés et comparés. Les moments sont utilisés pour ajuster la simulation, de sorte que les résultats de la simulation sont en accord avec les résultats expérimentaux. L'ordre du modèle, une métrique de précision pour les DEMs, est défini. Basée sur des concepts provenant de la thermodynamique et la physique statistique, l'entropie de la charge est calculée. Un comportement semblable à une transition de phase est observé dans l'entropie, la moyenne de l'énergie et la fluctuation de l'énergie. Sur ces résultats, une nouvelle définition de la vitesse critique est introduite. La vitesse critique du moulin est définie comme la vitesse à laquelle l'entropie, la moyenne de l'énergie ou la fluctuation de l'énergie ont un comportement de phénomène critique. D'autres définitions de la vitesse critique reposent sur des analyses géométriques et dynamiques de la charge;

cette nouvelle définition est basée sur les distributions et les moments. Enfin, des sujets nécessitant davantage de recherche et de développement sont présentés.

TABLE OF CONTENTS

DEDICATION	ii
ACKNOWLEDGMENTS	iii
ABSTRACT	iv
ABRÉGÉ	v
LIST OF TABLES	x
LIST OF FIGURES	xii
1	Introduction	1
	1.1 Mineral Processing	3
	1.2 Comminution	4
	1.2.1 Comminution Processes in Industry	5
	1.2.2 Comminution Efficiency	6
	1.3 Comminution Machines	8
	1.3.1 Crushing	9
	1.3.2 Grinding	9
	1.3.3 Tumbling Mills	10
	1.3.4 Charge Motion	12
	1.3.5 The Charge Filling of a Mill	15
	1.3.6 The Critical Speed of a Mill	16
	1.3.7 The Effect of Mill Parameters on Mill Performance	19
	1.3.8 Power Draw	20
	1.3.9 Instrumentation	25
	1.4 Research Goal	27
2	Literature Review and Objectives	29
	2.1 Introduction	29
	2.2 The Dunn and Martin Instrumented Ball	30

2.2.1	The Austin Reanalysis	35
2.3	The Rolf and Vongluekiet Instrumented Ball	40
2.4	The Gao and Thelen Instrumented Ball	47
2.5	The Rajamani, Delgadillo and Duriseti Instrumented Ball	56
2.6	Discrete Element Models	58
2.6.1	Geometry	59
2.6.2	Contact Detection	60
2.6.3	Contact Forces	61
2.6.4	Body Forces	62
2.6.5	Equations of Motion	62
2.6.6	Use of Discrete Element Models	63
2.7	Summary	70
3	Materials and Methods	72
3.1	Introduction	72
3.2	Instrumentation	72
3.2.1	Instrumented Ball	73
3.2.2	Instrumented Ball Electronics and Software	73
3.2.3	Instrumented Ball Shells	76
3.2.4	Video System	78
3.3	Laboratory Mill	80
3.3.1	Lifters	81
3.3.2	Mill Charge	82
3.4	DEM Simulations	83
3.5	Analysis	84
3.5.1	Physical Quantities	85
3.5.2	Statistics and Central Moments	86
3.5.3	Confidence in the Moments	89
3.5.4	Comparing Distributions	90
3.5.5	Comparative Study	91
3.5.6	Assumptions	93
3.6	Summary	94
4	Observations and Results	96
4.1	Instrumentation	96
4.1.1	Instrumented Ball	96
4.1.2	Camera System	99

4.2	Mill	100
	4.2.1 Spherical Charge Configuration	100
	4.2.2 Instrumented Ball	100
	4.2.3 Repeatability	101
	4.2.4 Cylindrical Charge Configuration	103
	4.2.5 Instrumented Ball	103
	4.2.6 CORSIM	111
	4.2.7 Instrumented Ball and CORSim	116
	4.2.8 Free Parameter DEM	117
4.3	Summary	130
5	Discussion	132
	5.1 Instrumentation, Measurands and Model Order	132
	5.2 Entropy and Energy Fluctuations	138
	5.3 Distributions	145
	5.4 Moments	146
	5.5 Summary	148
6	Conclusion	150
	6.1 Contribution to Knowledge	153
	6.2 Future Work	154
	References	157

LIST OF TABLES

<u>Table</u>	<u>page</u>
1-1 The ages of human history	2
1-2 Classification of comminution products by size	5
1-3 Comminution energy consumption	6
1-4 Teck Cominco annual milled tonnage	6
1-5 Energy consumption of mineral processing operations	7
1-6 The energy efficiency of size-reduction machinery	8
1-7 The annual consumption of products requiring grinding in their processing	9
1-8 The mill filling parameters	17
2-1 Grinding ball impact force and stress	35
2-2 Re-analyzed grinding ball impact force and stress	39
2-3 Estimated modulus of elasticity	39
2-4 Contact force and torque models	61
3-1 The properties of the instrumented disk	78
3-2 The properties of the aluminum instrumented ball	78
3-3 The properties of the aluminum instrumented box	78
3-4 The properties of the delrin instrumented ball	79
3-5 The properties of the delrin instrumented box	79
3-6 The properties of the spherical charge used during the 3D laboratory mill experiments	83

3-7	The properties of the cylindrical charge used during the 2D laboratory mill experiments	83
4-1	The rotation rate sensor noise characteristics	99
4-2	<i>In-Silico</i> energy rates-of-change statistics	101
4-3	The 2D mill parameters	103
4-4	<i>In-Situ</i> energy rates-of-change statistics	105
4-5	Initial CORSim model parameters	111
4-6	<i>In-Silico</i> energy rates-of-change statistics	113
4-7	<i>In-Situ</i> energy and power: mean, standard deviation and confidence limits	118
4-8	<i>In-Silico</i> (initial) energy and power: mean, standard deviation and confidence limits	119
4-9	Range of the simulation parameters	120
4-10	Best simulation parameters	123
4-11	<i>In-Silico</i> (best fit) energy and power: mean, standard deviation and confidence limits	127
5-1	The critical speeds of the laboratory mill	141
5-2	The skewness of the <i>in-situ</i> rotational kinetic energy, translational kinetic energy and potential energy	148

LIST OF FIGURES

<u>Figure</u>	<u>page</u>
1-1 The Antikythera Mechanism	2
1-2 Mineral processing	4
1-3 Comminution	5
1-4 Annual number of SAG and AG mills sold	10
1-5 Annual installed SAG and AG mill capacity	11
1-6 A tumbling mill	12
1-7 A typical tumbling mill charge motion	13
1-8 Examples of mill lifter profiles	14
1-9 Examples of installed mill lifter profiles	14
1-10 The charge motion as the speed of the mill increases	15
1-11 The charge filling of the mill	16
1-12 The critical speed of a mill	18
1-13 The Watanabe critical speed of a mill	19
1-14 The Hooke critical speed of a mill	20
1-15 The effect of lifter angle on the single particle trajectory	20
1-16 The effect of liners on the mill	21
1-17 Estimating the mill power draw	23
1-18 The torque arm model for estimating the mill power draw	24
1-19 An X-ray measurement system	26

2-1	A photograph of the Dunn and Martin instrumented ball	31
2-2	The Dunn and Martin instrumented ball	32
2-3	The Protect-A-Pack accelerometer	33
2-4	The grinding ball impact rate	34
2-5	The grinding ball impact rate reanalysis	38
2-6	The Rolf instrumented ball	42
2-7	The cumulative frequency distribution of the impact energy	43
2-8	The impact energy frequency distribution with lifters	44
2-9	The impact energy frequency distribution without lifters	45
2-10	The variation of the impact energy as the mill speed changes	46
2-11	The variation of the impact frequency as the mill speed changes	47
2-12	The Gao and Thelen instrumented ball	52
2-13	The frequency intensity of the impact energy at 40 percent critical speed	53
2-14	The frequency intensity of the impact energy at 100 percent critical speed	54
2-15	The impact frequency as a function of the mill speed	55
2-16	The Rajamani <i>et al.</i> instrumented ball	57
2-17	The alternative Rajamani mill instrumentation	58
2-18	The DEM calculation loop	59
2-19	The effect of the shape of the ball size distribution on the specific power consumption	65
2-20	Simulated power and observed power	66
2-21	Simulated power and observed power	67

2-22	Ball trajectories for 4 mill revolutions at 66 percent, 83 percent, and 93 percent critical speed	67
2-23	Percentage occupancy of a 2 mm rock particle for the mill rotating at 75 percent critical speed	68
2-24	DEM kinetic energy distributions	68
2-25	Experimental and DEM bin plots of selected components of particle velocity	69
3-1	The instrumented ball circuit	74
3-2	An opened instrumented ball	75
3-3	The instrumented ball software flowchart	77
3-4	The laboratory mill layout	81
3-5	The laboratory mill	82
3-6	The COREM DEM simulator	84
4-1	A verification of the rotation sensor	97
4-2	Time series of the rotation rate sensor noise	98
4-3	The cumulative distribution of the sensor noise	99
4-4	A picture of the operating mill with a measured instrumented ball trajectory overlay	100
4-5	The rotational kinetic energy distribution repeatability	102
4-6	The average experimental rotational kinetic energy of the instrumented ball at different mill speeds	103
4-7	The spatial distribution of the translational kinetic energy—instrumented ball	105
4-8	The spatial distribution of the rotational kinetic energy—instrumented ball	106
4-9	The spatial distribution of the potential energy—instrumented ball	107

4-10	The probability distribution of the time rate-of-change of the translational kinetic energy	108
4-11	The probability distribution of the time rate-of-change of the rotational kinetic energy	109
4-12	The probability distribution of the time rate-of-change of the potential energy	110
4-13	The spatial distribution of the translational kinetic energy—CORSim	112
4-14	The spatial distribution of the rotational kinetic energy—CORSim . .	113
4-15	The spatial distribution of the potential energy—CORSim	114
4-16	The probability distribution of the time rate-of-change of the translational kinetic energy	115
4-17	The probability distribution of the time rate-of-change of the rotational kinetic energy	115
4-18	The probability distribution of the time rate-of-change of the potential energy	116
4-19	The cumulative distribution of the translational kinetic energy	117
4-20	The cumulative distribution of the rotational kinetic energy	118
4-21	The cumulative distribution of the potential energy	119
4-22	Number of valid simulations for a given number of measurands	121
4-23	The simulated mean energies compared to the experimental results . .	124
4-24	The simulated energy standard deviations compared to the experimental results	125
4-25	The simulated and measured specific power	126
4-26	Cumulative distribution of the rotational kinetic energy with the CORSim best fit	127
4-27	Cumulative distribution of the translational kinetic energy with the CORSim best fit	128

4-28	Cumulative distribution of the potential energy with the CORSim best fit	129
5-1	Number of valid simulations for a given number of measurands	135
5-2	Fourier transform of the measured acoustic amplitude	136
5-3	Fourier transform of the simulated acoustic amplitude	137
5-4	Entropy estimate as the probability bin number is increased	139
5-5	An example of a phase transition—specific heat at constant volume of Argon	140
5-6	Simulation entropy, mean energy and total energy fluctuations as mill speed is increased	142
5-7	Cumulative distribution with the same mean and standard deviation .	147

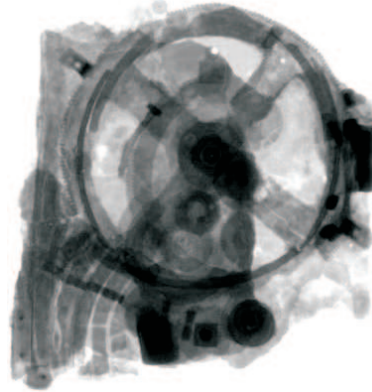
CHAPTER 1

Introduction

The study of human history does not rest on the discovery of human remains alone. It is also guided by the study of artifacts, objects manufactured, modified or shaped by human craft or culture. Since, at the moment of their creation, they reflect the state of technology and human thought, these artifacts, such as tools, documents, weapons, implements, utensils, buildings, and ornaments, complete the historical narrative, filling in what human remains cannot. The Antikythera Mechanism is an example of an important artifact (Figure 1–1). The Antikythera Mechanism, the world’s oldest known geared mechanism, was a sophisticated and intricate bronze astronomical clock and calendar—a portable mechanical planetarium, and possibly, the first analog computer [Wri07]. The mechanism seems to have been able to calculate and display celestial information such as the phases of the moon, predict lunar and solar eclipses, and display planetary positions. The Mechanism is thought to date from between 150 and 100 BCE [FBM⁺06, Mor84]. Though constructed thousands of years ago, the device demonstrates sophisticated knowledge of the heavens. Yet, without the proper tools and *materials*, the construction of such a device would have been very difficult, if not impossible. The materials and methods used by humankind, such as in the creation of artifacts, are not static—they have changed over time, closely following the evolution and advancement of human thought. Such is the importance of the materials that the major periods of human



(a) A fragment of the Antikythera Mechanism [FBM⁺06]



(b) A radiograph of the Antikythera Mechanism [Mor84]

Figure 1–1: The Antikythera Mechanism

history are divided by the use of various minerals and metals [Gre01, Kap90, KH74] (Table 1–1).

Regardless of the age, metals and minerals play an important role. As the technology improves, a greater variety and a better quality of metals and minerals are available. In turn, better tools are manufactured. Since tools are often necessary to the acquisition of knowledge, better tools lead to a greater understanding of the

Table 1–1: The ages of human history

Historical Age	Historical Period ¹
Paleolithic Age	400000 to 10000 BCE
Neolithic Age	10000 to 8000 BCE
Copper Age	8000 to 3500 BCE
Bronze Age	3500 to 1400 BCE
Iron Age	1400 BCE to 1600 CE
Coal Age	1600 to 1850 CE
Petroleum Age	1850 to 1950 CE
Uranium Age	1950 to 2000 CE
Carbon Age	2000 to ? CE

¹The dates are approximations.

natural world. With the greater understanding comes improved technology. So the cycle continues [Kap90]. Mining and mineral processing are the main methods used to obtain the metals and minerals. As was the case in the past [Gre01], most modern minerals and metals are obtained in this fashion [Tec08, Bam00].

1.1 Mineral Processing

The general steps necessary to extract and concentrate minerals are shown in Figure 1–2 [Wil97, FH03, GY06]. There are three fundamental steps to this process: mining, liberation and concentration [Wil97]. *Mining* is the set of processes associated with the extraction of ores from the earth [Har92], liberation is the release of the mineral from the gangue, the worthless part of the ore. Of interest here, the liberation is accomplished by crushing and grinding. Collectively, these crushing and grinding processes are called comminution. Finally, concentration separates the mineral from the gangue, and valuable minerals from each other [Wil97, VW91]. The valuable mineral is processed and refined, whereas the gangue, which possesses a low economic value, is considered waste and must be disposed of.

Since the capital and operating costs of mineral processing are high, the processing choices are always driven by economic concerns. Consequently, mineral processors constantly strive to increase the economic value of the ore [Wil97], by seeking the most efficient processing circuit for each particular site, by selecting the most efficient machinery, and by adopting the most efficient methodology.

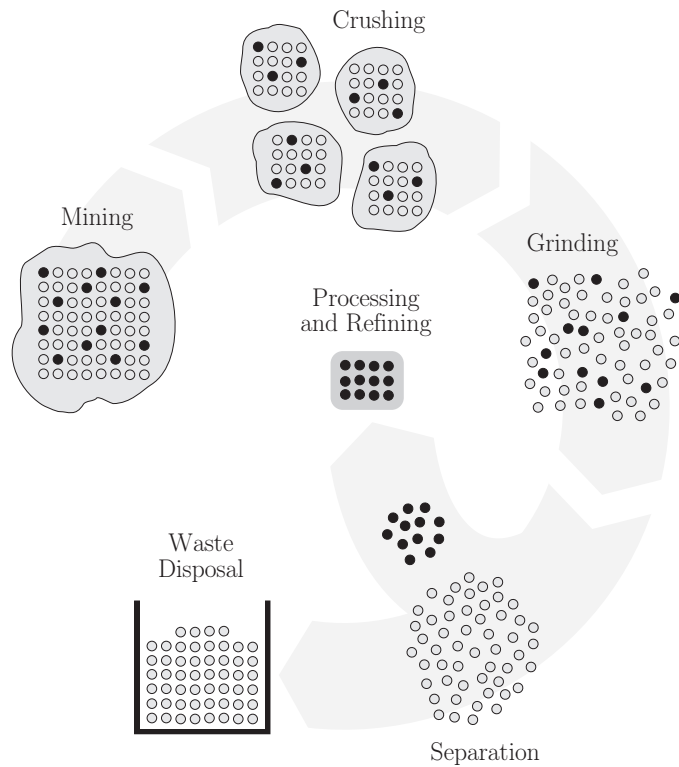


Figure 1-2: Mineral processing [FH03]

1.2 Comminution

Comminution is the process by which the application of a large stress causes a body to break into smaller bodies. It encompasses both crushing and grinding, and has the objective of physically freeing the valuable mineral from the gangue, the worthless part of the ore (Figure 1-3), at the coarsest possible particle size, while preserving the maximal recovery of materials during separation, processing and refining. The advantages of comminuting the ore to the optimal particle size are twofold. Firstly, less energy is used, since no energy is wasted in overgrinding. As shown in

Table 1–2: Classification of comminution products by size [Pra87]

Stage of reduction	Typical machine	Product size 80% passing (μm)	Specific energy (kWh/tonne)
Primary crushing	Compression or impact crusher	$10^6 - 10^5$	0.1 – 2
Secondary crushing	Compression or impact crusher	$10^5 - 10^4$	0.1 – 2
Coarse grinding	Rod mill	$10^4 - 10^3$	2 – 4
Fine grinding	Ball or vertical spindle mill	$10^3 - 10^2$	5 – 20
Very fine grinding	Tube mill	$10^2 - 10$	20 – 100
Super-fine grinding	Attrition or fluid energy mill	$10 - 1$	100 – 1000

Table 1–2, the smaller the desired ore particles, the greater the energy required. Secondly, subsequent separation stages are easier and cheaper to operate since particles have been reduced to a size appropriate for separation [Wil97].

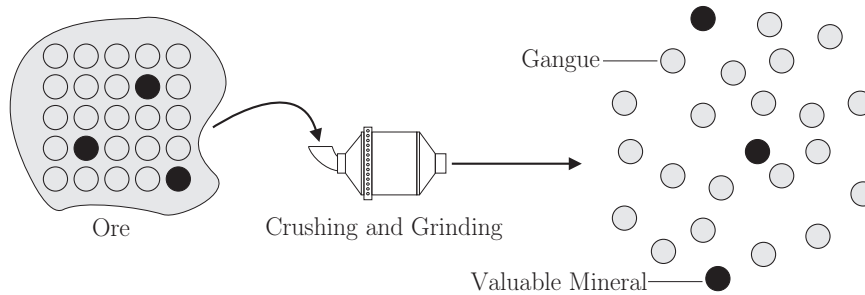


Figure 1–3: Comminution

1.2.1 Comminution Processes in Industry

A report of Canadian mining operations lists the operational configuration of a number of mineral concentrating plants [Bam00]. A selection of itemized operational power consumption values reveals the importance of comminution, and grinding in

particular, in mineral processing (Table 1–5). In the selected cases, 47 percent to 81 percent of the power is dedicated to comminution processes. A large percentage of this comminution power (67 percent to 90 percent) is used to grind the ore.

Furthermore, the annual milling tonnage of a Canadian mining and metals company underlines the scale of the operations (Table 1–4). Massive amounts of material are processed, requiring large amounts of power. The consumption of large amounts of energy is not limited to Canadian mineral processing plants. The scale of international operations is apparent in Table 1–3.

Table 1–3: Comminution energy consumption [Tro08]

Country	Annual Energy Consumption (2001)	
	Total, E_T (PJ)	Comminution (% of E_T)
USA	101.161×10^3	0.39
Canada	7.89×10^3	1.86
Australia	5.155×10^3	1.48
South Africa	5.159×10^3	1.80

1.2.2 Comminution Efficiency

Since comminution processes are resource intensive (Table 1–3), increasing their efficiency drives the research, design and operation of modern comminution processes. Nearly half of the operating costs of a mineral processing plant are associated with comminution processes [Wil97, RDD06, Che07], and they often represent more than

Table 1–4: Teck Cominco annual milled tonnage (000’s tonnes/yr) [Tec08]

Site	2007	2006	2005
Highland Valley Copper	42 593	45 356	50 666
Antamina	31 174	30 256	30 344
Duck Pond	205	-	-
Red Dog	3 381	3 238	3 087
Pogo	649	-	-
Williams and David Bell	3 036	3 355	3 503

Table 1–5: Energy consumption (kWh/t) of mineral processing operations (1997)
[Bam00]

Mount Polley Mine, Imperial Metals Corporation	
Crushing, conveying and screening	3.13
<i>Grinding</i>	<i>19.61</i>
Flotation	1.60
Thickening, dewatering, and drying	0.19
Pumping	0.58
Reclaim pumping	1.16
Compressors and blowers	1.60
Total	27.87
Troilus Project, Inmet Mining Corporation	
Crushing, conveying and screening	2.0
<i>Grinding</i>	<i>18.0</i>
Miscellaneous mill	6.0
Miscellaneous	6.0
Total	32.0
Timmins Operations, Kinross Gold Corporation	
Crushing, conveying and screening	7.6
<i>Grinding, classification</i>	<i>15.1</i>
Thickening, dewatering and drying	18.9
Lighting	3.7
Tailings	1.3
Fresh Water Pumps	1.3
Total	47.9
Gibraltar Mine, Boliden Westmin Limited	
Crushing, conveying and screening	1.865
<i>Grinding</i>	<i>7.015</i>
Flotation	1.127
Tailings	0.687
Mill building—general	0.940
Moly circuit	0.191
Fresh water pumps	1.089
Miscellaneous	3.436
Total	16.350

half of the capital costs [Wil97]. Moreover, comminution is inefficient. The average energy efficiency of comminution machinery is either less than 10 percent [SKSM05], less than 5 percent [Wil97], or may be as low as 1 percent [FA02]. Even if the 10 percent efficiency is assumed accurate, the individual efficiency of most comminution machines is low, as shown in Table 1–6.

Table 1–6: The energy efficiency of size-reduction machinery [SKSM05]

Equipment Class	Efficiency ($E_{\text{comminution}}/E_{\text{in}}$)
Jaw and roll crushers	0.7–0.9
Impact crushers	0.3–0.4
Roller-ring mills	0.007–0.15
Ball mills	0.05–0.1
Impact mills	0.1

Since energy consumption when milling may represent 85 percent of the total consumption of an open pit operation and 40 percent for an underground operation [RC04], and with the rising costs of energy, mineral processing companies have undertaken the work necessary to increase the energy efficiency of their facilities. Part of the research in this area has focused on the improvement of the performance and efficiency of their processes and technology [Tec08]. Due to the scale of the problem, as shown in Tables 1–4 and 1–5, research on grinding is an active area, with the goals of increasing the efficiency of grinding processes, understanding and characterizing the dynamics of grinding machinery [CR04].

1.3 Comminution Machines

There exists a number of comminution machines used in industry. Typically, they are defined by the nature of their action, a characteristic is strongly related to

Table 1–7: The annual consumption of products requiring grinding in their processing [LR05]

Product	1900	1930	1960	1990	2000
Gold (tons)	448	746	1049	2133	2576
Copper (millions of tons)	0.50	1.06	4.10	9.00	14.56
Coal (millions of tons)	780	1100	2000	3500	5300
Cement (millions of tons)	NA*	200	500	1000	1700
Wheat (millions of tons)	NA*	145	220	592	594
Phosphate, US (millions of tons)	1.52	4.02	17.80	46.3	38.6

* NA = not available

the size of the ore they process, as suggested in Table 1–2. Generally, comminution machines are group within the following two families, crushers and grinders [Pra87]:

1.3.1 Crushing

Crushers are used during the early stages of mineral processing. In industry, this type of device is applied to ores large that $10^4 \mu m$ (Table 1–2), and reduces the size of the ore by impact and compression. This class of comminution device includes compression rollers, jaw crushers, hammer mills, gyratory and cone crushers.

1.3.2 Grinding

Generally, grinding mills comprise the last stages of the comminution process. At this point in the processing, the ore prepared by the crushing stage is further reduced by the grinding circuit (Table 1–2). Here, the principal reasons for grinding are *a*) to liberate the important material from the unrequired constituents of a mixture, in preparation for the separation of the ore; *b*) to expose a large surface area per unit mass of a material in order to promote reactivity; and *c*) to reduce the material to the desired form [RS58]. As listed in Table 1–7, many materials require grinding in their processing. An extrapolation of these data suggests that the tonnage of materials requiring grinding is expected to increase in the near future. The grinding

circuit is composed of a several types of machinery, such as grinding rolls, stirred mills, hammer mills, vertical mills, and tumbling mills [Wil97]. The tumbling mill is one of the most used in industry, as illustrated by Figures 1–4 and 1–5.

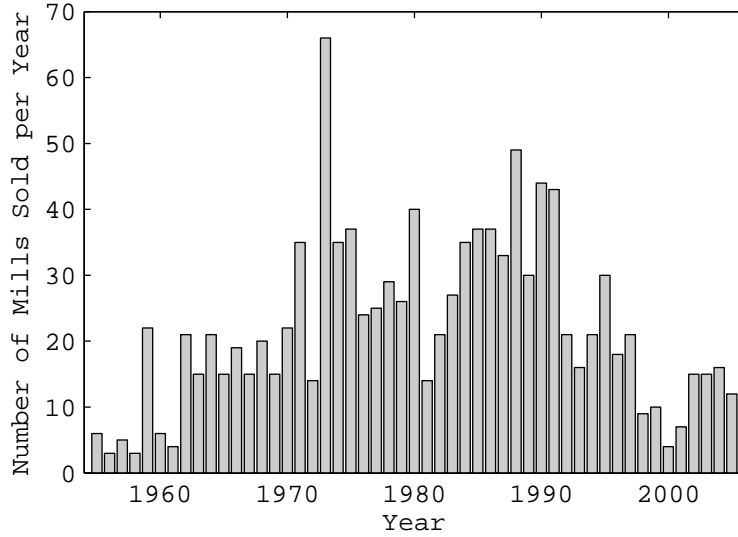


Figure 1–4: Annual number of SAG and AG mills sold [Jon06]

1.3.3 Tumbling Mills

The tumbling mill (Figure 1–6) is a rotating cylindrical shell filled with a charge, a heterogeneous mixture of ore—or whatever material is to be reduced in size—and, in many cases, water. The charge enters the mill at the feed end and exits at the discharge. Due to the rotation, the charge is lifted towards the shoulder, the point at which the charge material separates from the mill shell (Figure 1–7) [PM04]. From the shoulder, the charge drops towards the toe, the zone of intersection where the tumbling charge impacts the material below. As the charge transits from the toe, back to the shoulder, it is subject to grinding forces. Throughout the cycle, the

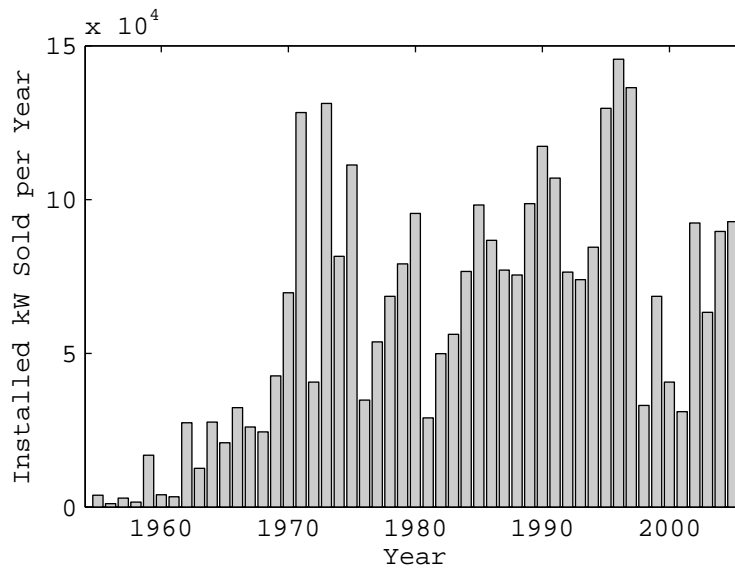


Figure 1-5: Annual installed SAG and AG mill capacity [Jon06]

charge is subject to both impact and grinding forces. The forces also affect the mill. To protect the shell from the comminutive action of the charge, a set of sacrificial plates are fixed to its inner surface. With some modification, liners can have a second purpose: to promote the circulation of the charge, thereby enhancing the action of the comminution processes upon the ore. These modified liners are called lifters. Examples of lifter geometries are illustrated in Figures 1-8 and 1-9.

Several types of tumbling mills exist. *Rod mills* are characterized by their use of long rods as the grinding media, whereas *ball mills*, unsurprisingly, use balls as their grinding media. *Autogenous mills* (AG mills) substitutes the ore for the grinding media, relying only on ore-ore interactions for the size reduction. To some degree, *Semi-autogenous mills* (SAG mills) operate in the same manner as autogenous mills.

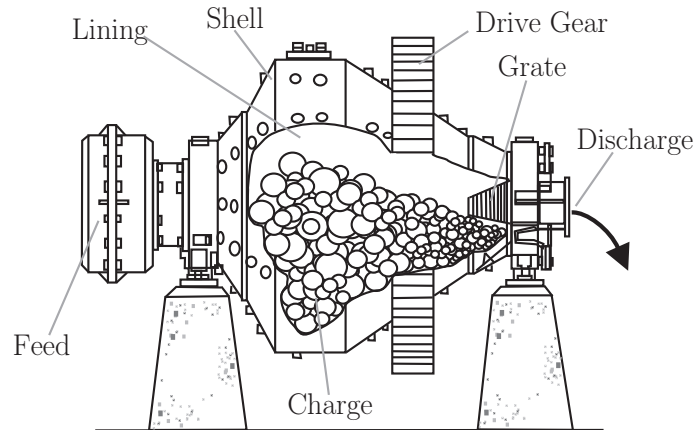


Figure 1–6: A tumbling mill [The08]

The difference lies with the addition of a small quantity of grinding media in semi-autogenous mills.

Mills can be operated either in a *batch* mode or a *continuous* mode. In a batch mode, a fixed quantity of charge is milled and subsequently discharged, When filling or discharging, the mill must be stopped. In continuous mode, the charge is added to the mill at the feed, is milled and exits at the discharge, without halting the operation of the mill.

1.3.4 Charge Motion

The modern grinding mill took form in the late 19th century. The ball mill was invented in Germany by Brückner in 1876 [Hab06]. With over a century of usage in industry [LR05], the theory of operation of the tumbling mill is well understood. The behavior of the charge defines a number of specific zones, where particular phenomena dominate [Rad99, RV84, YYMB08]. In a typical charge motion profile, the charge acts as follows: *i*) in the *flight zone*, the charge particles follow a parabolic

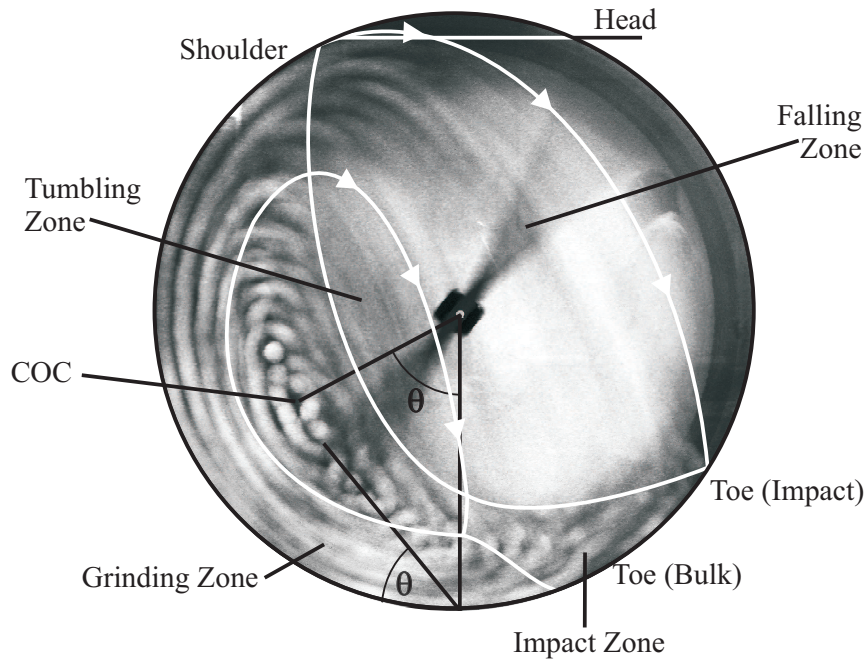


Figure 1-7: A typical tumbling mill charge motion

flight, under the influence of gravity; *ii*) in the *impact zone*, the falling particles re-enter the charge body, crushing the rock particles below at relatively high energy; *iii*) in the *grinding zone*, the charge layers slide over each other, grinding any trapped material; and, *iv*) in the *tumbling zone*, the charge rolls over itself, generating low energy breakage events. Also, a set of characteristic features (Figure 1-7), as defined by Powell and McBride, are useful for describing the behavior and characteristics of the charge in tumbling mills [PM04].

1. Shoulder: The uppermost point at which the charge material leaves the mill shell and enters the flight zone.

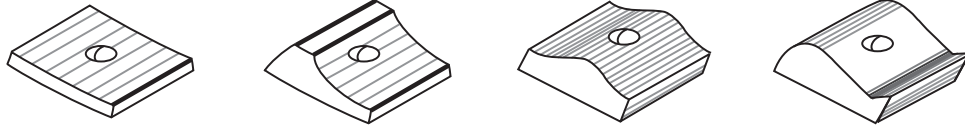


Figure 1–8: Examples of mill lifter profiles. From left to right: smooth lifters, differential wave lifters, wave lifters, and step lifters [Wil97].

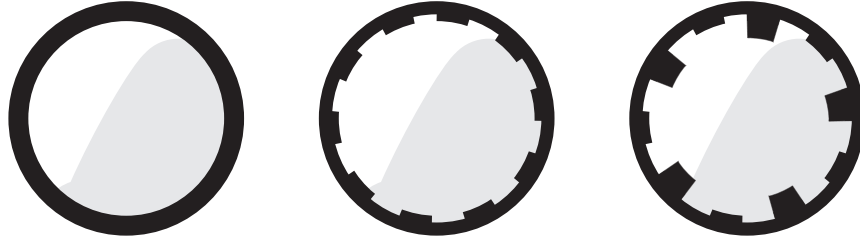


Figure 1–9: Examples of mill installed lifter profiles: smooth lifters (left), rectangular lifters (center), and hi/low lifters (right) [Rad97, Wil97]

2. Head: The highest point of charge trajectory.
3. Bulk Toe: The point of intersection of tumbling charge motion with mill shell. When the tumbling zone is extended towards the bottom of the charge, the point at which it intersects with the shell is the bulk toe.
4. Impact Toe: The highest point at which cataracting (flight zone) material strikes the mill shell
5. Angle of Repose: Cascade angle of the charge. It is equivalent to the angular position of the centre of circulation (Figure 1–7, angle θ).
6. Centre of Circulation (CoC): Axis about which all charge in the mill circulates.

Tumbling mill behavior depends on a large number of parameters: the rotational speed of the mill, the hardness of the ore, the filling of the mill, the length of the mill, the diameter of the mill, the solids to liquids ratio, etc [RS58]. Simply changing the speed of the mill results in very different charge dynamics, as is illustrated in

Figure 1–10. At low speeds, no flight of the charge is observed. At an intermediate speed, flight of the charge is present, with impacts playing a role in how the charge behaves. Finally, at high speeds, the charge undergoes centrifugal locking, and is, from the point of view of the mineral processor, a useless configuration.

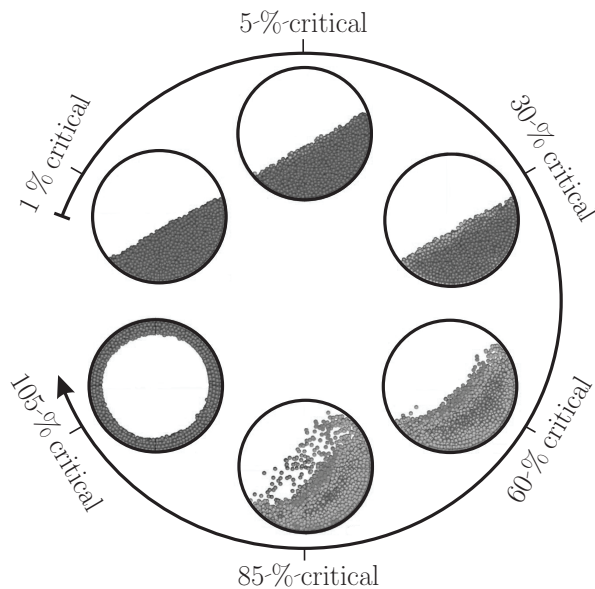


Figure 1–10: The charge motion as the speed of the mill increases [YYMB08].

1.3.5 The Charge Filling of a Mill

The quantity of material within the mill greatly affects the dynamics of the charge. This effect is best illustrated by the behavior of the charge at the two fill extremes. At very low fill levels, the charge will dwell at the bottom of the mill, experiencing small impact and grinding forces. If the mill is filled to capacity, preventing any addition of material, the behavior of the charge is different. Here, only small, local motion of the charge is possible; all other motion is inhibited by the tight-packing constraint. This effectively locks the charge in place, allowing it to

essentially rotate with the mill. At this fill level, the charge acts like a rigid body. Typically, the mill is not operated under these two conditions. An intermediate level of fill is often selected such that impact and grinding effects are present, and manifest themselves through the presence of impact, tumbling, grinding and falling zones.

The level of fill of the charge, or the fractional fill, J is defined as

$$J = \frac{V_{charge}}{V_{mill}} \quad (1.1)$$

the ratio of the charge volume, V_{charge} , including voids, to the mill volume, V_{mill} . In Table 1–8, the relationship between the fill, J , and a number of geometric measurements of the charge, as defined in Figure 1–11, are given.

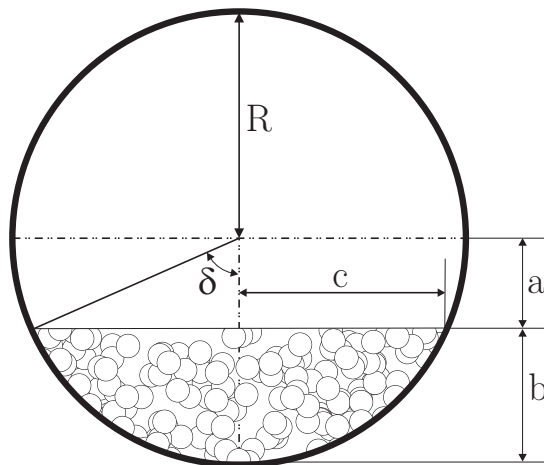


Figure 1–11: The charge filling of the mill [RS58].

1.3.6 The Critical Speed of a Mill

The critical speed is a characteristic speed associated with the mill. Several definitions of the critical speed exist. Rose and Sullivan [RS58] give the critical

Table 1–8: The mill filling parameters [RS58]

δ°	J	C/R	a/R	b/R
0	0.000	0.000	1.000	0.000
15	0.003	0.259	0.966	0.034
30	0.028	0.500	0.866	0.134
45	0.090	0.707	0.707	0.297
60	0.194	0.886	0.500	0.500
75	0.335	0.966	0.259	0.741
90	0.500	1.000	0.000	1.000
105	0.665	0.996	-0.259	1.259
120	0.804	0.866	-0.500	1.500
135	0.910	0.707	-0.707	1.707
150	0.972	0.500	-0.866	1.866
165	0.997	0.259	-0.966	1.966
180	1.000	0.000	-1.000	2.000

speed as the rotation rate of the mill at which an element of the charge, with a size r , remains in contact with the mill shell, with a radius R . In this case, the centripetal and gravitational accelerations balance at the highest point of the trajectory (Figure 1–12). The critical speed is

$$N_{c,Rose} = \sqrt{\frac{g}{R - r}} \quad (1.2)$$

Watanabe defines the critical speed as rotation rate at which all the elements in the charge are stationary [Wat99].

$$N_{c,Watanabe} = \sqrt{\frac{g}{R \sin\Theta_c \sqrt{1 - \alpha}}} \quad (1.3)$$

where Θ_c is the angle of repose of the charge, g is the gravitational acceleration, α is the volumetric fill fraction and R is the radius of the mill (Figure 1–13). From the

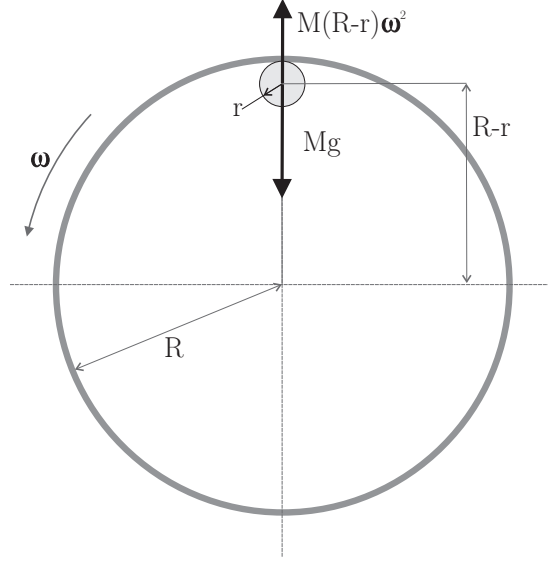


Figure 1–12: The critical speed of a mill

definitions, it is observed that

$$\frac{N_{c,Watanabe}}{N_{c,Rose}} \geq 1 \quad (1.4)$$

A third definition balances the frictional forces with the gravitational forces [Rad86].

$$N_{c,Hooke} = \sqrt{\frac{g}{\mu(R-r)}} \quad (1.5)$$

where μ is the friction coefficient of the charge/shell interface (Figure 1–14).

Finally, a definition of the critical speed, which is independent of the charge properties, is given by the following expression [Dav19],

$$N_{c,Davis} = \lim_{r \rightarrow 0} N_{c,Rose} = \sqrt{\frac{g}{R}} \quad (1.6)$$

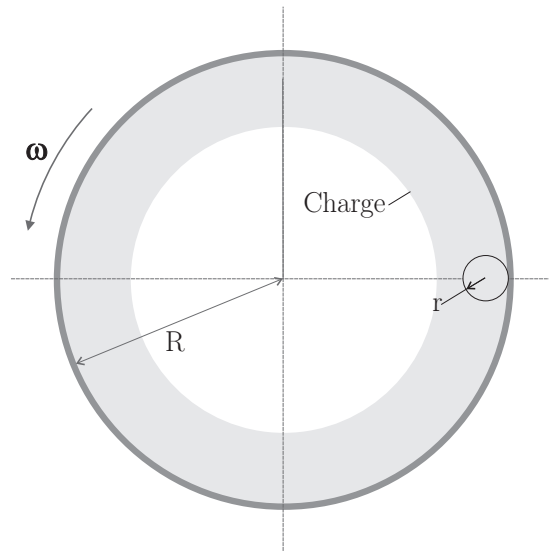


Figure 1–13: The Watanabe critical speed of a mill

$N_{c,Davis}$ represents the minimum possible critical speed, as defined by Rose, for any arbitrary charge, independent of particle size r . This definition of the critical speed is adopted here.

For tumbling mills, the rotation rate of the mill is not expressed as the rotation rate of the mill, ω_{mill} , but as a percentage of the critical speed,

$$N_{mill} = \frac{\omega_{mill}}{N_c} \times 100 \tag{1.7}$$

1.3.7 The Effect of Mill Parameters on Mill Performance

As stated in previous sections, many parameters have an effect on the dynamics of the charge. For example, a modification of the lifter angle give rise to changes in the particle trajectories (Figure 1–15). A change of the spacing-to-height ratio of the lifters produces changes in the power draw, as illustrated in Figure 1–16. The

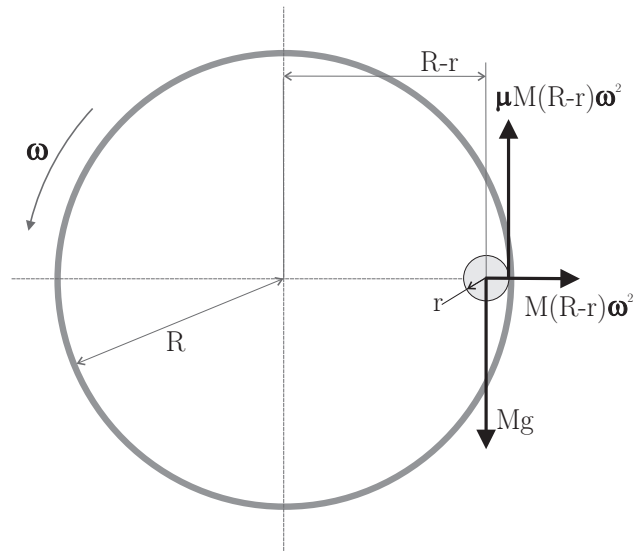


Figure 1-14: The Hooke critical speed of a mill

complex relationship between the parameters and the charge dynamics has long been the focus of grinding mill studies.

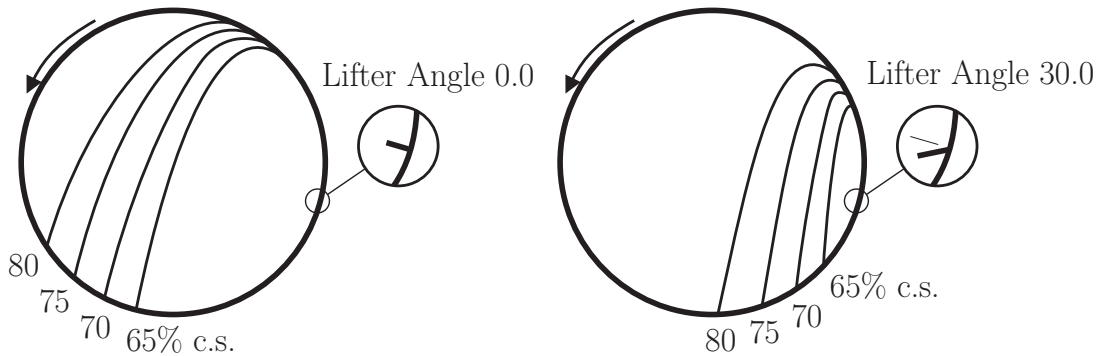


Figure 1-15: The effect of lifter angle on the single particle trajectory [McI83].

1.3.8 Power Draw

The power draw of the mill is controlled by the configuration of the charge and the internal dynamics[RS58]. The power required to drive a mill is expected to

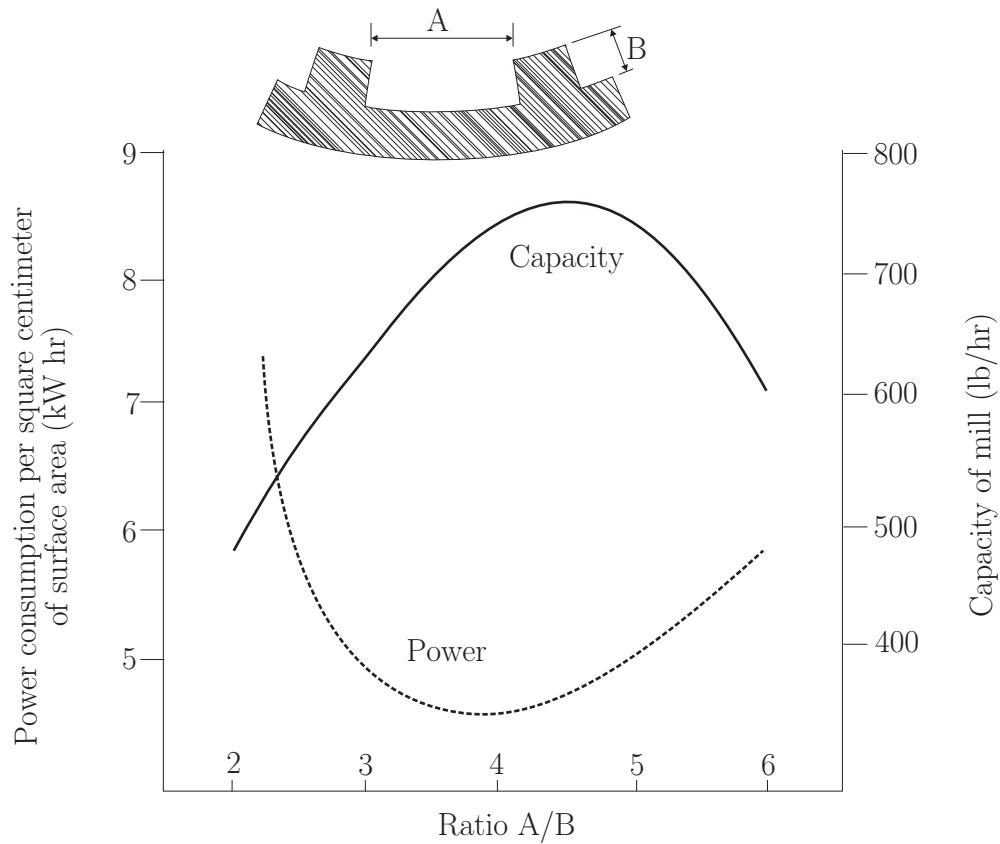


Figure 1-16: The effect of liners on the mill[HV86].

depend on the length of the mill, L , the diameter of the mill, D , the diameter of the balls, d , the density of the balls, ς , the fractional ball filling of the mill (the fraction of the total volume occupied by the charge, including voids), J , the rotation speed of the mill, N , the acceleration due to gravity, g , and the coefficient of restitution of the ball and mill materials, e . Furthermore, the mill power can be a function of the characteristic diameter of the particles, b , the energy required to produce a unit increase in the specific area of the ore, E , the fraction of the total volume occupied

by the powder including voids, V , the effective kinematic viscosity of the powder and fluid mixture within the mill, ν , the density of the mixture, ρ , and, in the case of wet milling, the ratio, by volume for the solids with respect to the liquid in the pulp, U . Finally, if lifters are used to promote the charge motion, the number of lifters, n , and the lifter height, h , play a role in the power draw [RS58].

$$P = \phi(L, D, d, \varsigma, J, N, g, f, e, b, E, V, \nu, \sigma, U, h, n) \quad (1.8)$$

Using dimensional analysis, Rose and Sullivan express the power as a function of dimensionless groups [RS58].

$$\begin{aligned} \left(\frac{P}{D^5 N^3 \varsigma}\right) = & \phi \left\{ \left(\frac{h}{D}\right), \left(\frac{L}{D}\right), \left(\frac{d}{D}\right), \left(\frac{g}{DN^2}\right), \left(\frac{b}{D}\right), \left(\frac{E}{D^3 N^2 \varsigma}\right), \right. \\ & \left. \left(\frac{\nu}{D^2 N}\right), \left(\frac{\sigma}{\varsigma}\right), (J), (f), (e), (V), (U), (n) \right\} \end{aligned} \quad (1.9)$$

Rose and Sullivan further reduce the power to the following expression:

$$\begin{aligned} \left(\frac{P}{D^5 N^3 \varsigma}\right) = & \left(1 + \frac{0.4\sigma}{\varsigma}\right) \cdot \left(\frac{L}{D}\right) \cdot \phi_1\left(\frac{Nc}{N}\right) \cdot \phi_3(J) \\ & \times \phi_4\left(\frac{d}{D}\right) \cdot \phi_5(n) \cdot \phi_6\left(\frac{h}{D}\right) \cdot \phi_9\left(\frac{b}{D}\right) \cdot \phi_{11}(V) \end{aligned} \quad (1.10)$$

where $\phi_1, \phi_3, \phi_4, \phi_5, \phi_6, \phi_9$ and ϕ_{11} are functions of a single dimensionless parameter that affects the power of the mill. The calculated mill power, as given by Equation 1.10, agrees with the observed power (Figure 1–17). Other methods of estimating the power involve the analysis of the ball charge dynamics, circumferential mass flow rates, and empirical results (Equation 1.11) [RBL⁺05, GY06].

$$\begin{aligned} P &= 3.627 \rho L D^{2.5} f(J) \\ P &= 3.627 \rho N_{mill} L D^{2.5} \sin^3 \theta \\ P &= 12.262 \rho L D^{2.3} J (1 - 0.937J) \left(1 - \frac{0.1}{29 - 10Nc}\right) \end{aligned} \quad (1.11)$$

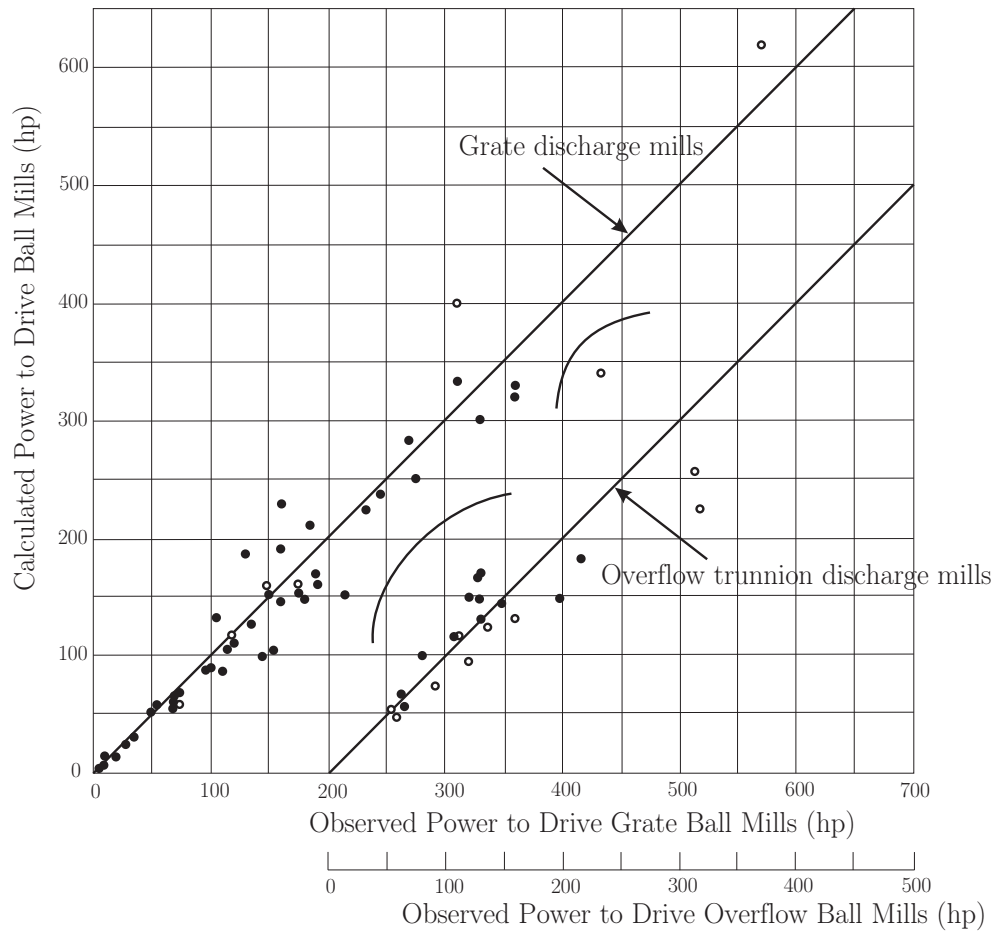


Figure 1-17: Estimating the mill power draw [RS58]

where ρ is the solid volume fraction in slurry, N_{mill} is the mill speed expressed as a fraction of the critical speed, N_c , L is the length of the mill, D is the diameter of the mill, θ is the toe angle of the mill, and J is the fractional filling of the mill.

A final method of calculating the mill power uses a torque-arm method, as illustrated in Figure 1-18. An applied torque is necessary to support the charge,

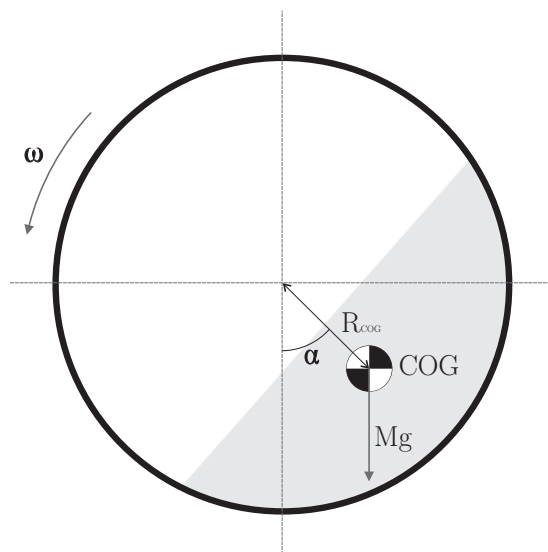


Figure 1–18: The torque arm model for estimating the mill power draw with a center of gravity offset from the rest position [RBL⁺05, DM03, GY06].

$$T = Mg R_{COG} \sin(\alpha) \quad (1.12)$$

where M is the mass of the charge, R_{COG} is the distance from the center of the mill to the center of gravity of the charge, g is the gravitational acceleration, and α is the angular offset of the charge, with respect to the rest position. The power required to maintain the applied torque is [GY06]:

$$P = T\omega_{mill} = Mg R_{COG} \sin(\alpha) \frac{N_{mill}}{100} N_c \quad (1.13)$$

where N_c is the critical speed of the mill and N_{mill} is defined by Equation 1.7. The torque-arm method does have some shortcomings. For instance, cascading, cataracting and frictional components have a complex relationship with the applied torque [FKV90]. The specific power required to maintain the charge in its position

is

$$p_M = \frac{P}{M} = g R_{COG} \sin(\alpha) \frac{N_{mill}}{100} N_c \quad (1.14)$$

The calculation of the power draw illustrates several points. Firstly, the mill performance is very complex and difficult to analyze. Often, simplifications are necessary, with empirical values playing an important role. Finally, the ease of calculation of the power, as defined by Equation 1.14, is an advantage, as long as the loss in accuracy is acceptable. This expression of the power is rewritten as,

$$p_M = g \bar{X}_{COG} \frac{N_{mill}}{100} N_c \quad (1.15)$$

where $\bar{X}_{COG} = R_{COG} \sin(\alpha)$ is the horizontal distance of the center of gravity of the charge from the rotation axis of the mill.

1.3.9 Instrumentation

Due to the complex nature of mill dynamics, measurement and characterization stand as preferred avenues to improving the understanding of what occurs within the mill [CR04]. To this aim, several instruments have been developed, such as microphone systems, thermocouples, load cells, and strain gauges [CR04]. Due to the harsh internal environment and some technical difficulties, few instruments have been designed to operate within the charge, or to measure bulk charge properties. This class of instrument must be able to either peer into the charge or move with the charge. Peering into the charge is difficult, but high energy particles and X-rays provide a solution, as pictured in Figure 1–19 [GPN01, CBBW⁺02, BGC⁺09, MGPC04]. Until the scalability of the instrument is demonstrated, a solution, applicable to small mills and pilot mills, is the construction of an instrumented ball, which is an electronics

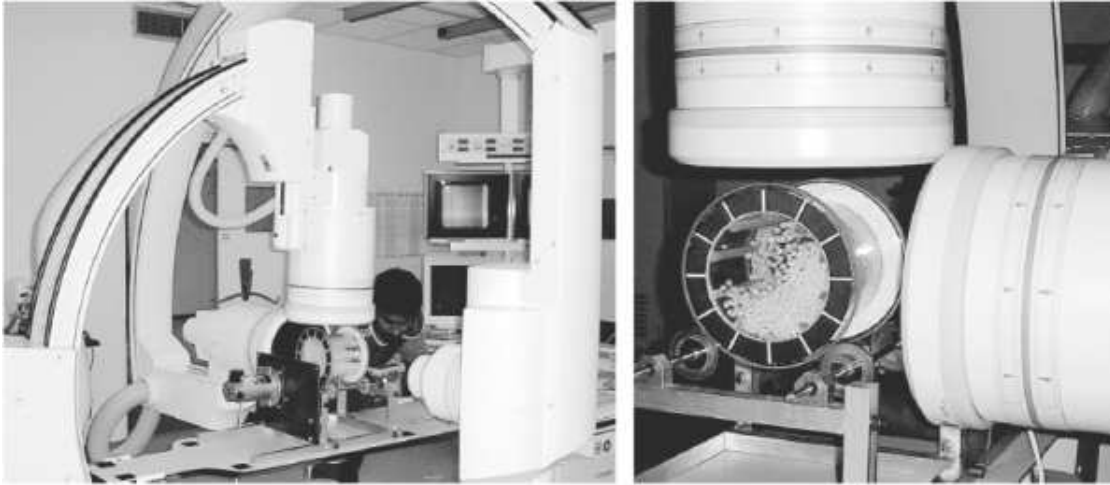


Figure 1-19: An X-ray measurement system. The person preparing the experiment (left) provides a scale of the image.

package protected by a rigid shell, thereby permitting its addition to the charge. By adding the instruments to the charge, the expectation is that the measurements will be representative of the dynamics since the instrument is subject to the same environment as the rest of the charge [CR04].

Not all instruments have a physical embodiment. Due to their many contributions to the understanding of mill dynamics, simulations of the charge motion are considered to be indirect instruments [CR04, CMM03, Cle04, Cle01a, Cle98, ZZRA08, Ach00, RM98, TR90, RBL⁺05, MC99, MR92, VR01, Mis03, RMVD00, MR94a]. When properly calibrated, a simulation can infer quantities that can be determined through measurement, and others that cannot be measured.

In the next chapter, the past instrumented balls are discussed and a general description of the discrete element method (DEM) simulations is given.

1.4 Research Goal

Though the history of mineral processing spans thousands of years, it remains one of humanity's cornerstone technologies. Without it, obtaining a number of the many modern materials would be difficult. A fundamental part of mineral processing is *comminution*, a collection of processes where a material is broken down through crushing and grinding, in preparation for the concentration of the minerals. This work is accomplished with the aid of a number of specialized machines such as *grinding mills*. Grinding mills operate by lifting the charge and dropping it back onto itself, by virtue of the rotation of the mill, thus creating impact and grinding forces. Such a system forms a rotating granular flow, with complex properties and behaviors, making predicting important quantities, like the power draw, difficult. Furthermore, the details of the internal dynamics of the charge are not well understood. The lack of instruments capable of operating within or peering into the charge is a factor limiting the understanding. With the ability to operate within the charge, instrumented balls are a class of instrumentation showing some promise. In conjunction with virtual instrumentation, the DEM simulations, the expectation is that the understanding of mill behavior will improve, benefiting mineral processors, through an improvement in efficiency of grinding mills.

Therefore, the goal is to develop a better understanding of tumbling mill dynamics through the development, use and validation of an instrumented sensor ball. First, this development is framed by the literature review of past instrumented ball

technologies. Current simulation methods are presented, as they offer another independent means of determining a wide set of states, comparable to what the instrumentation produces. This is followed by the description of the instrument and the methodology used to analyze the results. The results of the measurements are presented and, in certain cases, are set in parallel with the simulation results. Finally, an outline of the potential applications of the instrumented ball technology and its associated methodology is given.

CHAPTER 2

Literature Review and Objectives

2.1 Introduction

The search for understanding is based on the recursive, iterated and interlaced processes where one observes, proposes, tests, and predicts aspects of a system. For tumbling mills, a major weakness in understanding the system is the lack of instrumentation capable of operating within the charge—the observations are limited. A number of novel systems exist, with the purpose of observing aspects of the internal state of the charge. Example systems make use of X-rays [MGPC04] and positron emissions [BGC⁺09]. Unfortunately, the scalability of these devices is has not yet been demonstrated. Until it is possible to apply these techniques to a large mill, the best tools for the task remain the *instrumented ball* and, indirectly, *DEMs*. First, the objectives of this study are presented. In this work, the objectives are:

1. To show that an instrumented ball can be designed and built, with improved electronics;
2. To show that it is possible to obtain measurements from the mill interior, particularly measurements that are not impact forces;
3. To show that these measurements allow for a different type of analysis of the mill;
4. To show that the data are comparable to DEM simulation results;
5. To show that the data are helpful with regards to DEMs, as follows.

- (a) The instrument measurements can be used to verify that the DEM results accurately represent the system;
- (b) The instrument measurements can be used to tune the DEM simulations, enhancing their accuracy; and
- (c) The instrument measurements can be used to identify aspects of the DEMs in need of improvement.

As background to the work, the descriptions of the instrumented balls of (i) *Dunn and Martin*, (ii) *Rolf and Vongluekiet*, (iii) *Gao and Thelen*, and (iv) *Rajamani, Delgadillo and Duriseti* are presented. Since the DEMs, considered to be indirect instruments, are important tools in the understanding of tumbling mill dynamics, a brief description of the modeling is given.

2.2 The Dunn and Martin Instrumented Ball

Tumbling mills are designed to direct the comminution processes towards the charge—impacts must fracture the charge; abrasion must grind it down. Impacts due to falling grinding balls, rods or pebbles play an important role in the fine grinding of the ore. As this occurs within the mill, both the charge *and* the liner are subject to impact and abrasion.

In 1978, Dunn and Martin [DM78] designed an instrumented ball (Figure 2–1) to measure the impact forces in tumbling mills so that they may, in turn, be used to determine the stresses within the liners. Since the work was undertaken at the Climax Molybdenum Company, a producer of alloy steels used for components in mining equipment, the objective was to correlate the liner stresses with the service performance of mill liner alloys.

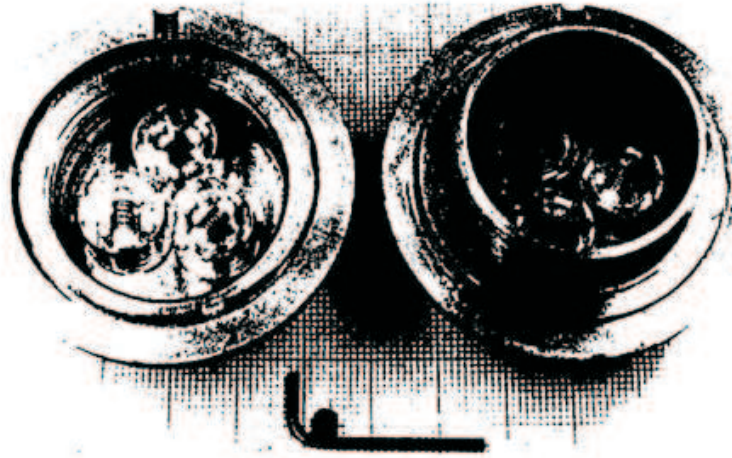


Figure 2-1: A photograph of the Dunn and Martin instrumented ball [DM78]

The Dunn and Martin instrumented ball (Figure 2-2) consists of two bored hemispheres. A pipe nipple fastens the two threaded hemispheres together. The cavity within the hemisphere can house six Protect-A-Pack accelerometers (Figure 2-3). A set of spring loaded steel balls constitute the heart of the accelerometer. When subject to an acceleration greater than the instrument rating, the accelerometer balls become dislodged, indicating that the rated acceleration had been exceeded [Rag07]. At the time of the study, the Protect-A-Pack accelerometers were available in ratings of 10 *g* to 500 *g*, in 10 *g* increments.

When placed within a mill, the Dunn and Martin instrumented ball experiences comminution forces, as does the rest of the charge. These forces will accelerate the instrumented ball. By direct observation of the accelerometers, it can be determined

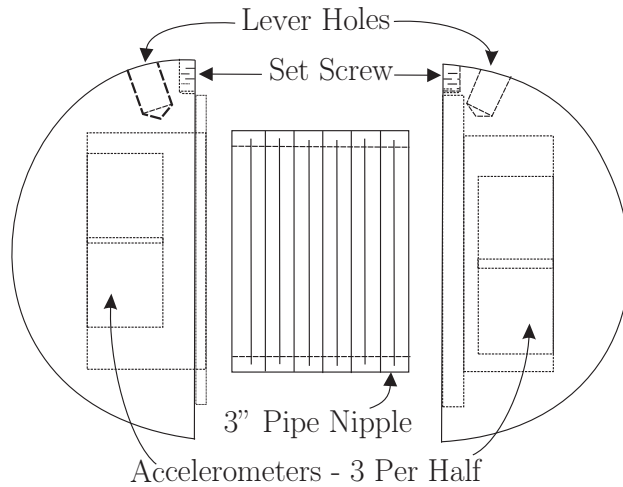


Figure 2–2: The Dunn and Martin instrumented ball [DM78]

if the instrumented ball is subject to accelerations greater than the Protect-A-Pack rating. By changing the rated Protect-A-Pack accelerometers, the maximum acceleration a , and consequently the maximum force P , applied on the instrumented ball, can be found, given the mass of the ball m .

$$P = ma \tag{2.1}$$

The forces applied to the instrumented ball are also interaction forces the it applies to either the rest of the charge or the mill liners. Therefore, the instrumented ball provides an estimate of the impact forces on mill liners due to grinding balls.

Hertzian theory develops expressions for compressive stress in the plane of contact between elastic materials. For the maximum compressive surface stresses in spheres and plates, the expressions are [DM78]:

$$\sigma_{sphere,plate} = 0.616 \left(\frac{FE^2}{D^2} \right)^{1/3} \tag{2.2}$$



Figure 2-3: The Protect-A-Pack accelerometer [Rag07]

$$\sigma_{sphere,sphere} = 0.616 \left(F E^2 \frac{D_1 + D_2}{D_1 D_2} \right)^{1/3} \quad (2.3)$$

where F is the impact force on the body, E is the modulus of elasticity, and D , D_1 and D_2 are the diameters of spheres. In this analysis, the modulus of elasticity and Poisson's ratio is the same for all bodies.

Prior to in-service tests, drop weight tests are used to determine the expected range of acceleration. The instrumented ball is dropped from a number of heights onto either bare liner steel or liner steel with a layer of sized ore. From these tests, a linear plot of the deceleration as a function of impact velocity is found (Figure 2-4). During in-service tests, the instrumented ball was used to measure the impact forces for three different mill types. Using the Hertzian expressions, the maximum calculated compressive stresses generated by ball-liner impacts are summarized in Table 2-1.

The results confirm the qualitative observations of the mill operators. The operation of the mill with ore does not generate impact stresses greater than the

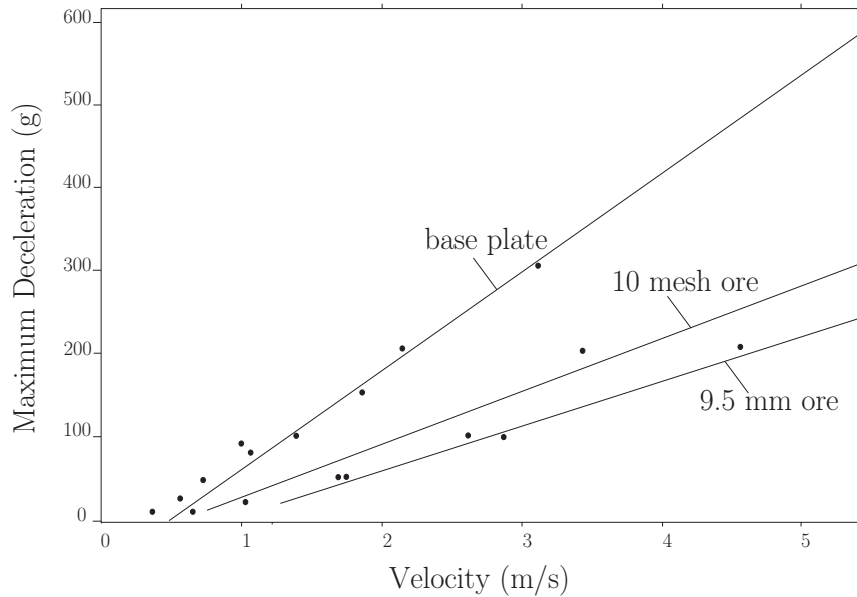


Figure 2-4: The grinding ball impact rate [DM78]

yield stress of the liner. Without the ore, the compressive stresses generated by ball-liner impacts equal or exceed the yield strength of iron and steel, damaging the liner and shortening its operational life. Consequently, Dunn and Martin suggest avoiding situations where the mill is operated without ore, such as intentional grind-outs, which clear the mill of product buildup. Additionally, the large mill results (Table 2-1, 8.53 m mill results) underline that the greater the mass of the grinding ball, the greater the Hertzian stresses on the liner. Therefore, Dunn and Martin stress the benefits of the use of grinding balls with the minimum mass necessary for the processing of the ore.

Dunn and Martin conclude that such testing on operating mills could identify situations detrimental to the operational life of the machine.

Table 2–1: Grinding ball impact force and stress [DM78]

Mill Diameter (m)		2.74	3.96	8.53
Mill Speed (rpm)		20	14.5	10.2
Mill Speed (percent critical speed)		78	66	69
Total Ball Drop (m)		2.03	2.28	6.39
Impact Velocity (m/s)		6.55	6.79	11.39
Ball Diameter (mm)		76	76	101, 127
Ball Weight (kg)		1.8	1.8	4.3, 8.4
Estimated Impact Deceleration (g)	with ore	350	380	650
	no ore	760	820	1 300
Estimated Impact Force (N)	with ore	6 230	6 760	27 500, 53 700
	no ore	13 500	14 600	54 900, 108 000
Hertzian Impact Stress (MPa)	with ore	2 200	2 270	2 980, 3 210
	no ore	2 850	2 920	3 760, 4 050

2.2.1 The Austin Reanalysis

A reanalysis of the Dunn and Martin results by Austin [Aus01] questions the initial findings. According to Austin, Hertzian theory gives the following decrease in distance between a sphere of radius, R_1 , impacting a surface with a radius of curvature R_2 :

$$z = \frac{r^2}{R} \quad (2.4)$$

where

$$\frac{1}{R} = \frac{1}{R_1} + \frac{1}{R_2} \quad (2.5)$$

and the radius of the contact circle r is

$$r = \left[\frac{3}{4} F R \left(\frac{1 - \nu_1^2}{E_1} + \frac{1 - \nu_2^2}{E_2} \right) \right]^{1/3} \quad (2.6)$$

where F is the compressive impact force, ν_i is the Poisson ratio of the i th body, E_i is the young's modulus of the i th body. To simplify the equations, the constant K

is defined as,

$$K = \frac{3}{4}R \left(\frac{1 - \nu_1^2}{E_1} + \frac{1 - \nu_2^2}{E_2} \right) \quad (2.7)$$

From Equations 2.4, 2.6 and 2.7, the expression for the compressive impact force becomes

$$F = z^{3/2} \frac{R^{3/2}}{K} \quad (2.8)$$

The energy absorbed as reversible strain energy, J , is

$$J = \int_0^z F dz = \frac{2}{5} \frac{R^{3/2}}{K} z^{5/2} \quad (2.9)$$

When the sphere impacts the surface, the strain energy comes from the decrease in the kinetic energy of the sphere. The maximal loss in kinetic energy gives the largest strain energy, which in turn, generates the largest force. The strain energy, J , as a function of the kinetic energy loss, is

$$J = \frac{1}{2}MV^2 - \frac{1}{2}Mv^2 \quad (2.10)$$

where M is the mass of the sphere, V is the initial velocity of the sphere, and v is the final velocity of the sphere. The maximal strain energy occurs when $v = 0$,

$$J_{max} = \frac{1}{2}MV^2 \quad (2.11)$$

With Equations 2.9 and 2.11, the maximum compression, z_{max} , is

$$z_{max} = \left(\frac{M}{2C} \right)^{2/5} V^{4/5} \quad (2.12)$$

and the maximum compressive force, F_{max} , is

$$F_{max} = \frac{(Rz_{max})^{3/2}}{K} \quad (2.13)$$

where the constant, C , is defined as

$$C = \left(\frac{2}{5K}\right) R^{3/2} \quad (2.14)$$

The maximum deceleration, a_{max} occurs at z_{max} ,

$$a_{max} = \frac{F_{max}}{M} = \left(\frac{R^{3/2}}{KM^{2/5}}\right) \left(\frac{1}{2C}\right)^{3/5} V^{6/5} \quad (2.15)$$

With the above modifications, Austin observes that the plot of the deceleration as a function of impact velocity (Figure 2-4) may not be linear. Instead, as given by Equations 2.13 and 2.15, the maximum force is function of $V^{6/5}$ (Figure 2-5). Furthermore, the linear functions used by Dunn and Martin (Figure 2-4) do not pass through the origin, which is unphysical. Using Equations 2.13 and 2.15, Austin recalculates the results presented by Dunn and Martin. The new results are presented in Table 2-2 (*cf.* Table 2-1). Furthermore, assuming that Poisson's ratio is the same for both materials, the effective Young's modulus, E , defined by

$$\frac{1}{E} = \frac{1}{E_1} + \frac{1}{E_2} \quad (2.16)$$

can be calculated. By solving for E in Equation 2.13,

$$E = \frac{6}{5^{3/2}V^3}(1 - \nu^2)\sqrt{\frac{F^5}{M^3R}} \quad (2.17)$$

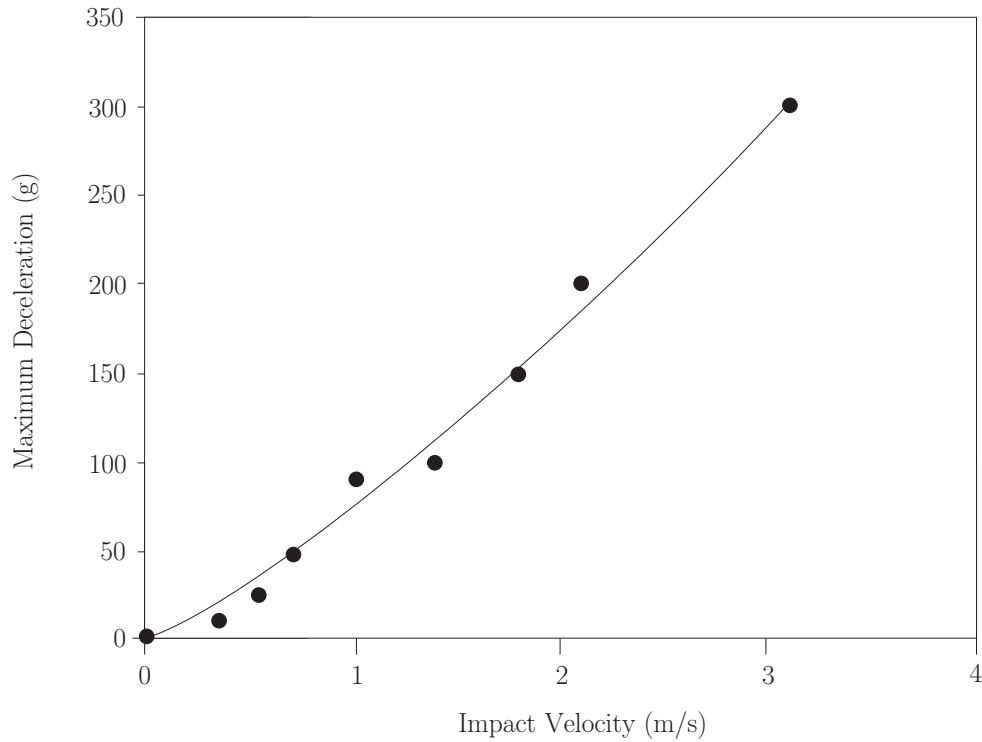


Figure 2-5: The grinding ball impact rate reanalysis—steel ball dropped on a liner plate [Aus01]

the effective modulus of elasticity, using the original data, can be calculated (Table 2-3). Compared to the expected results, the Dunn and Martin modulus of elasticity is smaller by a factor of 10^3 . The Dunn and Martin modulus is not comparable to either the expected modulus, based on the Austin analysis, the ore modulus or the steel modulus.

Austin concludes that the results of the drop weight test were correct, but in the analysis of the drop weight results, the use of the linear model was incorrect. As for the in-service experimental results, Austin questions the validity due to the

Table 2–2: Re-analyzed grinding ball impact force and stress [Aus01]

Mill Diameter (m)		2.74	3.96	8.53
Mill Speed (rpm)		20	14.5	10.2
Mill Speed (percent critical speed)		78	66	69
Total Ball Drop (m)		2.03	2.28	6.39
Impact Velocity (m/s)		6.55	6.79	11.39
Ball Diameter (mm)		76	76	127
Ball Weight (kg)		1.8	1.8	8.4
Estimated Impact Deceleration (g)	with ore	360	380	420
	no ore	690	720	800
Estimated Impact Force (N)	with ore	6 400	6 700	34 800
	no ore	12 300	12 800	66 000

Table 2–3: Estimated modulus of elasticity [Aus01]

	Modulus of Elasticity, E (Pa)
Dunn and Martin (1978) (Effective)	2.4×10^7 to 12×10^7
Austin (2001) (Expected Effective)	5×10^{10}
Steel	2×10^{11}
Ore	6×10^{10}

difference in the Young’s modulus. The rough surfaces and the high impact velocities may limit the validity of the Hertzian analysis.

2.3 The Rolf and Vongluekiet Instrumented Ball

An improved instrumented ball was developed by Rolf and Vongluekiet [RV83, RV84, RS90, Rol99, Ano90], with the aim of directly recording energy distributions within the ball charge.

The Rolf and Vongluekiet instrumented ball [RV84] is illustrated in Figure 2–6. A pestle is mounted flush with the external surface of the shell and is held in place by a rubber spring. If an impact occurs, the pestle is pushed down. If the force is large enough to overcome the resistance offered by the spring, the pestle travels far enough to activate a switch. The switch generates an electric pulse which is recorded by an electronic counter, whose power is supplied by a battery pack. The balancing mass within the instrumented ball adjusts the mass properties of the instrument, with the goal of matching the mass properties of the rest of the charge. Finally, the shell, with an external diameter of 40 mm, is designed to protect the electronics, while keeping the size and surface properties as close as possible to those of the charge. Due to the risk of jamming the pestle, the instrumented ball can only be used without the presence of the material to be milled—no ore is present. Since the area of the pestle, A_{pestle} is smaller than the total area of the instrumented ball, A_{ball} , the impact count must be corrected by a factor equal to the area ratio

$$R = \frac{A_{ball}}{A_{pestle}} \quad (2.18)$$

The number of impacts per ball, per revolution is

$$Z_k = \frac{ZR}{2N} \quad (2.19)$$

where Z is the number of measured impacts, N is the number of revolutions of the mill. Since two balls participate in the collisions, only half the impacts are counted.

Since the instrumented ball is an engineered device, the stiffness of the spring is known. Also, the maximum displacement of the pestle required to activate the switch is known. An impact causing a greater displacement will cause the pestle to hit a geometrical stop, limiting its travel to the maximum displacement. Due to the geometry of the instrument, the displacement of the pestle is also the compression of the rubber spring. Therefore, the impact energy, E_{impact} , associated with the activation of the counting circuit is

$$E_{impact} \geq \frac{1}{2}k_e d_{max}^2 \quad (2.20)$$

where k_e is the effective stiffness of the rubber spring and d_{max} is the maximum travel of the pestle. Several instrumented balls, each with a different spring stiffness, are used to collect the data within a ball mill. The mill has an internal diameter of 800 mm, and a length of 400 mm. The mill is operated either with or without 12 lifters, each with a height of 40 mm.

The instrumented ball measurements are collected and combined. The aggregate measurements are classified by the mill speed, the presence or lack of lifters, and the charge filling fraction. According to Rolf and Vongluekiet, Figure 2-7, an example of the instrumented ball results, can be interpreted as the (complementary) cumulative frequency distribution of the impacts, Z_k , with respect to the impact energy, E_{impact} . The derivative of the cumulative frequency distribution is the frequency distribution (Figures 2-8 and 2-9). Since there are no collisions with zero

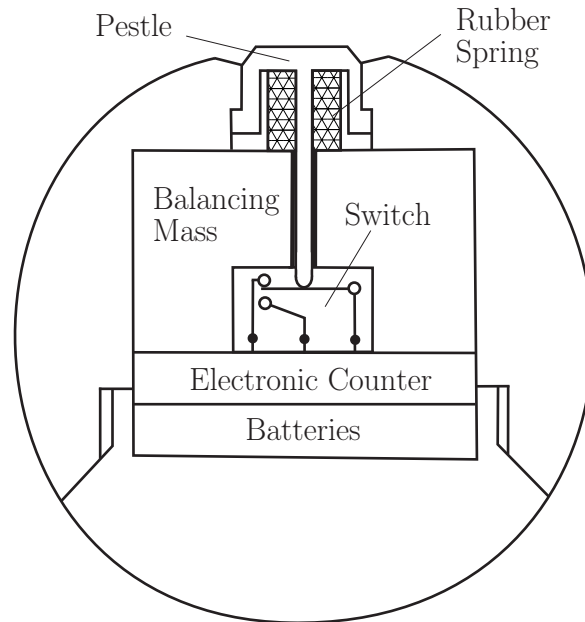


Figure 2-6: The Rolf instrumented ball [RV83]

impact energy, the frequency distribution curves must pass through the origin. The cumulative frequency distribution, $Z_s(E)$, the number of impacts with impact energy between E and $E + dE$ can be found. For all cases, the number of impacts decreases as the speed of the mill speed increases. Also, when the mill is equipped with lifters, a maximum in the impact frequency distributions occur at an impact energy approximately equal to 40 mJ (Figure 2-8). This value corresponds to the potential energy of a ball as it drops a distance equivalent to 15 mm. This distance corresponds to the mean free path, and is constant for the range of ball charges used in the experiments, with mill speeds between 55 and 95 percent critical. Furthermore, the maxima occur only at mill speeds less than the critical speed. Above the critical speed, the frequency distributions change markedly—the maxima observed

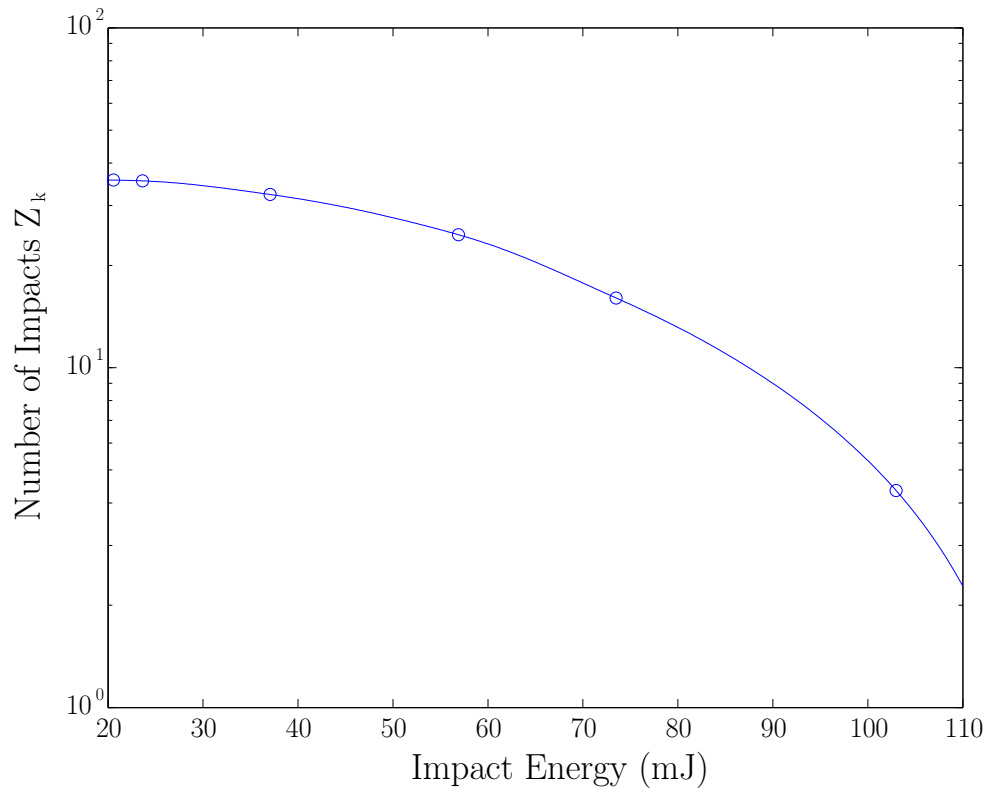


Figure 2-7: The cumulative frequency distribution of the impact energy. [RV84]

below the critical speed are absent. A possible explanation of the frequency distributions at speeds greater than the critical speed is the effect of the centrifugal field and the lifters. Large relative displacements between the balls are prevented, whereas slippage, a low energy process, can occur. When using a mill without lifters, the slip of the charge is important, regardless of the charge and the mill speed. Since the frequency distribution passes through the origin, the maximum of the frequency distribution occurs at an impact energy less than 20 mJ. Such low energy impacts are an indication of very small potential energy drops—the ball does not fall far before it is a party to an impact event, which is not the case when it is slipping.

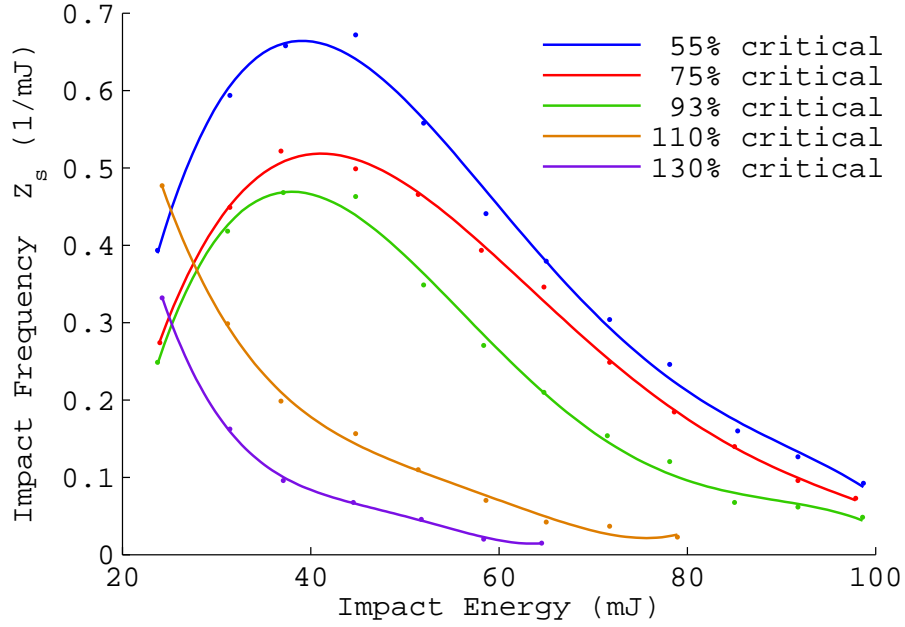


Figure 2-8: The frequency distribution of the impact energy, for a ball mill with lifters. The ball charge is 17.9 percent, and the speed of the mills is between 55 and 130 percent critical. [RV84]

The frequency distributions give the number of impacts per unit energy per ball over one rotation of the mill. If the distribution is integrated over the energy, the impact energy a ball is subjected to per rotation is obtained. Also, if the distribution is integrated, the number of impacts a ball is subject to is found.

$$E_{tot} = \int_{20 \text{ mJ}}^{100 \text{ mJ}} E_{impact} Z_s(E_{impact}) dE \quad (2.21)$$

$$N_{tot} = \int_{20 \text{ mJ}}^{100 \text{ mJ}} Z_s(E_{impact}) dE \quad (2.22)$$

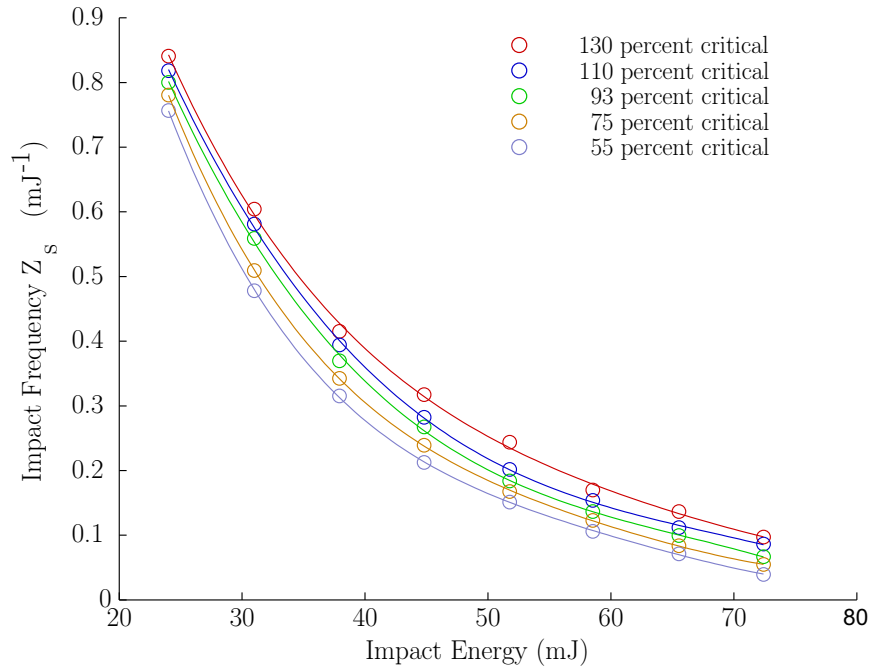


Figure 2-9: The frequency distribution of the impact energy, for a ball mill without lifters. The ball charge is 17.9 percent, and the speed of the mill is between 55 and 130 percent critical. [RV84]

Rolf and Vongluekiet use the discrete versions of the above equations, given as,

$$E_{tot} = \sum_{20 \text{ mJ}}^{100 \text{ mJ}} E_{impact} Z_s(E_{impact}) \Delta E \quad (2.23)$$

$$N_{tot} = \sum_{20 \text{ mJ}}^{100 \text{ mJ}} Z_s(E_{impact}) \Delta E \quad (2.24)$$

to obtain the impact energy per ball (Figure 2-10), and the number of impacts per ball (Figure 2-11), as the mill speed is changed.

Rolf and Vongluekiet conclude that it is possible to obtain a large quantity of information from within the charge. They note that the presence of lifters promote

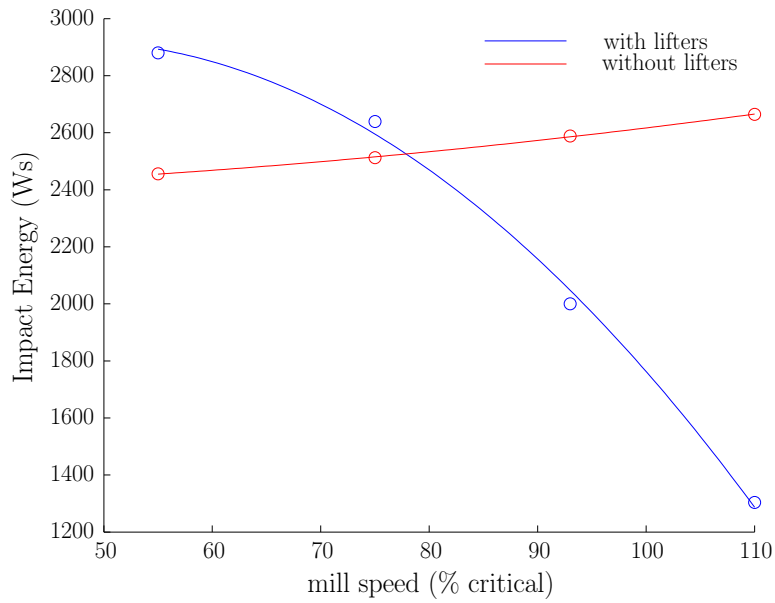


Figure 2–10: The variation of the impact energy as the mill speed changes. [RV83]

high energy impacts when the mill operates below the critical speed. At speeds above the critical speed, the lifters are not effective. They hinder the slippage of the charge. Ordinarily, the slippage generates impacts even though the centrifugal forces greatly affect the charge behavior, as is the case when the mill is operated without lifters.

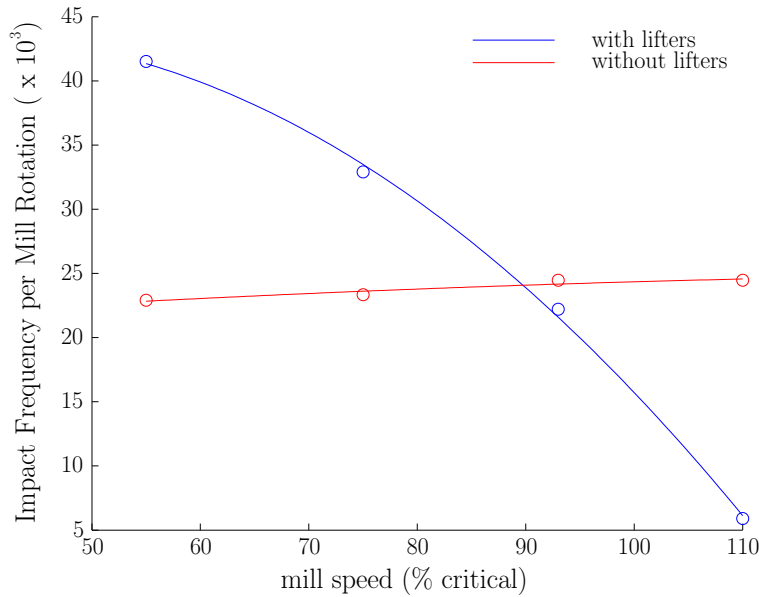


Figure 2–11: The variation of the impact frequency as the mill speed changes. [RV83]

2.4 The Gao and Thelen Instrumented Ball

According to Gao and Thelen, the comminution research, particularly grinding mill research, is limited by the inaccessibility of the measurand and the lack of suitable electronics [GT94], motivating their development of an instrumented ball. Gao and Thelen characterize the grinding processes by the types of loadings found within the mills: dynamic and quasi-static loadings [GT94]. Dynamic loadings involve two colliding bodies, which produce a large force within a short period of time. Furthermore, in addition to the properties of the bodies, the force strongly depends on the kinetic energy of the bodies. By measuring the impact force, the impact energy can be determined [GT94].

The relative motion between bodies are modeled as a combination of rubbing and shearing, characterized by a minimal change in the magnitude of the force throughout

the duration of the interaction. During this quasi-static loading of the bodies, the force between the bodies weakly depends the kinetic energy (and its conversion to other types of energy) [GT94].

In their analysis, Gao and Thelen neglect the quasi-static loading case. Consequently, the weak relation between forces and energy suggests that little optimization is possible. Instead, Gao and Thelen concentrate their research on the dynamic loading cases.

Since grinding mill are machines designed to break ore, they are effective at breaking any instrument installed within the mill. Also, grinding media, such as the steel balls added to the charge that are used to promote the comminuting processes, can effectively destroy measurement systems. Furthermore, Gao and Thelen find it difficult to obtain electronic devices small enough and sophisticated enough for the required data acquisition and processing. Consequently, milling systems are considered black boxes, forcing the adoption of empirical methods in determining a number of parameters, motivating the development of instruments. Bearing in mind the mill environment and the charge motion, the instrumented ball must satisfy the following conditions. Firstly, the instrumented ball must have the same size, mass and surface characteristics as an unmodified grinding ball. Secondly, the diameter of the instrumented ball must not exceed 60 mm. Larger balls are difficult to handle. Thirdly, the instrument must be able to withstand temperatures of 350 K and impacts up to 450 g. Also, the instrument must protect the electronics from any dust and water. Finally, the instrument must process a 100 μs impact signal. A design based on a piezoelectric sensor (Figure 2–12) is proposed by Gao and Thelen. In response

to an applied pressure or stress, a piezoelectric material generates a voltage. The instrumented ball is composed of the following modules:

1. *Pre-amplifiers.* The high impedance charge signals produced by the piezoelectric sensor is converted to a low impedance voltage.
2. *Signal conditioners.* A low-pass filter eliminates some of the distortions of the sensor signal.
3. *Analog-to-digital converters.* The sensor signal is converted to a digital number by a set of voltage comparators.
4. *Electronic memory.* The converted signal is stored in memory, with a capacity of 64K.
5. *I/O ports.* An off-line version of the instrumented ball can transfer previously stored data to an external console. An on-line version can modulate and transmit the data at a frequency of 433 MHz.

The test mill for the Gao and Thelen instrumented ball is 400 mm in length, with a diameter of 800 mm. For the tests, the grinding media void ratio, Φ_m , defined as the ratio of the bulk volume of the grinding media—in this case, quartz—to that of the balls, was varied between 0.0 and 1.0. The rotation speed of the mill was set to 40, 60, 80, or 100 percent of the critical speed.

A dynamic impact process produces a compression and a restoration phase. The change in the kinetic energy of a body, E_b , before and after the collision, is

$$E_b = \Delta E_{ke} = \frac{1}{2}(1 - \epsilon^2)(\delta v)^2 \frac{m_1 m_2}{m_1 + m_2} \quad (2.25)$$

where m_1 and m_2 are the masses of the colliding bodies, ϵ is a material dependent coefficient ($0 \leq \epsilon \leq 1$), and δv is the change in speed. Assuming an elastic deformation during the impact process, the maximal force amplitude, F_{max} , is expressed as

$$F_{max} = \left[\frac{1.25 m_1 m_2 (v_2 - v_1)^2}{(m_1 + m_2) \left\{ \frac{9}{64} \left(\frac{1}{R_1} + \frac{1}{R_2} \right)^{1/3} \left(\frac{1-\rho_1}{G_1} + \frac{1-\rho_2}{G_2} \right) \right\}^{2/3}} \right]^{3/5} \quad (2.26)$$

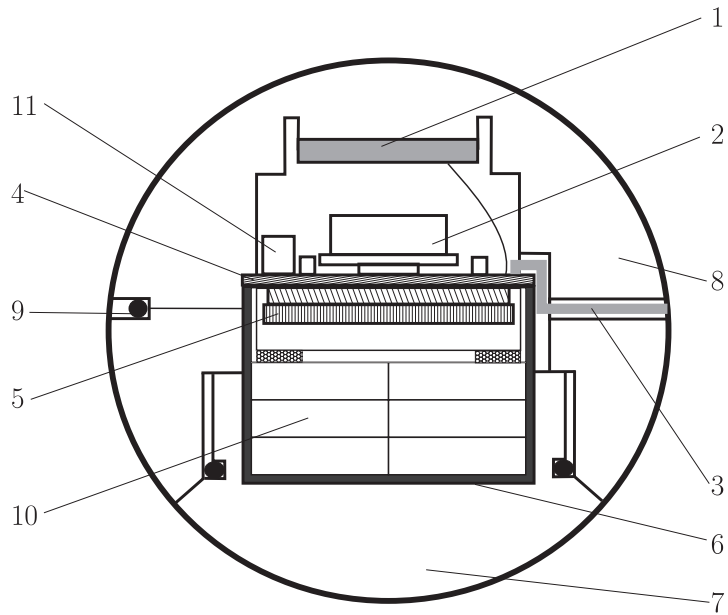
where R_i is the radius of the i^{th} colliding body. Also, G_i is the shear elastic coefficient, ρ_i is the Poisson ratio and E_i is the modulus of elasticity of the i^{th} material, associated with the i^{th} body. The maximal effective grinding energy, E_p , is equal to the maximal loss of mechanical energy, E_b (with $\epsilon = 0$), giving

$$F_{max} = \frac{1.94 E_p^{0.6}}{\left(\frac{1}{E_1} + \frac{1}{E_2} \right)^{0.4} \left(\frac{1}{R_1} + \frac{1}{R_2} \right)^{0.2}} \quad (2.27)$$

Using Equation 2.27, the distribution of the grinding energy can be determined from the measurement of the impact forces, as long as the ball dimensions and material properties are known. The number of measured impacts per revolution of the mill, scaled to account for the measurement zone area in comparison to the whole surface of the ball—the active area does not encompass the entire ball area, as shown in Figure 2-12—gives the impact frequency, H_i . The impact frequency, H_i , is a measurement of the number of times the ball impacts other bodies during one mill revolution. At the same time, the impact force measurements help determine the impact energy, E_p . The results are presented in Figures 2-13, 2-14 and 2-15.

When the mills speed is increased, more of the charge is thrown, creating larger spaces within the charge (see Figure 1–10). With less material available to damp any interactions, high energy impacts occur more often. This effect, seen in Figures 2–13 and 2–14, continues until the speed of the mill approaches the critical speed, when the charge begins to settle. A further increase in the speed of the mill will lock the charge, greatly reducing the number of impacts. As shown in Figure 2–15, a maximal impact frequency, H_i , exists within the range of 60 to 80 percent critical speed.

Gao and Thelen conclude that an instrumented ball, capable of operating within a realistic ball mill environment, such as one with quartz as the grinding medium, can be designed, fabricated and tested. Furthermore, by correlating the impact frequency, the impact energy and the specific energy required to grind a material, it may be possible to develop guidelines useful to the design and optimization of mills. Finally, the technology used in the development of the instrumented ball can be adapted to other industrial applications characterized by an insufficient accessibility to the measurands.



- | | |
|----------------------------|---------------------------|
| 1. Piezo-sensor | 7. Lower shell |
| 2. HF transmitter | 8. Upper Shell |
| 3. Antenna | 9. Sealing ring |
| 4. Circuit board | 10. Battery |
| 5. Hybrid circuits | 11. Electronic components |
| 6. Housing and cover plate | |

Figure 2-12: The Gao and Thelen instrumented ball [GT94]

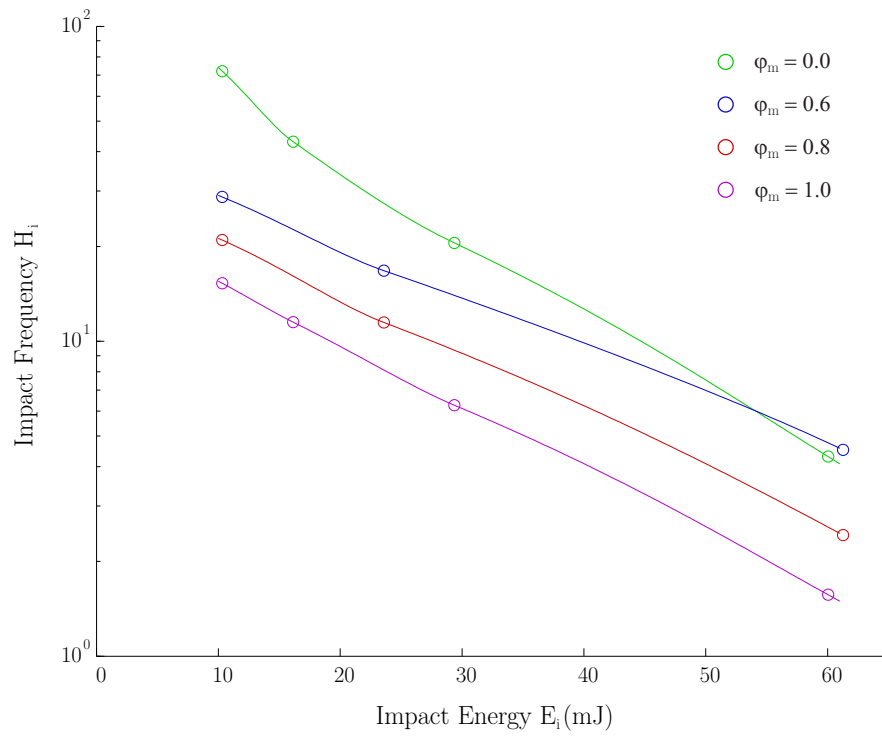


Figure 2-13: The frequency I intensity of the impact energy at 40 percent critical speed [GT94].

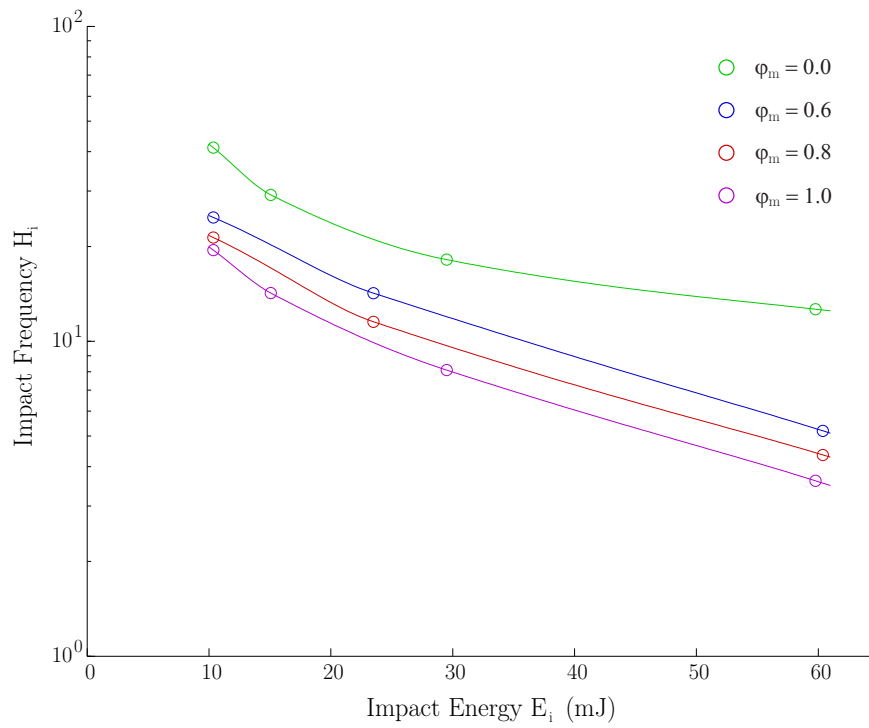


Figure 2–14: The frequency intensity of the impact energy at 100 percent critical speed [GT94].

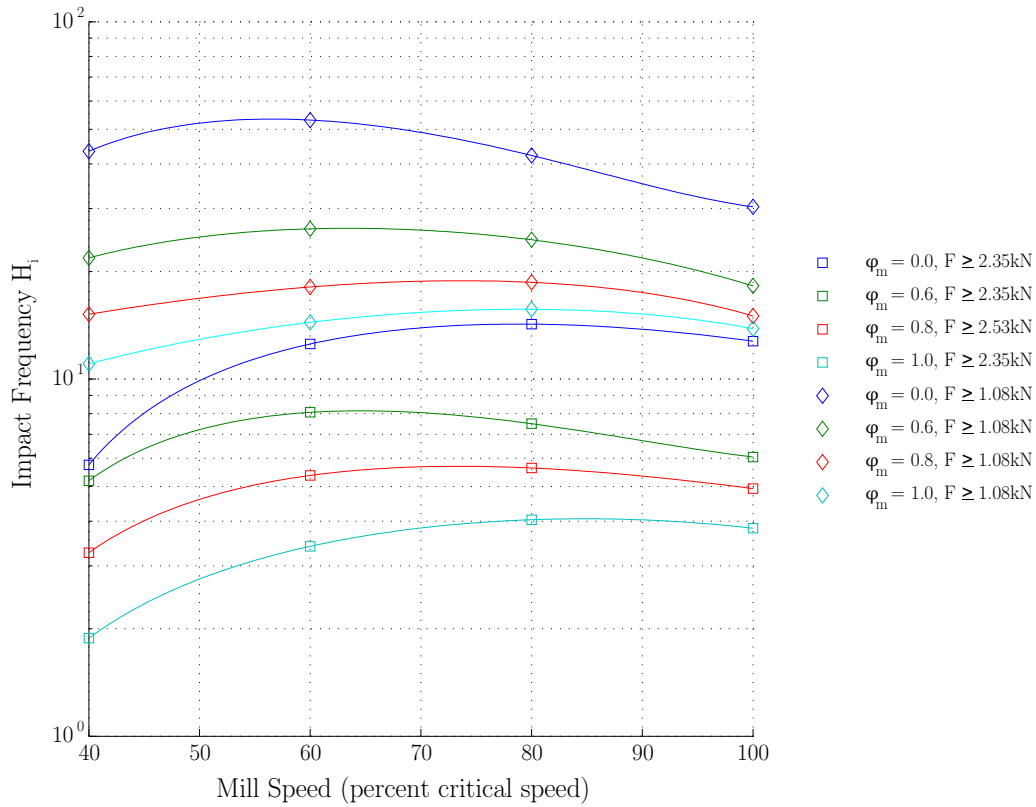


Figure 2–15: The impact frequency as a function of the mill speed [GT94].

2.5 The Rajamani, Delgadillo and Duriseti Instrumented Ball

Rajamani, Delgadillo and Duriseti [RDD06] designed a instrumented ball capable of measuring the stresses it is subject to, providing a means of monitoring the internal state of the mill.

Rajamani, Delgadillo and Duriseti modified a large ball (5 to 6 inches in diameter), forming an internal cavity, large enough to house a strain gauge based load cell, the telemetry electronics (FM transmitter and receiver), and a lithium ion battery (Figure 2–16). When added to the charge, the Rajamani instrumented ball wirelessly transmits the load cell measurements to an external receiver. A computer, connected to the receiver, records the measurements. From this record, a time history of the impacts and impact energy spectrum is determined. The ball continues to operate until either the battery is drained or the instrument is damaged by the action of the mill.

Two problems were encountered during the initial tests. Firstly, the electronics were quickly damaged during the tests [Raj07]. Embedding a large number of micro-electronic components within a grinding ball is challenging, especially if they must survive for an extended period of time. Secondly, the transmission of the measurements from within the mill to the receiver was not possible. The large quantity of metal within the mill and forming the mill shell creates a barrier to electromagnetic signals—particularly weak signals. Due to these technical challenges, the instrumented ball was modified. Instead of measuring the stresses on a ball, Rajamani,

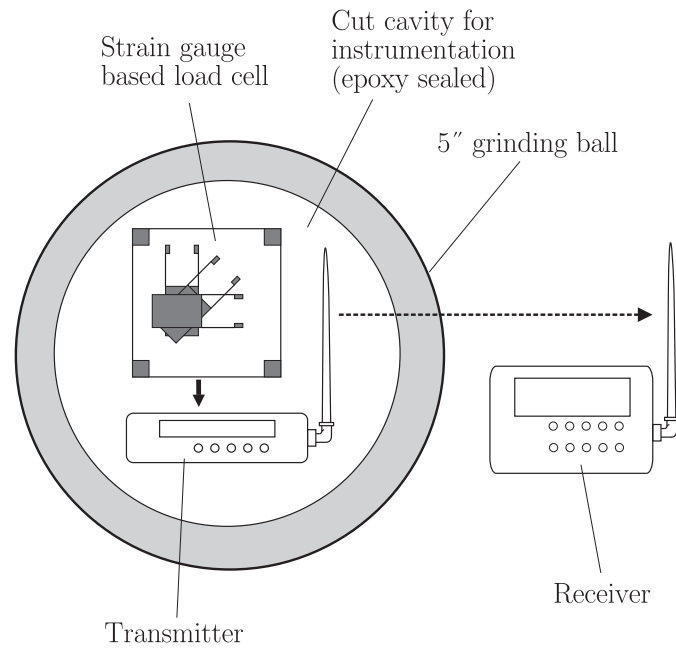


Figure 2-16: The Rajamani *et al.* instrumented ball [RDD06]

Delgadillo and Duriseti decided to measure the stresses on the liner. Now, the measurement devices are no longer housed within a ball. Instead, they are mounted externally on the mill shell (Figure 2-17).

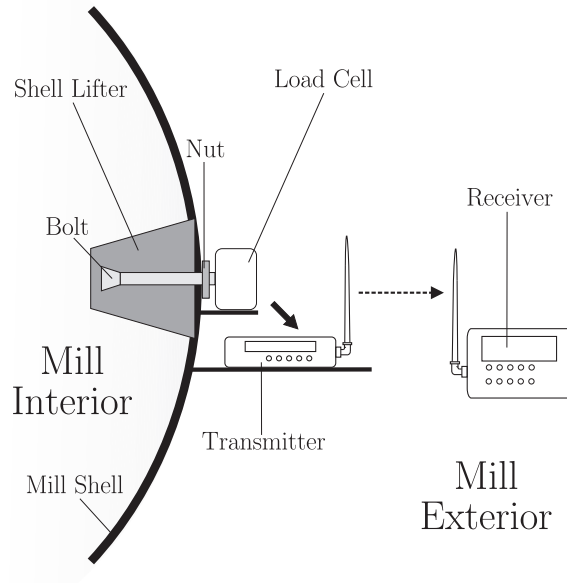


Figure 2–17: The alternative Rajamani mill instrumentation [RDD06]

2.6 Discrete Element Models

The discrete element method (DEM) is a class numerical modeling technique used for the simulation of the behavior of a large number of discrete interacting particles [MR92]. The field of application includes granular flows, traffic and crowd dynamics, astronomy, computer networks, biosystem interactions, geomechanics, agriculture, pharmaceuticals, and mineral processing [WS08, Cle98, DEM09].

The discrete element method, developed by Cundall and Strack [CS79], calculated the finite displacements and rotations of a large number of particles, over a

given timestep. As the calculation proceeds, the particles interact with the other particles or with the environment, as mediated by contact and non-contact forces [MR92, ZZRA08]. The simulation process is summarized in Figure 2–18.

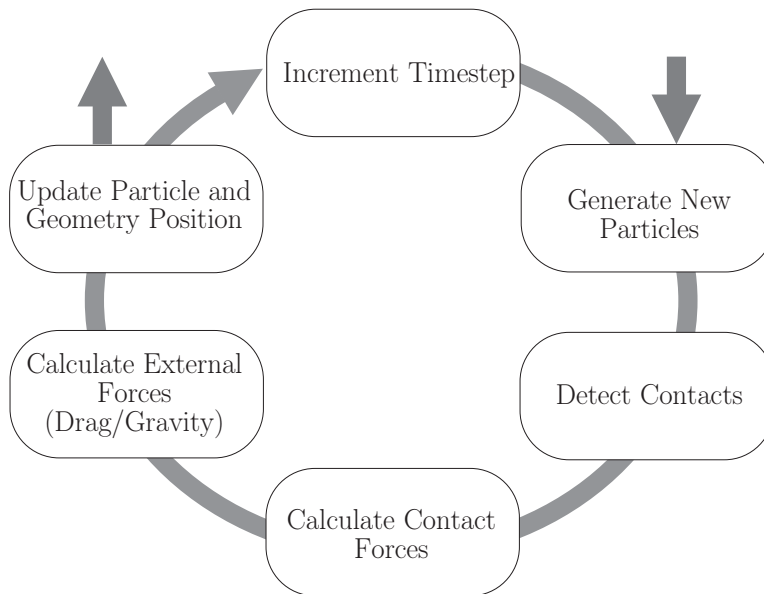


Figure 2–18: The DEM calculation loop [DEM09].

2.6.1 Geometry

First, new particles and the geometry are created. The geometry consists of solid bodies that are essential to the simulation, but are not part of the granular particles—the mill liners and the mill shell are two examples of the geometry. The geometry constrains the particles by defining the boundaries of the simulation. At this point, the importance of geometric abstractions comes to light. As an example, Mishra and Rajamani simulate a mill as a 2D DEM [MR92]. The mill cross-section abstracts the mill geometry, the inner boundary delimiting the area within which the charge will evolve; the charge is defined as a large assembly of discs, each identified

separately by a radius, a mass, a moment of inertia, and collision properties. A similar procedure can be applied to the 3D models, as demonstrated by Martins *et al.* [MRP⁺07]. In this case, spheres represent the particles that compose the charge; a simplified CAD drawing represents the mill. The particles can be modeled using other shapes. Aggregations of spheres [DEM09], super-quadric geometries [Cle98], and arbitrary shapes [PHSP07] are used to represent particles. The choice of how the particles are modeled is driven by balancing the computational efficiency with the accuracy of the simulation [ZZRA08]. Finally, material properties are associated with the geometry or the particles, as they are created.

2.6.2 Contact Detection

Next, the contacts between particles are detected. This task consists of determining if each individual particle contacts any other particle or geometry. One solution is to search through the particles pairs in order to determine if the distance between them is less than a set threshold. Such a pairwise search is computationally demanding algorithm, of order $O(N^2)$, where N is the number of particles [Fer01]. In practice, a more efficient contact detection scheme is used—only near neighbors of the particle are considered to be candidates in the event of a collision. A search grid is used periodically to build a near-neighbor interaction list that contains all the particle pairs that are likely to experience a collision in the short term. Only the particles considered to be part of the set of nearest neighbors of the selected particle are tested for collisions. All other particles are considered to be too far to possibly collide with the selected particle. Though the set of nearest neighbors must be updated with each timestep, this strategy can, in certain cases, reduce the

Table 2–4: Contact force and torque models [ZZYY07]

Force Models	Normal Force	Tangential Force
linear spring-dashpot model	$\mathbf{f}_n = -K_n \delta_n \mathbf{n}_c - C_n (\mathbf{v}_c \cdot \mathbf{n}_c) \mathbf{n}_c$	$\mathbf{f}_t = -K_t \mathbf{v}_c^t + C_t (\mathbf{v}_c \times \mathbf{n}_c) \times \mathbf{n}_c$
simplified Hertz-Mindlin and Deresiewicz model	$\mathbf{f}_n = \begin{aligned} &-\frac{4}{3} E^* \sqrt{R^*} \delta_n^{3/2} \mathbf{n}_c \\ &-C_n (8m^* E^* \sqrt{R^*} \delta_n)^{1/2} \\ &\cdot (\mathbf{v}_c \cdot \mathbf{n}_c) \mathbf{n}_c \end{aligned}$	$\mathbf{f}_t = \begin{aligned} &-\mu \mathbf{n}_{n,e} (1 - (1 - \mathbf{v}_c^t /\delta_{max})^{3/2}) \hat{\mathbf{v}}_c^t \\ &+ 2C_t (1.5\mu m^* \mathbf{n}_{n,e} \\ &\cdot \sqrt{1 - \mathbf{v}_c^t /\delta_{max}} \delta_{max}^{-1})^{1/2} \\ &\cdot (\mathbf{v}_c \times \mathbf{n}_c) \times \mathbf{n}_c \end{aligned}$
Walton and Braun model	$\mathbf{f}_n = \begin{aligned} &-k_1 \delta_n \mathbf{n}_c, \delta_n \geq 0 \\ &\text{(loading)} \\ &-k_2 (\delta_n - \delta_{n0}) \mathbf{n}_c, \delta_n < 0 \\ &\text{(unloading)} \end{aligned}$	$\mathbf{f}_t = \begin{aligned} &\mathbf{f}'_t + k_t^0 (1 - \frac{f_t - f_t^*}{\mu f_n - f_t^*})^{1/3} \Delta \mathbf{v}_c^t \\ &\text{if } \dot{\mathbf{v}}_c^t \text{ in initial direction} \\ &\mathbf{f}'_t + k_t^0 (1 - \frac{f_t^* - f_t}{\mu f_n + f_t^*})^{1/3} \Delta \mathbf{v}_c^t \\ &\text{if } \dot{\mathbf{v}}_c^t \text{ in opposite direction} \\ &\text{where } f_t = \mathbf{f}_t , f_n = \mathbf{f}_n \end{aligned}$
Torque Models	Rolling friction torque	Torque from \mathbf{f}_t
Method 1	$\mathbf{m}_r = -k_r \theta_r - C_r d\theta_r/dt$	$\mathbf{m}_t = \mathbf{R} \times \mathbf{f}_t$
Method 2	$\mathbf{m}_r = -\min \{ \mu_r \mathbf{f}_n , \mu'_r \omega_n \} \hat{\omega}_n$	

computational time to $O(N)$ [Cle04, VCVQ⁺98]. Industrial simulations with up to a million particles are currently possible in reasonable times on current single processor workstations.

2.6.3 Contact Forces

Once the contacts have been detected, the contact forces are calculated. The contact force model allows the simulation to calculate the forces applied to the particle as it undergoes a collision. Depending of the level of detail, these models take several forms [KESR⁺07, KESWS07], as the examples listed in Table 2–4 demonstrate. The details of the contact force models listed in Table 2–4 are not explained, as the purpose is only to show the variety and differences between types of contact

models. In many cases, the DEM models use the spring-dashpot contact model, due to its modest computational requirement, in contrast to many other contact force models. Regardless of the contact models, its coefficients are derived from or agree with physical measurements. For example, when using the spring-dashpot model, an appropriate normal damping coefficient, C_n , is selected such that the normal response produces agreement with the observed coefficient of restitution, defined as the ratio of the post-collision to pre-collision normal component of the relative velocity [Cle04, MX08].

2.6.4 Body Forces

After the contact forces have been determined, the body forces are calculated. The body forces include gravity, van der Waals forces, liquid bridge forces and electromagnetic forces [ZZYY07]. In the context of the grinding mill, only gravity is considered.

$$\mathbf{F}_i^b = m_i \mathbf{g} \quad (2.28)$$

where m_i is the mass of the i_{th} particle, and \mathbf{g} is the gravitational acceleration.

2.6.5 Equations of Motion

Since a particle in a granular flow can have both translational and rotational motion, the governing equations of motion are [ZZYY07]

$$m_i \dot{\mathbf{v}}_i = \sum_j \mathbf{F}_{ij}^{contact} + \mathbf{F}_i^{body} \quad (2.29)$$

$$\mathbf{I}_i \dot{\boldsymbol{\omega}}_i = \sum_j \mathbf{M}_{ij} \quad (2.30)$$

where \mathbf{v}_i is the translational velocity of the i^{th} particle, ω_i is the angular velocities of the i^{th} particle, m_i is the mass of the i^{th} particle, $\mathbf{F}_{ij}^{contact}$ and \mathbf{M}_{ij} are the contact force and torque acting on the i^{th} particle due to the j^{th} particle or any geometry (such as walls), \mathbf{F}_i^{body} is the body force acting on the i^{th} particle, and \mathbf{I}_i is the moment of inertia tensor of the i^{th} particle. Since the forces and torques are calculated, and the mass properties are known, it is possible to solve Equations 2.29 and 2.30, and propagate the i^{th} particle to the next timestep. This is done for all particles and geometry, thereby updating their positions and velocities. At this point in the simulation, new particles can be added to the simulation. If none are added, the simulation proceeds to the detection of collision. Again, this cycle is illustrated in Figure 2–18.

2.6.6 Use of Discrete Element Models

The nature of the quantitative predictions that can be made, using the extensive states produced by the DEM model, is varied. It can be used to determine [Cle04]:

- (a) the boundary stresses, for the mechanical design and the prediction of fatigue;
- (b) the wear rates and distributions, for estimating the life span of the equipment and the wear components;
- (c) the accretion rates, for the prediction of accretion induced blockage or changes in open area of screens;
- (d) the collisional force distributions, collision frequencies, and energy absorption spectra, for understanding breakage and agglomeration;
- (e) the power consumption and torque, for equipment design;
- (f) the flow rates and flow statistics, for summarizing the characteristics of complex flows;
- (g) the sampling statistics, for the assessment of the accuracy of various sampling processes;
- (h) the mixing and segregation rates, for the assessment of the progress

of intended mixing and de-mixing processes, and for understanding the degree of segregation and its effects on other processes, where segregation and/or mixing are not intended; (*i*) the residence time distributions, for the assessment of the range of times that particles are exposed to the various environments within a process, such as granulation and comminution; and (*j*) the axial transport rates, for the assessment of the axial flow along rotating or stationary cylinders.

As with all simulations, care is required. The behavior of discrete element models is sensitive to the characteristics of the particles and to the underlying assumptions [Cle01b]. Two examples illustrate this point. Firstly, spherical and non-spherical particles will produce a different DEM result, as shown in Figure 2–19. For an industrial application, such as a mill, the computational advantages of spherical particles may outweigh the systematic computational errors due to the geometric differences, particularly if large numbers of particles are being simulated. Secondly, due to the differences in their implementation, the DEM model will have different levels of accuracy and precision, as illustrated by the DEM power draw predictions plotted in Figures 2–20 and 2–21.

The prerequisite to an accurate simulation is the validation test. Comparisons between the *in-situ* and *in-silico* values, such as the power draw, the toe position, the shoulder position, the position of the center-of-circulation and the trajectories, are used to validate the simulations [CMM03, MR94b, PN96, Mis03, RMVD00]. Some of the validation tests, such as the power draw, are reliable. Others, such as trajectory comparisons, suffer from subjectivity [MGPC04].

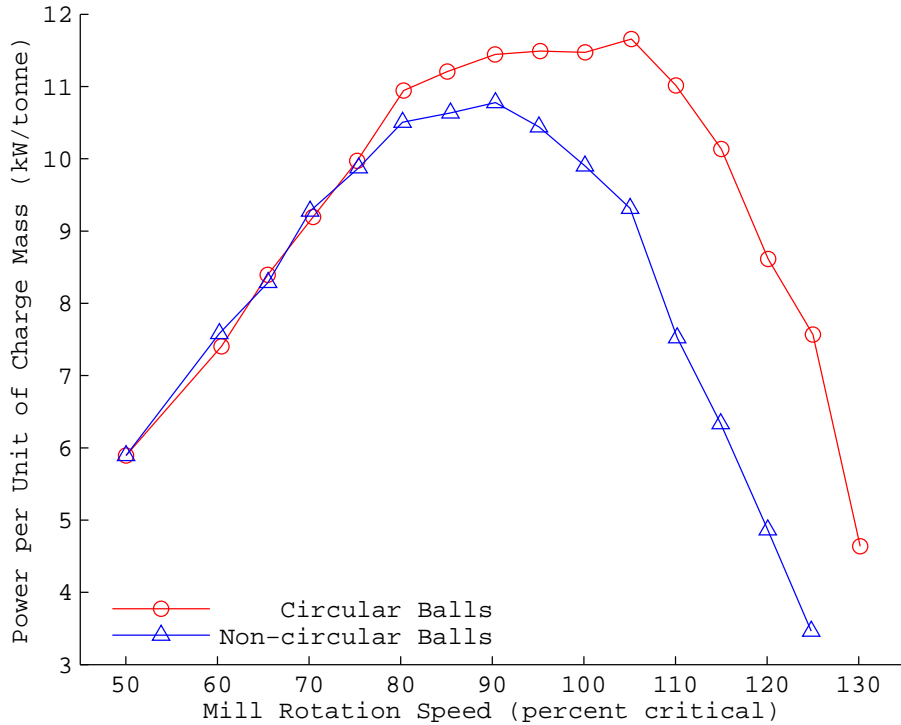


Figure 2–19: The effect of the shape of the ball size distribution on the specific power consumption [Cle01b].

As stated previously, a DEM simulation provides a wealth of information. From the simulation data, it is possible to generate trajectories of the charge, the spatial distribution of the charge, over a cross-section of the mill, and distributions of the kinetic energy, as illustrated in Figures 2–22, 2–23 and 2–24, respectively. It is noted that Misra and Cheung present various distributions of the kinetic energy (Figure 2–24), based on the DEM results at a specific point in time [MC99]. The DEM results, presented by McBride *et al.* [MGPC04], subdivide the mill cross-section into bins. By grouping and summing all data points falling within a bin,

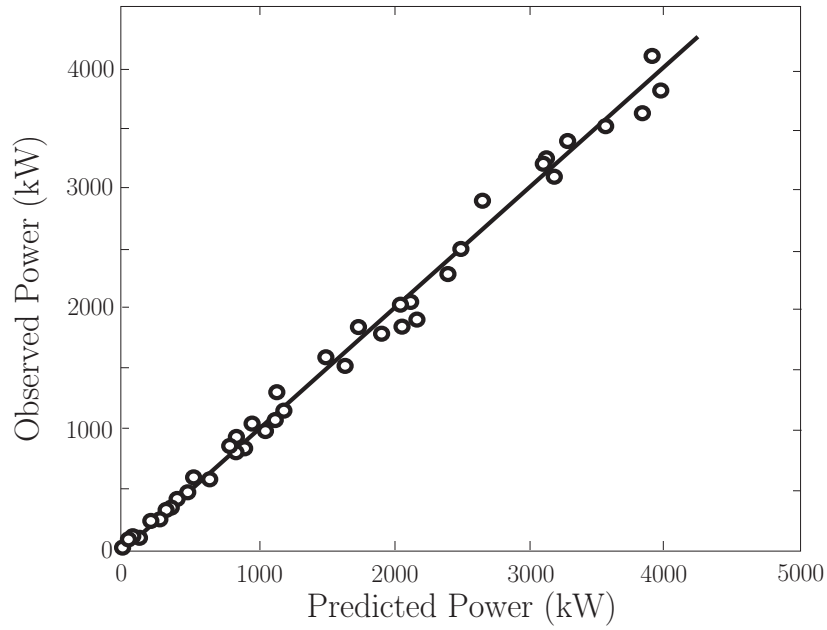


Figure 2–20: Simulated power and observed power [RM98]

a cross-sectional probability distribution is constructed. In doing so, any selected variable, either experimental or simulated, can be expressed as a function of position [GMP04]. For example, using this methodology, McBride *et al.* are able to generate and compare velocity distributions over the cross-section between the experimental setup and DEM simulations, as shown in Figure 2–25.

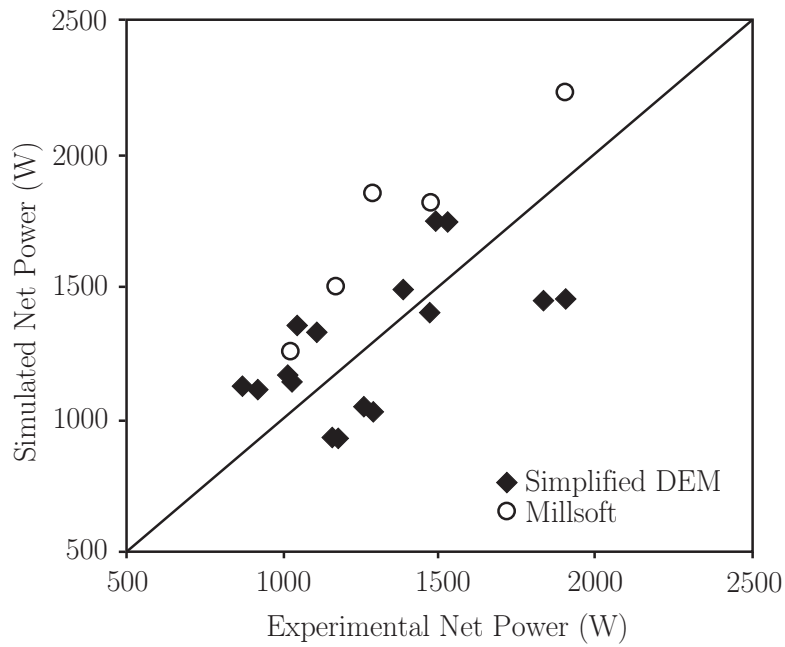


Figure 2-21: Simulated power and observed power [CAR+06]

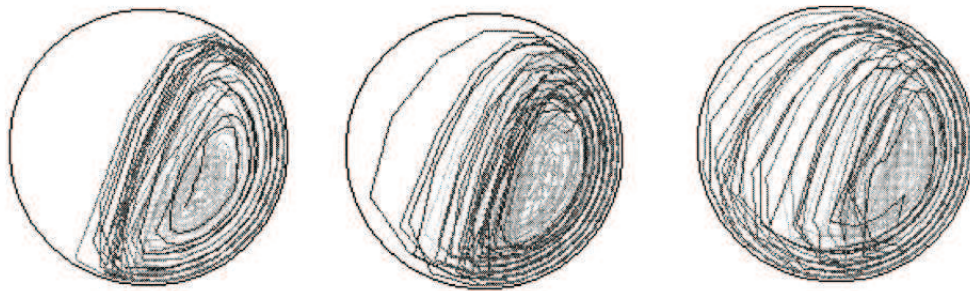


Figure 2-22: Ball trajectories for 4 mill revolutions at 66 percent, 83 percent, and 93 percent critical speed [MC99]

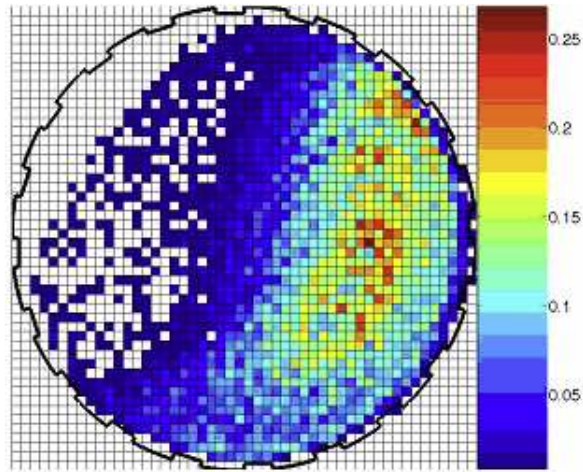


Figure 2–23: Percentage occupancy of a 2 mm rock particle for the mill rotating at 75 percent critical speed [BGC⁺09]

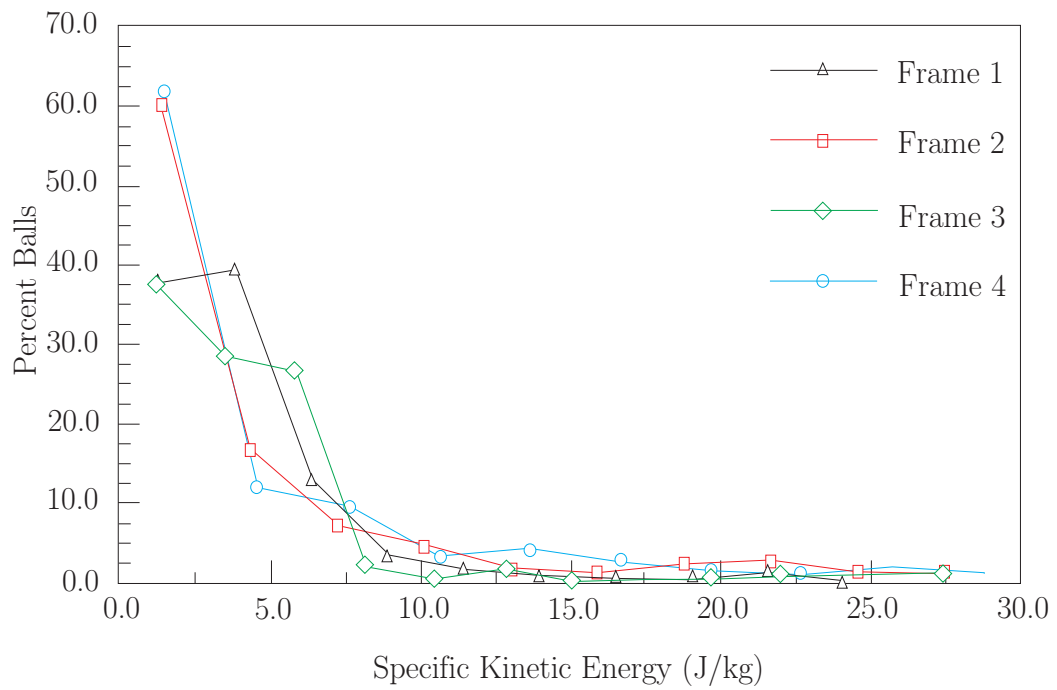


Figure 2–24: DEM kinetic energy distributions [MC99]

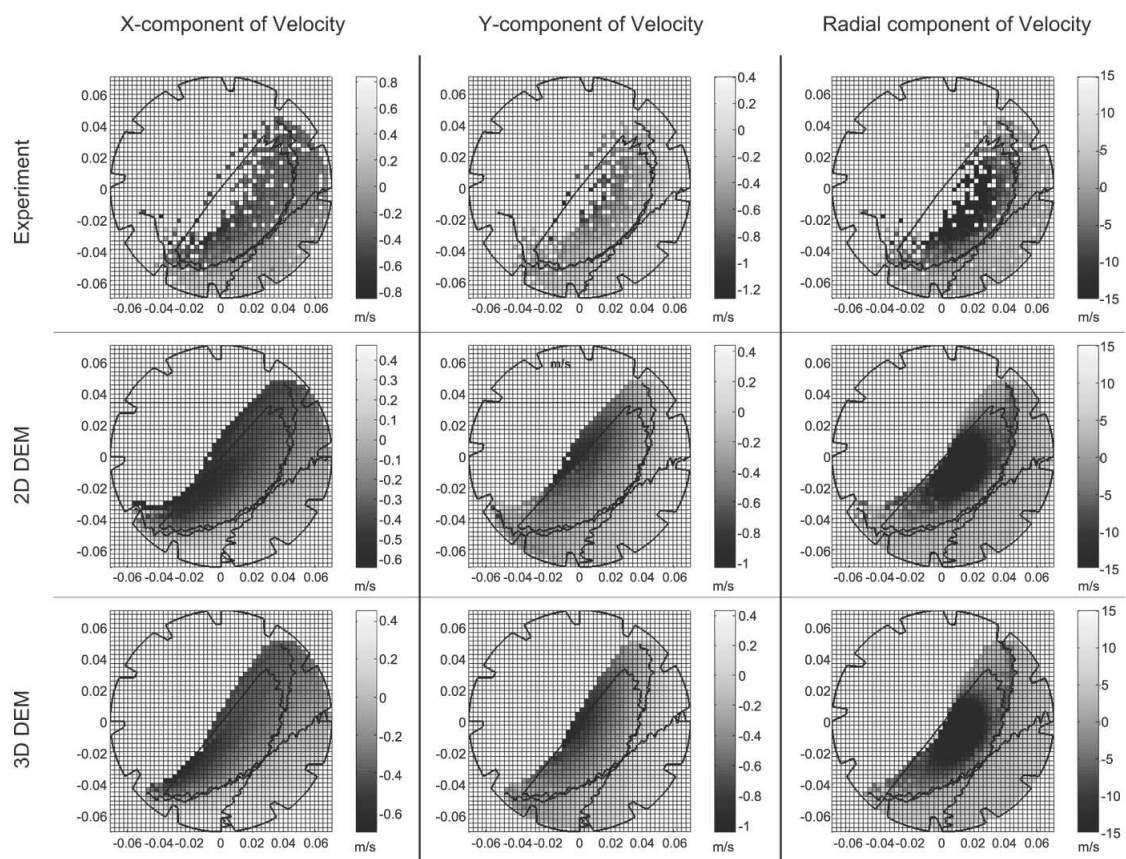


Figure 2-25: Experimental and DEM bin plots of selected components of particle velocity [MGPC04]

2.7 Summary

It is well established that standard comminution methods are energy intensive and inefficient in promoting mineral liberation [VW91], particularly for grinding mills, a type of machinery important in the mineral processing of ores. The motion of grinding media and the energy distribution have a profound influence on the comminution of particles in tumbling mills [Mis03]. Furthermore, it is understood that the mill environment is harsh. The ore-to-ore and the ore-to-steel collisions, which leave any instrument placed within the mill vulnerable to damage, make any measurement from within the mill very difficult. In spite of the difficulties, some progress is reported. A small number of instrumented balls have been built and used to collect data from within the mill, mostly for the determination of impact forces and impact energies. This shows it is possible to build an instrumented ball. Furthermore, electronic circuitry can be embedded within the ball, allowing the operation of a number of instruments. Though the capability exists, only a small number of instrumented balls have been designed. Given the limited instrumentation, DEMs are used as surrogate instruments, thereby allowing the calculation of quantities hereto unmeasurable. As designed, both instrumentation and simulation show promise and are expected to improve the understanding of the dynamics of the charge.

With all this in mind, the goal of this work, which is to develop a better understanding of tumbling mill dynamics through the development, use and validation of an instrumented sensor ball, will be achieved by working towards and meeting the following objectives:

1. To show that an instrumented ball can be designed and built, with improved electronics;
2. To show that it is possible to obtain measurements from the mill interior, particularly measurements that are not impact forces;
3. To show that these measurements allow for a different type of analysis of the mill;
4. To show that the data is comparable to DEM simulation results;
5. To show that the data is helpful with regards to DEMs.
 - (a) The instrument measurements can be used to verify that the DEM results accurately represent the system;
 - (b) The instrument measurements can be used to tune the DEM simulations, enhancing their accuracy; and
 - (c) The instrument measurements can be used to identify aspects of the DEMs in need of improvement.

CHAPTER 3 Materials and Methods

3.1 Introduction

Due to the difficulty of obtaining measurements, ball mills are difficult systems to understand. In this section, a framework allowing for an improved description of ball mills, through measurement and analysis, is presented. The core of this analysis is the instrumented ball. Its design and properties are presented. The instrumented ball is used, in conjunction with a camera system, to measure a number of physical quantities. The physical quantities, and derived quantities thereof, are collectively referred to as measurands. A method of analyzing the measurand is outlined. The methodology, applicable to both *in-situ* (experimental) and *in-silico* (simulated) results, provides a means to compare both. As a result, the methodology is proposed as a means to improve the understanding of tumbling mills.

3.2 Instrumentation

With the goal of investigating the behavior of tumbling mill charge, a number of instruments have been developed within the larger scope of this work [MLRC06a, MLRC06b, RML⁺06, Piced]. The improved instrumented ball is one of the cornerstone technologies developed for the study of tumbling mills, and is used in the present work. One of the supporting instruments, the video systems, adds a number of important measurements, and is also described.

3.2.1 Instrumented Ball

An objective of the development of the instrumented ball is to address the issue of measuring ball accelerations and rotations over a period of time, and to store this information on board. The preliminary steps are to design and integrate the core of the instrument electronics. The high strength instrument shell and wireless communication capabilities are not necessary, as the initial testing would be completed using the laboratory mill, with an engineered charge. This approach simplified the design problem to an attainable objective [MLRC06a].

3.2.2 Instrumented Ball Electronics and Software

The core of the instrument is contained within the assembly of the shell. Cavities are machined into the shells, forming pockets where the internal electronics are secured. When fully assembled, the shell protects the internal electronics. The electronics are separated into the following subsystems (Figures 3–1 and 3–2) [Li04]:

1. the power system
2. the microcontroller, including the clock
3. the storage array
4. the sensor array
5. the communication ports

The power system regulates the power to the instrumented ball electronics. Presently, the power source is a 9V battery. Laboratory measurements indicate that 0.63 W are required to operate the instrumented ball. The system clock regulates the sampling rate for the system. Moreover, since the sampling rate is known, the

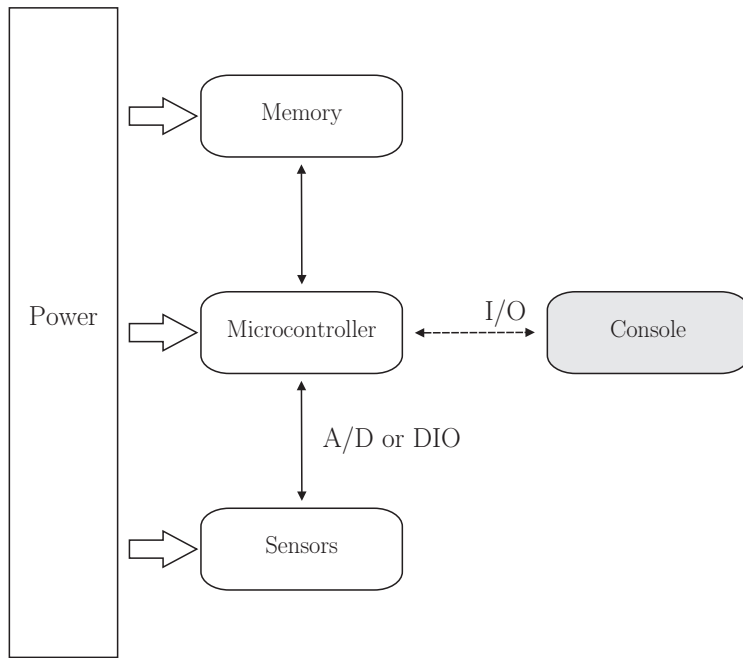


Figure 3–1: The instrumented ball circuit

measurements can be time stamped. Although the maximum sampling rate is 10 kHz, the initial tests were completed at a frequency of 300Hz. Subsequent test were done at a sampling rate of either 1 kHz, 2 kHz, or 4 kHz. The storage array allows the instrument to save the collected data as it operates within the mill. At the sampling frequency of 300 Hz, the instrumented ball is able to collect data over a period of 30 minutes. At a sampling rate of 4 kHz, the instrumented ball can collect and store data for only 2 minutes. Though a wireless port is present, communication with the ball is accomplished via its serial port. The decision to exclude the wireless data transfer capability, during or after measurement, allowed the development of the instrument to avoid one of the major hurdles encountered by Rajamani, Delgadillo and Duriseti [Raj07]. Currently, any commands or data transfers require the instrumented ball

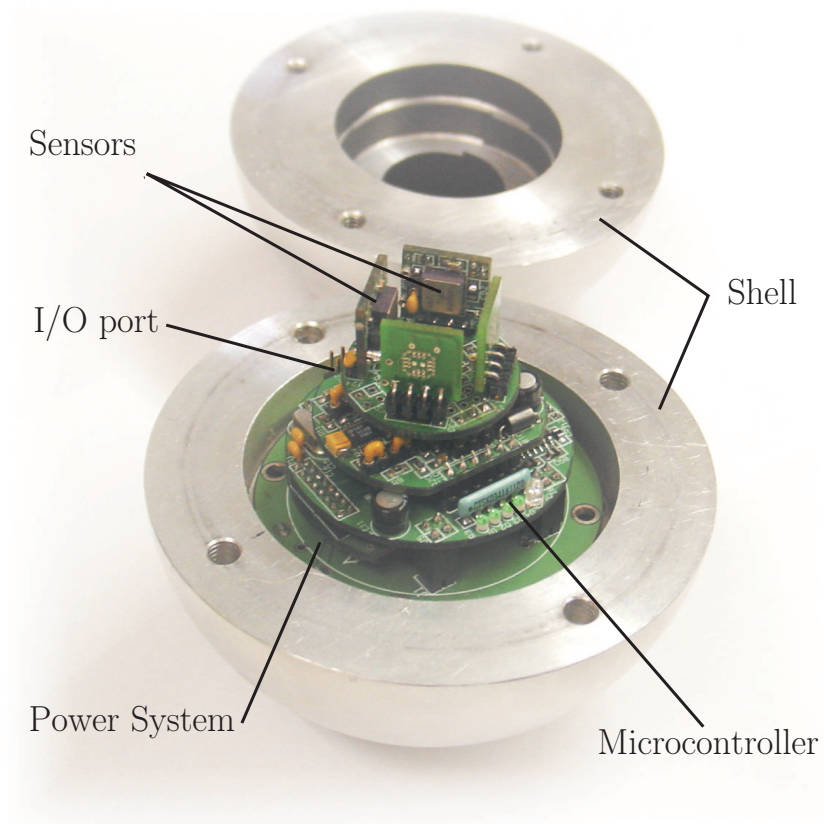


Figure 3-2: An opened instrumented ball

to be opened. The communication port is then connected to a computer, and the *Terminal* application is used to transfer the data.

Through the port, commands can be sent to the ball. The commands include *i)* dump data from the ball to the console via serial port; *ii)* set the sample frequency; *iii)* set the data collection time; and, *iv)* set the delay time before data collection begins. Once initialized, the instrument begins a set of timers. These timers indicate when certain actions are to be taken by the software, such as the collection of the data. The instrumented ball software flowchart is outlined in Figure 3–3. Currently, the sensors in the ball are

1. a 3-axis rotation rate sensor
2. a temperature sensor
3. two 3-axis accelerometers

The sensors allow the measurement of the acceleration, \mathbf{a} , the rate of rotation, ω , and the temperature within the instrumented ball, T , as a function of time.

3.2.3 Instrumented Ball Shells

The instrumented ball is designed to be flexible [MPF⁺08, MLRC06a, MLRC07]. Two distinct parts form the instrument: the electronics and the protective shell. Depending on the desired features, different shells can be used to house the electronics. For use within the laboratory mill, a number of shells have been manufactured; their properties are given in Tables 3–1, 3–2, 3–3, 3–4, and 3–5. The cylindrical shell (Table 3–1) is for use in the foreshortened laboratory mill, which serves as a platform for two-dimensional tumbling mill studies.

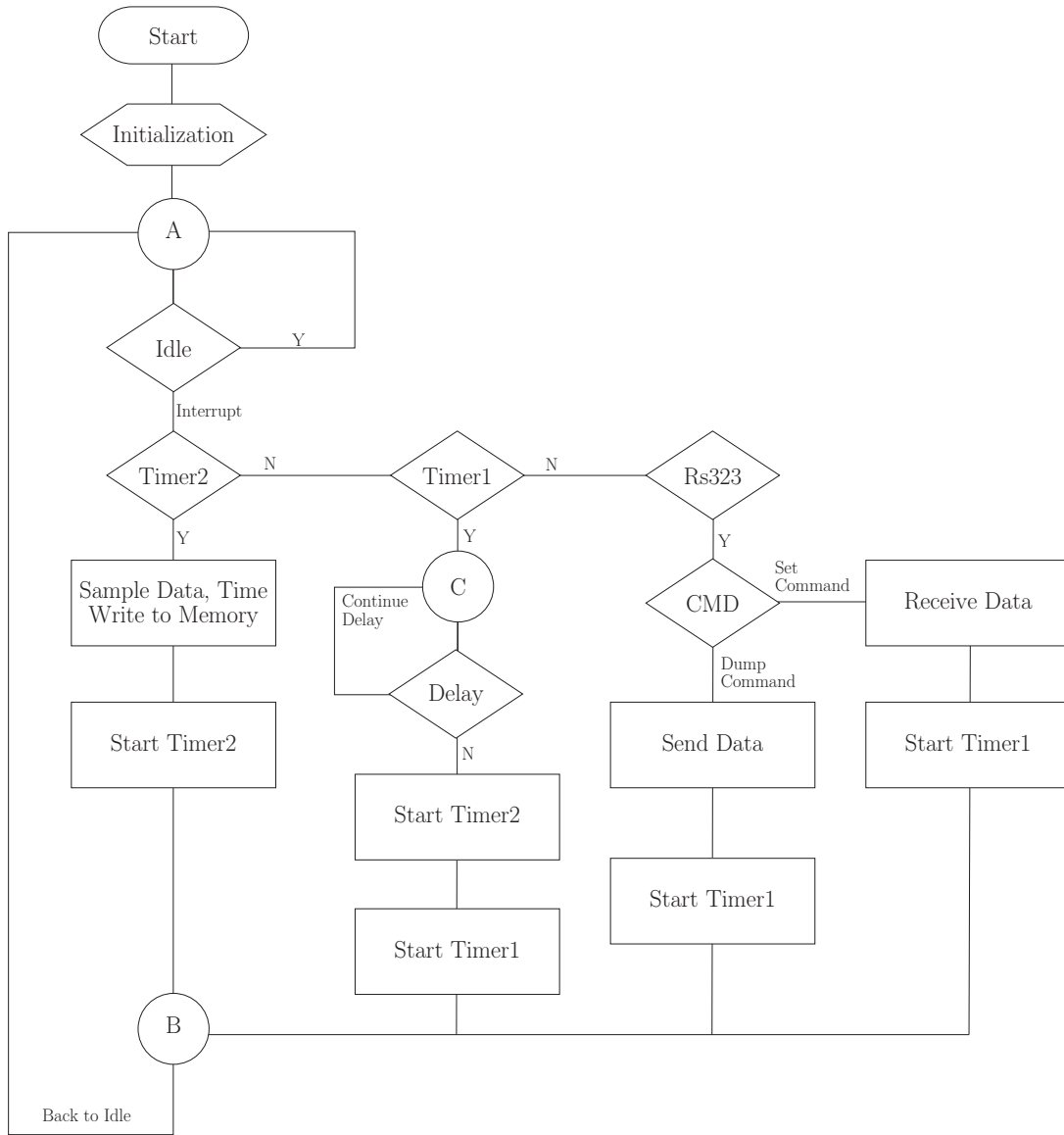


Figure 3-3: The instrumented ball software flowchart

Table 3–1: The properties of the instrumented disk

Shell Material	PVC and Nylon
Shell Diameter (<i>cm</i>)	11.5 ± 0.2
Shell Length (<i>cm</i>)	9.2 ± 0.24
Mass (<i>g</i>) [calculated]	667.07 ± 0.01
Mass (<i>g</i>) [measured]	662.23 ± 2.47
Inertia Tensor($kg \cdot m^2$) [calculated]	$\begin{bmatrix} 0.001738 & -0.000002 & 0.000000 \\ -0.000002 & 0.001114 & 0.000001 \\ 0.000000 & 0.000001 & 0.001741 \end{bmatrix}$ all values ± 0.00048

Table 3–2: The properties of the aluminum instrumented ball

Shell Material	Aluminium
Shell Diameter (<i>cm</i>)	10.0 ± 0.2
Mass (<i>kg</i>) [calculated]	1.2049 ± 0.0005
Mass (<i>kg</i>) [measured]	1.1708 ± 0.0001
Inertia Tensor($kg \cdot m^2$) [calculated]	$\begin{bmatrix} 0.001377 & 0.000003 & 0.000001 \\ 0.000003 & 0.001377 & -0.000001 \\ 0.000001 & -0.000001 & 0.001387 \end{bmatrix}$ all values ± 0.000084

3.2.4 Video System

A video system, developed for the study of charge motion slippage [Piced], is added to the instrumentation package. The video recordings provide additional information. By using image analysis routines, the positions of marked instrumented balls (or disks) and specific charge balls (or disks) can be determined as a function of

Table 3–3: The properties of the aluminum instrumented box

Shell Material	Aluminium
Shell Side Length(<i>cm</i>)	11.5 ± 0.2
Shell Length (<i>cm</i>)	9.2 ± 0.24
Mass (<i>g</i>) [calculated]	667.07 ± 0.01
Mass (<i>g</i>) [measured]	662.23 ± 2.47
Inertia Tensor($kg \cdot m^2$) [calculated]	$\begin{bmatrix} 0.001738 & -0.000002 & 0.000000 \\ -0.000002 & 0.001114 & 0.000001 \\ 0.000000 & 0.000001 & 0.001741 \end{bmatrix}$ all values ± 0.00048

Table 3–4: The properties of the delrin instrumented ball

Shell Material	Polyoxymethylene (POM or Delrin)
Shell Diameter (<i>cm</i>)	10.0 ± 0.2
Mass (<i>kg</i>) [calculated]	0.6960 ± 0.0003
Mass (<i>kg</i>) [measured]	0.6872 ± 0.0001
Inertia Tensor(<i>kg · m²</i>) [calculated]	$\begin{bmatrix} 0.000762 & 0.000000 & -0.000001 \\ 0.000000 & 0.000762 & 0.000000 \\ -0.000001 & 0.000000 & 0.000772 \end{bmatrix}$ all values ± 0.000010

Table 3–5: The properties of the delrin instrumented box

Shell Material	Polyoxymethylene (POM or Delrin)
Shell Side Length (<i>cm</i>)	11.5 ± 0.2
Shell Length (<i>cm</i>)	9.2 ± 0.24
Mass (<i>g</i>) [calculated]	667.07 ± 0.01
Mass (<i>g</i>) [measured]	662.23 ± 2.47
Inertia Tensor(<i>kg · m²</i>) [calculated]	$\begin{bmatrix} 0.001738 & -0.000002 & 0.000000 \\ -0.000002 & 0.001114 & 0.000001 \\ 0.000000 & 0.000001 & 0.001741 \end{bmatrix}$ all values ± 0.00048

time. In particular, these measurements complement the results obtained with the instrumented disk.

The operation of the laboratory mill is recorded by a video camera. Particular elements of the charge are marked with a distinctive color, such as blue or fluorescent yellow. Once the video is transferred to a computer, Matlab is used to decompose and analyze the video, frame by frame. Matlab, a mathematical software package, includes a specialized library of image analysis routines. These routines can locate specific colors in a pixel, identify clusters with the same color—these clusters of uniform color would generally represent an object—and determine the geometric center of the cluster. When the cluster position is determined, a time can be associated with the position since the fame number is known. The camera records images at a rate of

30 Hz. Since the cluster is defined by its color, the choice of color is important. For example, shadows will affect the identification of the clusters since the color of the cluster is perceived as darker, hence different. Consequently, good lighting is necessary to keep the colors uniform. Also, as the analysis can be imprecise for certain frames, human verification and correction of the position is required. The addition of brightly colored points to the video recording help in the visual inspection of the quality of the charge tracker and the identification of problem frames. As before, this process occurs within the Matlab environment.

Similar to the work of Dong and Moys [DM01], the velocity, \mathbf{v}_n , can be determined from the video system measurements.

$$\mathbf{v}_n = \frac{\Delta \mathbf{x}_n}{\tau} = \frac{\mathbf{x}_{n+1} - \mathbf{x}_n}{\tau} \quad (3.1)$$

where τ is the timestep, and \mathbf{x}_n is the position of the tracked particle, at the n^{th} timestep.

3.3 Laboratory Mill

The Comminution Dynamics Lab at McGill University is equipped with a cam driven mill, as illustrated in Figures 3–4 and 3–5 [MLRC06a, MLRC06b, MLRC07, RGT06]. A large diameter aluminum disk is fixed to a shaft mounted on a bearing. The aluminum disk supports two sets of parts. Firstly, the followers for the cam drive are fixed to its face. Secondly, the mill drum (or shell) is bolted to the disk. A Plexiglas face closes the mill at the free end of the drum. The transparent Plexiglas allows for the observation of the charge. Without it, the camera system could not be used. The drum consists of a steel cylinder, with a diameter of 1.524 meters and

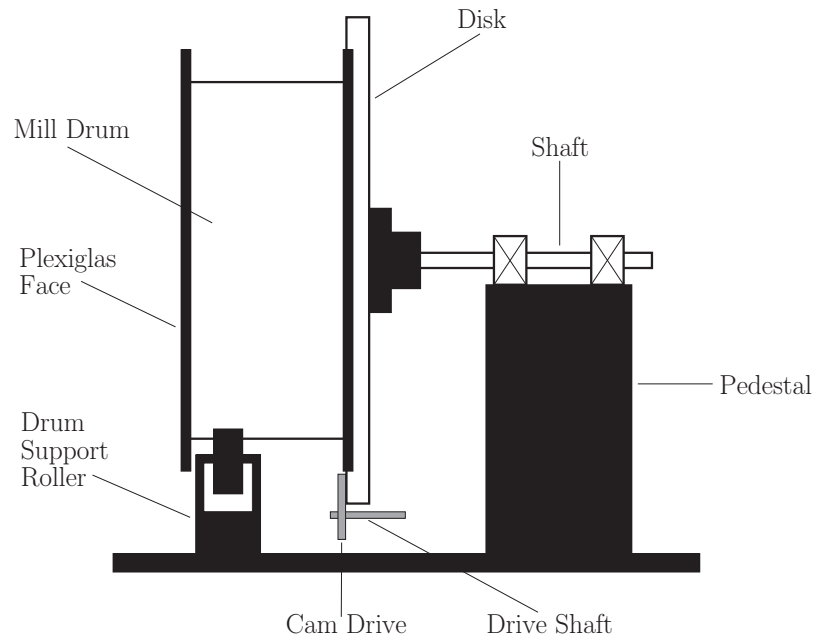


Figure 3-4: The laboratory mill layout

a length of 0.3048 meters. With the use of an insert, the length of the mill can be shortened to a length of 10.16 centimeters. In this configuration, the two-dimensional studies of the charge motion are possible.

3.3.1 Lifters

The laboratory mill is equipped with twelve adjustable triangular lifters, as shown in Figure 3-5. When the lifters are opened up, they flatten, thereby decreasing their effect on the charge. When they are closed, their effect on the charge increases, as illustrated in Figure 1-16. The range of the lifter angle is 0° , which presents a perpendicular face to the charge, to 75° , which present a nearly flat 15° face to the charge.



Figure 3-5: The laboratory mill

3.3.2 Mill Charge

The charge used in the mill consists of either wooden balls or PVC cylinders. The wooden balls are used when operating the full-length mill. The properties of the wooden charge are listed in Table 3-6.

For the two-dimensional studies of the charge motion, a cylindrical charge is used. The properties of this charge are summarized in Table 3-7.

Table 3–6: The properties of the spherical charge used during the 3D laboratory mill experiments

Material	Birch
Diameter (<i>cm</i>)	5.06 ± 0.03
Mass (<i>g</i>) [calculated]	43.8 ± 0.4
Mass (<i>g</i>) [measured]	43.8 ± 2.3
Inertia Tensor(<i>kg · m²</i>) [calculated]	$\begin{bmatrix} 0.000011 & 0.000000 & 0.000000 \\ 0.000000 & 0.000011 & 0.000000 \\ 0.000000 & 0.000000 & 0.000011 \end{bmatrix}$ all values ± 0.000005

Table 3–7: The properties of the cylindrical charge used during the 2D laboratory mill experiments

Material	PVC and Nylon
External Diameter (<i>cm</i>)	11.5 ± 0.2
Length (<i>cm</i>)	9.2 ± 0.2
Mass (<i>g</i>) [calculated]	477.92 ± 0.01
Mass (<i>g</i>) [measured]	484.3 ± 3.6
Inertia Tensor(<i>kg · m²</i>) [calculated]	$\begin{bmatrix} 0.001560 & 0.000000 & 0.000000 \\ 0.000000 & 0.000937 & 0.000000 \\ 0.000000 & 0.000000 & 0.001560 \end{bmatrix}$ all values ± 0.000020

3.4 DEM Simulations

The CORSim DEM simulator was developed by COREM in order to determine the effect of ball make-up strategies in ball mills, through the study of impact energy distributions. Because it is built on top of a general 3D DEM simulator [Ita03], COREM is able to use CORSim for broader research in comminution mills, including breakage efficiency, and mill equipment design. CORSim is divided into three main parts, as shown in Figure 3–6:

1. The DEM engine (DEM simulator), which, once configured, produces a simulation file containing particle positions and contact data over time (the minimal data set).

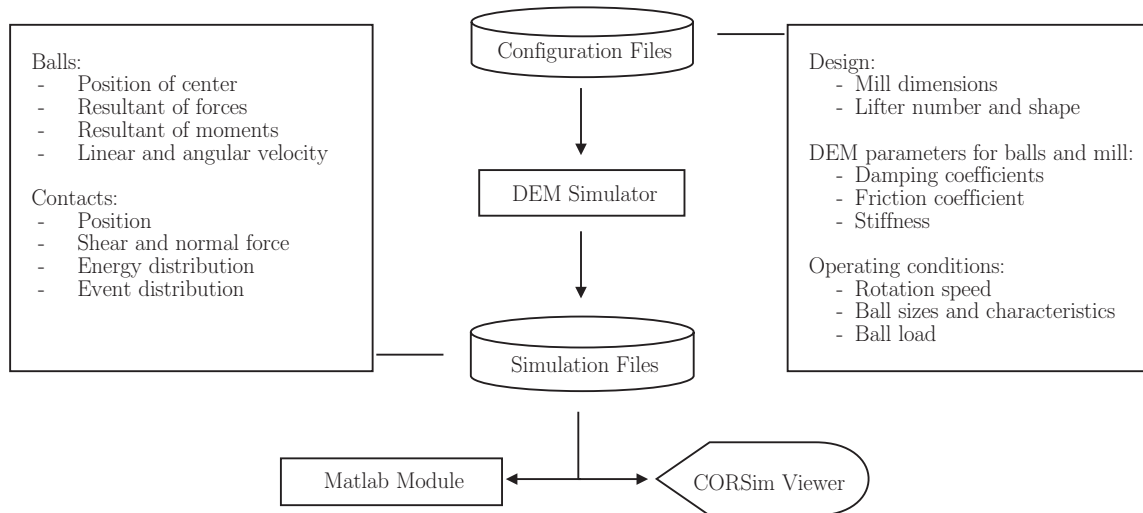


Figure 3–6: The COREM DEM simulator

2. The CORSimViewer, a data display application, which can be used to replay the simulation in real time, and display information from the simulation using pseudo-color. This viewer can also produce videos and still images
3. A Matlab module, which can be used to access raw data from the simulation file, in order to compute and display custom indicators.

A virtue of the simulations is their configurability. Without difficulty, both the two-dimensional and the three-dimensional variants of the mill can be simulated. Furthermore, the quantities determined experimentally (*in-situ*) can be calculated by the DEM (*in-silico*).

3.5 Analysis

Once the simulated data is calculated and the experimental data collected, a number of physical quantities are determined. When observing the laboratory mill

in operation, the stochastic nature of the charge motion is apparent. Also, in their analyses, Rolf and Vongluekiet [RV84], and Gao and Thelen [GT94] produce results in the form of frequencies of impact energies, as shown in Figures 2–7, 2–8, 2–9, 2–11, 2–13, 2–14, and 2–15. There are experimental and simulation analyses based on spatial statistical distributions of the charge, as presented in Figure 2–25. Finally, the specific kinetic energy distributions are determined from the simulations, as illustrated by Figure 2–24. The random nature of the charge motion and the prior work suggest that the use of statistical methods is useful for the analysis of the charge dynamics. Therefore, the analysis of the results presented here is based on the use of statistical methods to find distributions of the data and their moments. A comparison of moments permits the determination of simulations which are in agreement with the experimental results, as is explained below.

3.5.1 Physical Quantities

A tumbling mill can be thought of as an energy transformation machine. At the most basic level, by its action, the mill pushes the charge to gain potential energy, lifting it toward the shoulder. Next, the charge drops toward the toe, converting the potential energy to kinetic energy. Once the charge reaches the impact area, the kinetic energy of the charge is transformed into surface energy, as the ore breaks. Therefore, instead of analyzing the mill in terms of velocities, trajectories and positions, an energy based description is favored.

Using the instrumented ball, in conjunction with the video system, the kinetic energy, E_{ke} , the translational kinetic energy, E_k , the rotational kinetic energy, E_r , the potential energy, E_{pe} , the energy rate-of-change, P , the average mill power draw

per unit mass, p_{charge} , and the velocity, \mathbf{v} , can be determined as a function of time, using the measured and calculated values of the position, \mathbf{v} , the rotation rate, ω , the mass, m , and the moment of inertia, I .

$$E_{ke} = E_k + E_r \quad (3.2)$$

$$E_k = \frac{1}{2}m |\mathbf{v}|^2 \quad (3.3)$$

$$E_r = \frac{1}{2}I^{ij}\omega_i\omega_j \quad (3.4)$$

$$E_p = m(\mathbf{x} - \mathbf{x}_0) \cdot \mathbf{g} \quad (3.5)$$

$$P_i = \dot{E}_i \text{ for } i = k, r, p \quad (3.6)$$

Furthermore, the specific power required to maintain the charge is, as stated by Equation 1.15,

$$p_{charge} = g \bar{X}_{COG} \frac{N_{mill}}{100} N_c \quad (3.7)$$

where \bar{X}_{COG} is the horizontal distance of the center of gravity of the charge from the rotation axis of the mill, g is the gravitational acceleration, N_c is the critical speed of the mill, and N_{mill} is defined by Equation 1.7.

3.5.2 Statistics and Central Moments

Statistics is an inductive process that looks at the sample and predicts the population [RH98]. A number of observations are gathered and analyzed, with the objective of understanding the population. A basic description of a statistical system is the cumulative distribution function, F ,

$$x \mapsto F_X(x) = P(X \leq x) \quad (3.8)$$

which gives the probability, P , of finding a random variable, X , having a value less than x . The probability distribution forms the basis of the analysis, inspired by the analysis of the DEM results, described in Section 2.6.6. Associated with the distribution are a set of numbers called *moments* (central), defined as

$$\bar{x}_n = \int (x - \mu)^n dF(x) \quad n \in [2, \infty) \quad (3.9)$$

where μ is the mean, given by

$$\mu = \bar{x}_1 = \int x dF(x) \quad (3.10)$$

Since the mill is a discretely sampled systems (N samples), a set of analogous numbers, the experimental sample central moments, m_k , and the simulation sample central moments, M_k , can be generated from the experimental (*in situ*) and the simulation *in silico* data, x and \hat{x} respectively [RH98]. Here, the data are any physical quantities defined in Section 3.5.1. For the experimental values, the central moments are

$$m_k(N) = \frac{1}{N} \sum_{i=1}^N (x_i - m_1(N))^k \quad \text{where } k \neq 1 \quad (3.11)$$

$$m_1(N) = \frac{1}{N} \sum_{i=1}^N x_i \quad (3.12)$$

Similarly, the simulation moments are

$$M_k(N) = \frac{1}{N} \sum_{i=1}^N (\hat{x}_i - M_1(N))^k \quad \text{where } k \neq 1 \quad (3.13)$$

$$M_1(N) = \frac{1}{N} \sum_{i=1}^N \hat{x}_i \quad (3.14)$$

The sample mean, \bar{x} , and the sample variance, s , of a random variable, x , are defined as [FW87]

$$\bar{x}_N = \frac{1}{N} \sum_{i=1}^N x \quad (3.15)$$

$$s_N^2 = \frac{1}{N-1} \sum_{i=1}^N (x - \bar{x})^2 \quad (3.16)$$

The sample mean estimates the mean, μ , of a random variable, x , and the sample variance estimates the variance, σ^2 , of a random variable, x .

$$\mu = E(x) \quad (3.17)$$

$$\sigma^2 = E((x - \mu)^2) \quad (3.18)$$

When compared to the definitions of the central sample moments (Equations 3.11, 3.12, 3.13, 3.14), it is observed that the sample mean is the first sample moment, and the sample variance approaches the second moment, as the number of samples increases.

Here, the analysis by McBride *et al.* [MGPC04] and, Mishra and Cheung [MC99] is adopted with some modification. Whereas they use spatial distributions to analyze the mill charge, here the distribution of the time series is adopted. In the case of a steady state distribution, the time series results map can be interpreted together

since, at any point in time, the system looks the same—it is, as a whole, time invariant. For this reason, time is not explicitly part of the analysis.

3.5.3 Confidence in the Moments

Since the data consists of a finite set of *in situ* and *in silico* measurements, the derived moments will only be estimates of the actual values—some error will be present. Therefore, a confidence interval, an error range on the moment, can be determined. If \bar{x} and s are the sample mean and sample standard deviation of a sample of size N , then the mean is within the following range, with a probability of $1 - \alpha$ [FW87]:

$$P\left(\bar{x} + t_{\alpha/2, N-1} \frac{s}{\sqrt{N}} < \mu < \bar{x} + t_{1-\alpha/2, N-1} \frac{s}{\sqrt{N}}\right) = 1 - \alpha \quad (3.19)$$

where $t_{\alpha/2, N-1}$ and $t_{1-\alpha/2, N-1}$ are random variables having a t distribution with $N - 1$ degrees of freedom, and with the following respective probabilities,

$$\begin{aligned} P(\mathbf{t} \geq t_{\alpha/2, N-1}) &= \alpha/2 \\ P(\mathbf{t} \geq t_{1-\alpha/2, N-1}) &= 1 - \alpha/2 \end{aligned} \quad (3.20)$$

Similarly, the variance is within the following range, with a probability of $1 - \alpha$ [FW87]:

$$P\left(\frac{(N-1)s^2}{\chi_{\alpha/2, N-1}^2} < \sigma^2 < \frac{(N-1)s^2}{\chi_{1-\alpha/2, N-1}^2}\right) = 1 - \alpha \quad (3.21)$$

where $\chi_{\alpha/2, N-1}^2$ and $\chi_{1-\alpha/2, N-1}^2$ are random variables having a chi-square distribution having $N - 1$ degrees of freedom, and respective probabilities,

$$\begin{aligned} P(\chi^2 \geq \chi_{\alpha/2, N-1}^2) &= \alpha/2 \\ P(\chi^2 \geq \chi_{1-\alpha/2, N-1}^2) &= 1 - \alpha/2 \end{aligned} \quad (3.22)$$

Thus, the first and second sample central moments, and their error range, can be calculated.

3.5.4 Comparing Distributions

The moments are used to compare distributions. The convergence of moments states that, if F_1 and F_2 are two distribution functions, and if

$$\forall n \geq 1 : \int_0^1 x^n dF_1(x) = \int_0^1 x^n dF_2(x) \quad (3.23)$$

then $F_1 \equiv F_2$ [Chu01], the distributions are equivalent. In certain cases, such as for a distribution over a field of real numbers, a further condition is required, the Carleman condition [Chu01]. Since a physical system is the basis for the *in silico* and *in situ* convergence of moments, it is assumed that the convergence criteria is met. If the estimated *in silico* and *in situ* moments converge, then it is argued that the simulation is an accurate representation of the physical system. Thus, when two measurements (or their derived quantities) are found, such as the *in-situ* and the *in-silico* potential energy, the moments can be determined. If the moments prove to be equivalent, within error, it is stated that the measurements are equivalent. This supports the argument that the simulation is a faithful representation of the experimental results. However, this remains a weak argument if it is only based on one measurement. If the above condition applies to all measurements, a strong argument for equivalence is made.

$$\text{As } N \rightarrow \infty, \text{ then } M_k(N) \rightarrow m_k(N) \text{ for all } k \quad (3.24)$$

Therefore, the matching of all *in silico* and *in situ* moments, for all measurements, is sought. In doing so, all distributions are matched. If all the statistics are the same, then the dynamics are the same.

3.5.5 Comparative Study

The method of matching moments is useful within the context of a comparative study. The laboratory mill is a physical system with a given set, A , of parameters. The parameters include the diameter of the mill, D , the length of the mill, L , the gravitational acceleration, g , and the rotational speed of the mill, N .

$$A = \{D, L, g, N, \dots\} \quad (3.25)$$

The set of physical parameters can only be known with a finite degree of precision and accuracy, represented by the set, \hat{A} , an estimate of the physical set A . In addition, not all parameters are included in the estimated set, \hat{A} . \hat{A} is a smaller set than A . For example, altitude and atmospheric effects, which are present in the physical system, are not included in the estimated parameters since they are not part of the simulation.

$$\hat{A} = \{\hat{D}, \hat{L}, \hat{g}, \hat{N}, \dots\} \quad (3.26)$$

In addition to the set of estimated physical parameters \hat{A} , the DEM model parameters, B , which include the time-step, τ , the type of contact model, \mathcal{F} , are known.

$$B = \{\tau, \Omega, \mathcal{F}\} \quad (3.27)$$

When the lab mill is operated, the set of parameters A define the system and how it behaves. From this system, a set of *in situ* measurements, $x_1 \dots x_N$ and their derived

quantities, the moments $(m_1 \dots m_L)$, are obtained.

$$A \xrightarrow{\text{experiment}} \{x_1, \dots, x_N\} \longrightarrow \{m_1(N), \dots, m_L(N)\} \quad (3.28)$$

The act of performing the experiment on the physical system, collecting the measurements and determining the derived physical quantities is represented by the plant operation, \mathcal{P} . Again, the defined set of physical parameters give, by virtue of the physics, a set of derived quantities.

$$\mathcal{P}(A) = \{m_1(N), \dots, m_L(N)\} \quad (3.29)$$

Similarly, the simulation process takes the estimated physical parameters, \hat{A} , in addition to the simulation parameters, B , and computes a number of states and *in silico* measurements, $\hat{x}_1 \dots \hat{x}_N$ and their derived quantities, the moments $(M_1 \dots M_L)$.

$$\hat{A}, B \xrightarrow{\text{simulation}} \{\hat{x}_1, \dots, \hat{x}_N\} \longrightarrow \{M_1(N), \dots, M_L(N)\} \quad (3.30)$$

The process of simulating the physical system, and calculating a number of states and derived quantities is represented by the simulation operation, \mathcal{S} . With the set of estimated physical parameters and simulator parameters, the simulation computes a set of derived quantities.

$$\mathcal{S}(\hat{A}, B) = \{M_1(N), \dots, M_L(N)\} \quad (3.31)$$

If it is assumed that the estimated physical parameters \hat{A} are equivalent, for the purposes of the analysis, to the physical parameters, A , and if the simulation results, $M_1 \dots M_L$, within error, converge to the measured results, $m_1 \dots m_L$, with the caveat

that the analysis used to obtain the results be the same, then it is argued that simulation, $\mathcal{S}(\cdot, B)$ is an accurate representation of the physics, $\mathcal{P}(\cdot)$. This methodology, based on Equation 3.24, seeks consistency between the models and the mills, through convergence of the *in silico* and *in situ* moments. When the moments converge, the distributions also converge. If all distributions converge, then the dynamics underlying the processes which produce the distributions are equivalent.

If

$$\hat{A} \cong A$$

and if

$$\{M_1(N), \dots, M_L(N)\} \longrightarrow \{m_1(N), \dots, m_L(N)\} \quad (3.32)$$

then

$$\mathcal{S}(\cdot, B) \equiv \mathcal{P}(\cdot),$$

3.5.6 Assumptions

With regards to both the simulation and the experimental results, a number of assumptions have been made. Firstly, the *in silico* and *in situ* processes are steady state. No time variation of any average quantity or the statistics is expected. Secondly, though the nature of the distributions is unknown, it is assumed that the expressions for the confidence limits of the first and second moments are valid. Though this is likely incorrect, as these expressions assume a normal distribution of the random variable, the confidence limit expressions (Equations 3.19 and 3.21) provide, at the very least, an estimate of the actual confidence limits. Thirdly, any

two-dimensional results have no dependence on the axial coordinate. Since the two-dimensional mill is a shortened version of the three-dimensional mill, some small motion in the axial direction, as well as small rotations out of the plane of the mill disk, exist and are neglected. Next, no breakage or grinding is considered though some breakage and abrasion residue is present—one example is the wood dust generated when using the wooden charge. Finally, the time series of instrument results are equivalent to the instantaneous spatial results of the instrument. In other words, what is measured over time, as the instrument follows its trajectory, is equivalent to having multiple instrumented balls at a point in time, at the positions defined by the trajectory of the instrumented ball. This argument exploits the time symmetry of a steady state condition where instantaneous differences on a microscopic level are washed out at the macroscopic level, particularly when in the regime of large statistics. In certain case, this assumption is extended. The time series behavior of an element of the charge (here, the instrument) is equivalent to the spatial behavior of the whole charge, mass properties notwithstanding. For example, the determination of the position of the instrumented ball, over a number of rotations of the mill, is assumed to accurately represent an instantaneous configuration of the charge.

3.6 Summary

The instrumented ball, in conjunction with other instruments—in this case, a camera system—can produce a number of *in-situ* measurements pertaining to the charge. Furthermore, the designed instrumented ball is capable of measuring the rotations rates (3-axis). This type of measurement is new to tumbling mills, with the advantage of providing the possibility of easily calculating an energy term (Equation

3.4). Similarly, a DEM model can be programmed to produce an output equivalent to the instrument measurements, the *in-silico* measurements. By construction, the laboratory mill, the charge, and the instrumented ball geometry are simple, thereby simplifying the implementation of the simulation. The statistical analysis of both the *in-situ* and the *in-silico* measurements each give a set of moments. If the simulation is a faithful model of the mill dynamics, then, within error, the moments will agree. The matching of *in-situ* and *in-silico* moments can be used to identify an accurate DEM model of the mill.

CHAPTER 4

Observations and Results

Based on the measurements provided by the instrumented ball, in conjunction with the camera system, a number of physical quantities are determined. A subset of these measurements—the rotation rates in particular—are obtained using an instrumented ball evolving with the charge. The rotation rates have not been measured prior to the development of this instrumented ball. The results are presented here in the form of energies, as defined by Equations 3.3, 3.4 and 3.5. These energies can also be simulated. From both the simulated and experimental energies, the mean and the standard deviation, collectively referred to here as the moments, can be found. The comparison between simulated and experimental moments of the energies allow the identification of accurate simulations. Any differences point to areas where more development is needed. Prior to this, the performance characteristics of the instrumented ball are given.

4.1 Instrumentation

4.1.1 Instrumented Ball

To verify the operation of the rotation rate sensors, the instrumented ball is fixed to the shell of the empty mill. The mill is rotated at different known rates. At the same time, the instrumented ball collects data. The mill rotation rates, as measured externally and as measured by the instrumented ball, are compared in Figure 4-1 [MLR⁺08]. A properly operating instrumented ball must agree with the

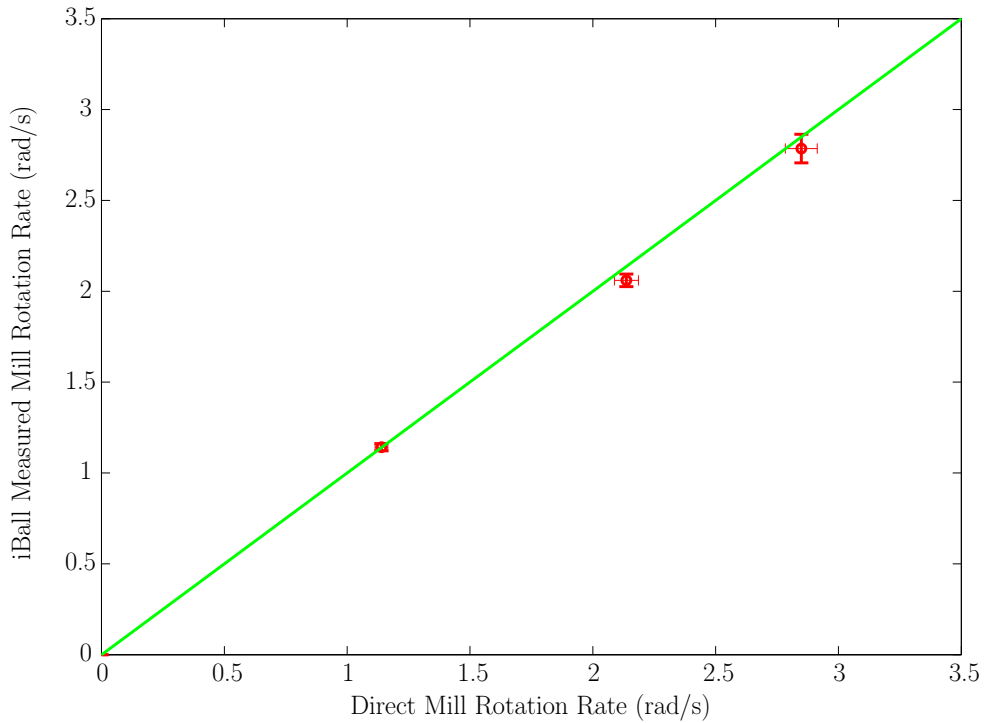


Figure 4-1: A verification of the rotation sensor

external rotation rate measurement. As expected, the instrumented ball measures rotation rates accurately, within error (see Equation 3.19 and 3.21, with a 95 percent confidence limit). When the mill is stationary, the rate sensors output is noise. This signal is shown in Figure 4-2.

The cumulative distribution of the noise is plotted in Figure 4-3. In addition, a Gaussian distribution is fit to the data. Therefore, the noise present in the rotation rate sensors can be accurately characterized as Gaussian noise, with properties summarized in Table 4-1. Furthermore, the measurement limit of the rotation rate sensor is known. Each axis can measure a rotation rate less than 5.23 rad/s . Above this rate, the sensor output saturates. To account for these sensor limitations, noise

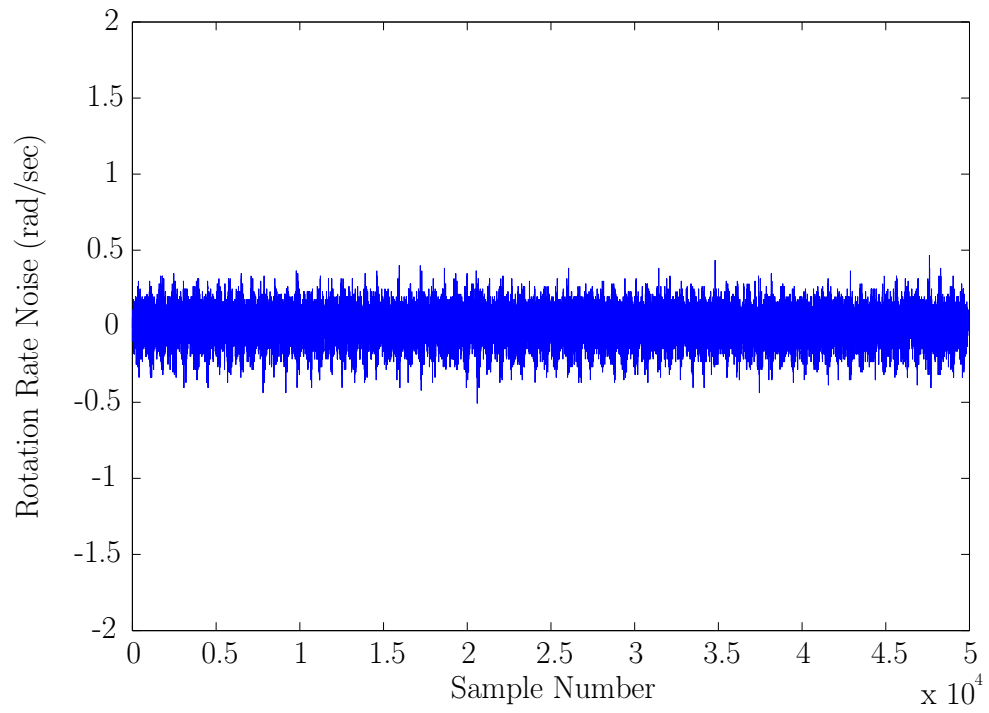


Figure 4-2: Time series of the rotation rate sensor noise (y-axis)

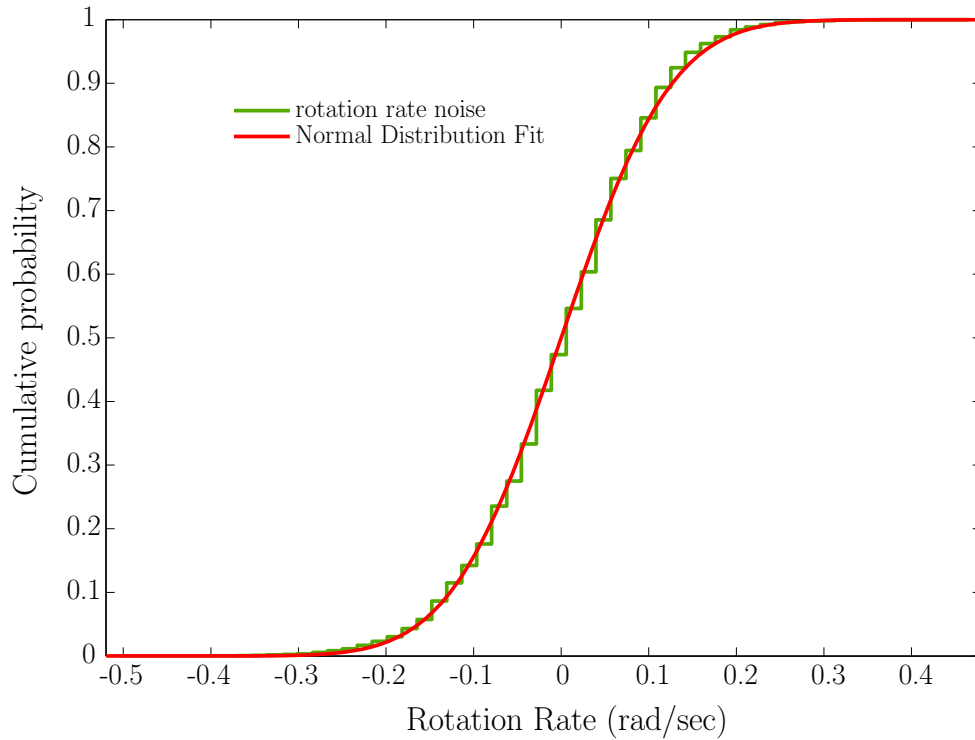


Figure 4-3: the cumulative distribution of the sensor noise (y-axis)

is added to the DEM rotation results and a saturation filter clips the simulated rotation rate measurements, mirroring the operation of the sensor. Thus, the comparison of experimental and simulated results is between similar values.

Table 4-1: The rotation rate sensor noise characteristics

Parameter	Estimate (rad/s)	Standard Error (rad/s)
Mean	6.02×10^{-17}	4.43×10^{-4}
Standard Deviation	9.89×10^{-2}	3.13×10^{-4}

4.1.2 Camera System

The camera system provides the capability to track the positions of the marked instrumented ball as a function of time, as pictured in Figure 4-4. From the Matlab



Figure 4–4: A picture of the operating mill with a measured instrumented ball trajectory overlay

analysis, the camera system is known to give accurate positions of the tracked target [Piccd].

4.2 Mill

4.2.1 Spherical Charge Configuration

4.2.2 Instrumented Ball

In this section, the three-dimensional configuration of the mill is used as the experimental platform. The charge of the mill consists of spherical, wooden balls. The properties of this charge are summarized in Table 3–6. The number of balls used is constant, giving a fractional fill level equal to 30 percent. The adjustable lifter angle is set to 0° , such that a perpendicular lifter face is presented to the charge.

Table 4–2: *In-Silico* energy rates-of-change statistics

Year	Speed	$E_{rot} (J)$	$95 \sigma_{rot} (J)$
2006	60	0.0430	0.0304
	70	0.0533	0.0332
2007	60	0.0438	0.0305
	70	0.0548	0.0326

4.2.3 Repeatability

When the mill (3D configuration) is operated at 60 and 70 percent critical speed, with the aluminum instrumented ball added to the wooden charge, the distribution of the rotational kinetic energy, as defined by Equation 3.4, is obtained. The same configurations were repeated six months later. The results are shown in Figure 4–5, and the moments of the distributions are compared in Table 4–2. The differences between the moments are less than 2 percent. Therefore, repeated experiments produce the same distribution; it is a characteristic of the charge, for a given configuration of the mill. This result is extended to the translational kinetic energy and the potential energy. The use of the translational kinetic energy and potential energy distributions as characteristics of the charge is supported by the results obtained by McBride *et al.* [MGPC04]. In their work, the spatial distributions of the charge and the velocity distributions over the cross-section of the mill (experimental and simulated) do not change and are used as a basis for comparison (Figure 2–25). If these results are integrated over the whole cross-sectional area, what is obtained is a distribution of the velocities (or positions), at a point in time, for the whole mill area. In steady state, this distribution at a point in time is assumed equivalent to the distribution of the values measured over time for one of the elements (the instrumented ball in this

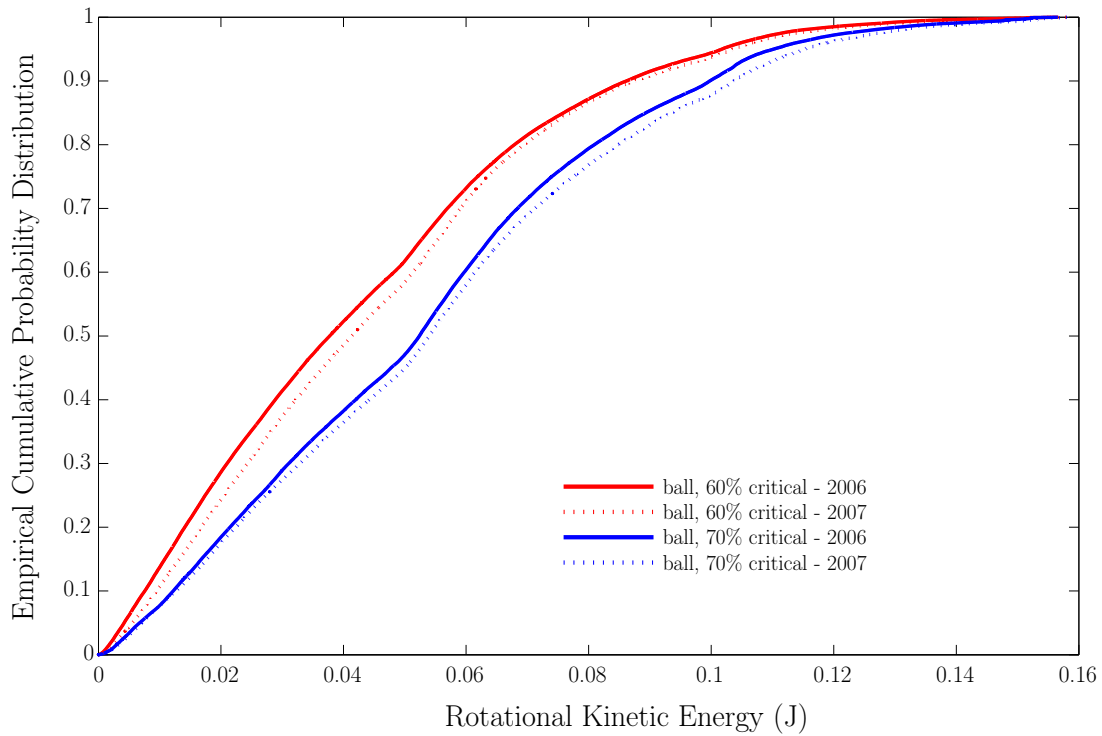


Figure 4-5: The rotational kinetic energy distribution repeatability [MLRC07]

case), as is argued in Section 3.5.6. The time-series result is what is obtained when the instrumented ball and camera system data are analyzed. Therefore, the results obtained here with the instruments characterize the charge, as do the McBride *et al.* results, as long as the mill remains in steady state. To some extent, the work of Mishra and Cheung (Figure 2-24) supports this statement, though this is a weaker argument due to the observed variability in their distributions.

In the three dimensional configuration, it is possible to determine the measured mean rotational kinetic energy of the instrumented ball. In Figure 4-6, the mean rotational kinetic energy is plotted as a function of the speed of the mill. From this

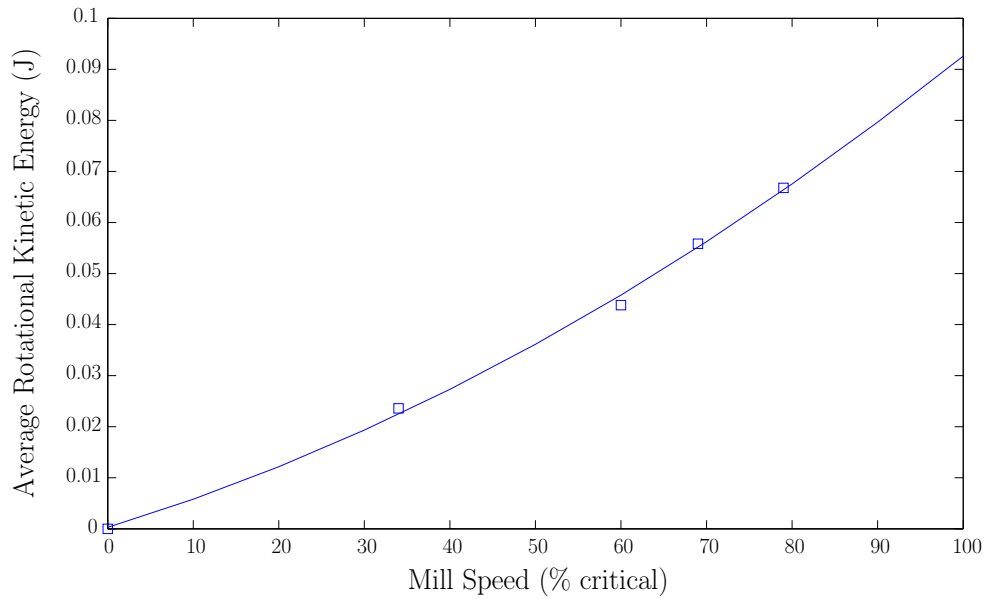


Figure 4-6: The average experimental rotational kinetic energy of the instrumented ball at different mill speeds

plot, it is noted that the rotational kinetic energy smoothly varies with the speed, in parallel to observations of the mean energy, described in Section 5.2.

4.2.4 Cylindrical Charge Configuration

4.2.5 Instrumented Ball

In this section, the instrumented ball, in conjunction with the camera system, is used within the two-dimensional configuration of the mill. Table 4-3 gives the mill parameters. The same configuration is simulated using the CORSim model of the

Table 4-3: The 2D mill parameters

Mill Speed (percent critical)	38 ± 2
Number of 2D Instrumented Balls	2
Number of 2D Charge Elements	37
Lifter Angle (degrees)	75

mill. The experimental results are presented first, followed by the CORSim results. Once the laboratory mill is stopped, and the data downloaded, the experimental translational kinetic energy (Equation 3.3), the experimental rotational kinetic energy (Equation 3.4) and the experimental potential energy (Equation 3.5) can be determined, as a function of the instrumented ball position. They are plotted in Figures 4–7, 4–8 and 4–9, respectively. The spatial distribution of the translational kinetic energy does not show as much variation as expected. This is caused by an extreme event dominating the upper range of the color scale. In terms for kinetic energy results, these are comparable to the simulation (see Section 4.2.7). The time derivative of the kinetic and potential energies can be calculated since each measurement has a time-stamp. The distribution of each of the energy terms, as defined by Equation 3.6, is plotted. The probability distribution of the time rate-of-change of the translational kinetic energy, the rotational kinetic energy and the potential energy are plotted in Figures 4–10, 4–11 and 4–12, respectively. The mean and the standard deviation of the rates-of-change of are given in Table 4–4. In this table, it is observed that the mean values of all the energy terms are near zero and are much smaller than the standard deviations. Though energy is being exchanged, as the large standard deviations indicate, the net amount of energy exchanged over time, between the instrumented ball and its environment, is near zero. This supports the argument that the laboratory mill is operating in a steady state. This conclusion is based on the instrumented ball results, which are extended to the charge. At any given moment in time, some elements of the charge receive energy, while others lose energy, giving a net energy exchange equal to zero.

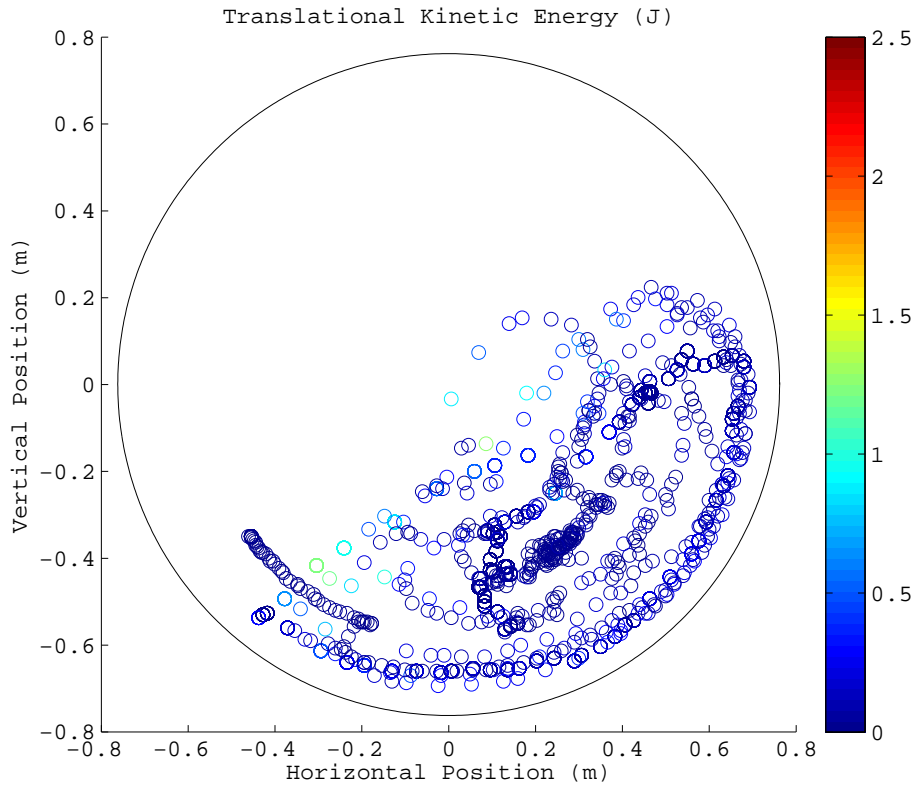


Figure 4–7: The spatial distribution of the translational kinetic energy—
instrumented ball

Table 4–4: *In-Situ* energy rates-of-change statistics

	$d\bar{E}/dt$ (W)	95 % confidence limits (W) (Equation 3.19)	$S_{dE/dt}$ (W)	95 % confidence limits (W) (Equation 3.21)
E_k	0.0841	(-0.5566, 0.7248)	16.9754	(16.5343, 17.4408)
E_r	-7.2605×10^{-5}	(-0.0045, 0.0044)	0.9573	(0.9542, 0.9605)
E_p	-0.0604	(-0.2500, 0.1292)	4.4301	(4.3000, 4.5683)

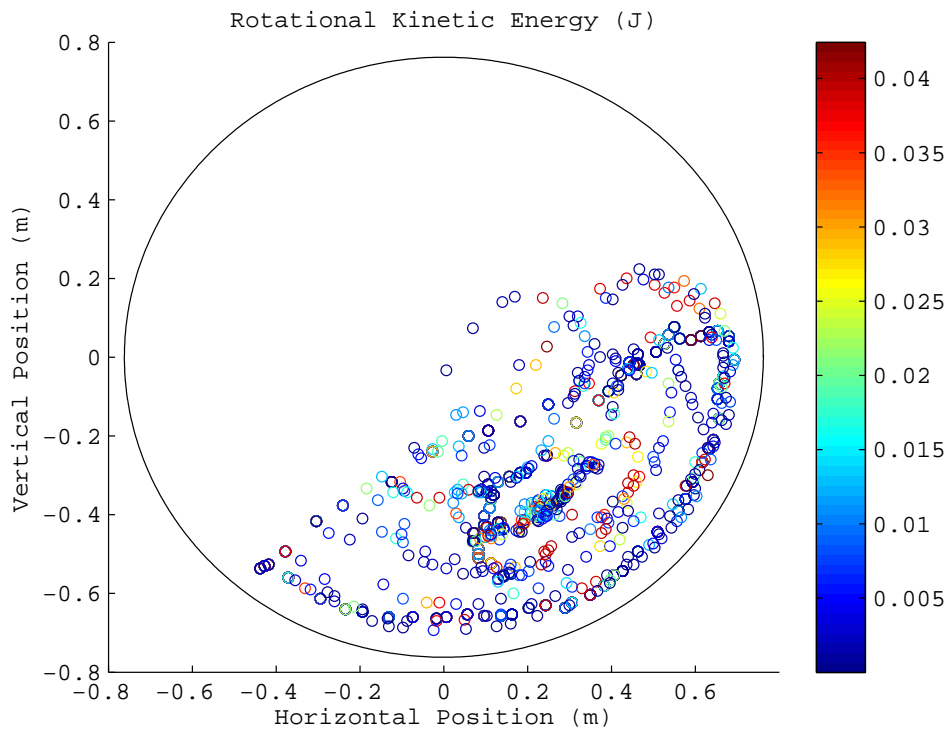


Figure 4-8: The spatial distribution of the rotational kinetic energy—instrumented ball

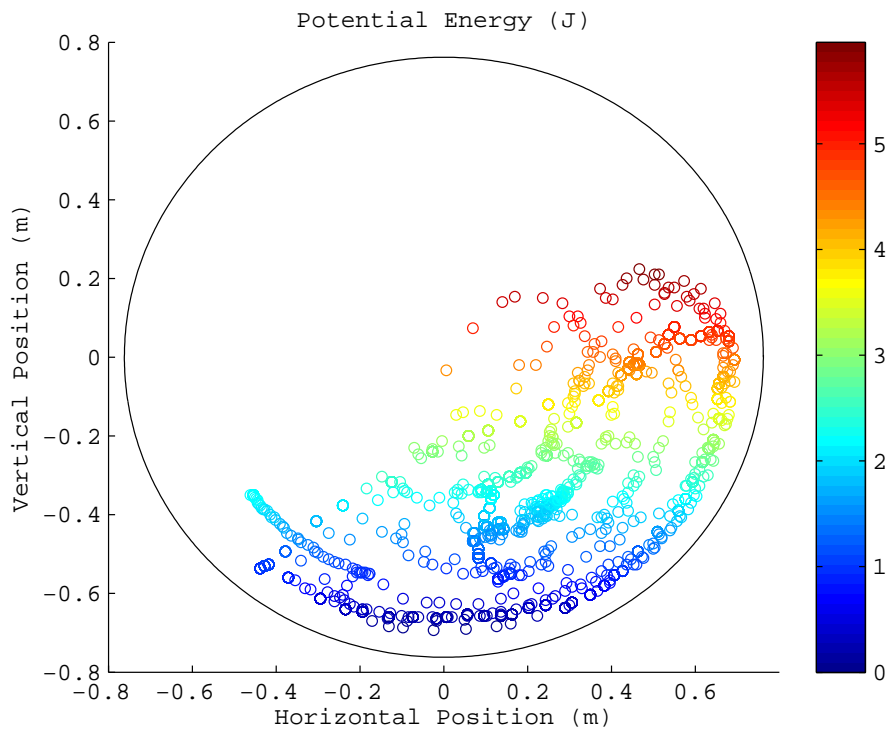


Figure 4–9: The spatial distribution of the potential energy—instrumented ball

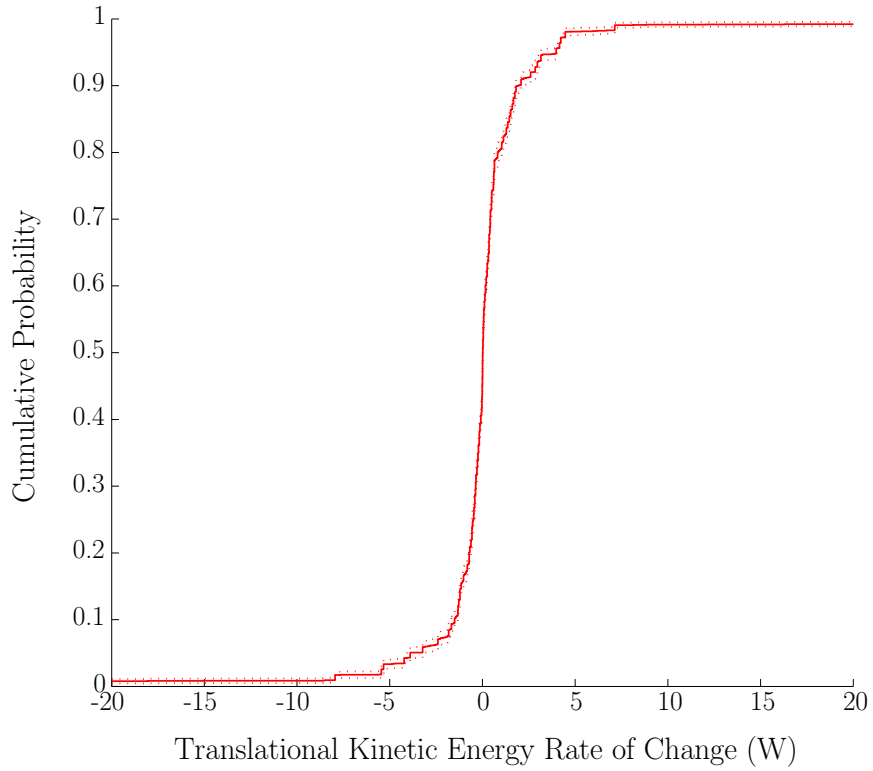


Figure 4-10: The probability distribution of the time rate-of-change of the translational kinetic energy

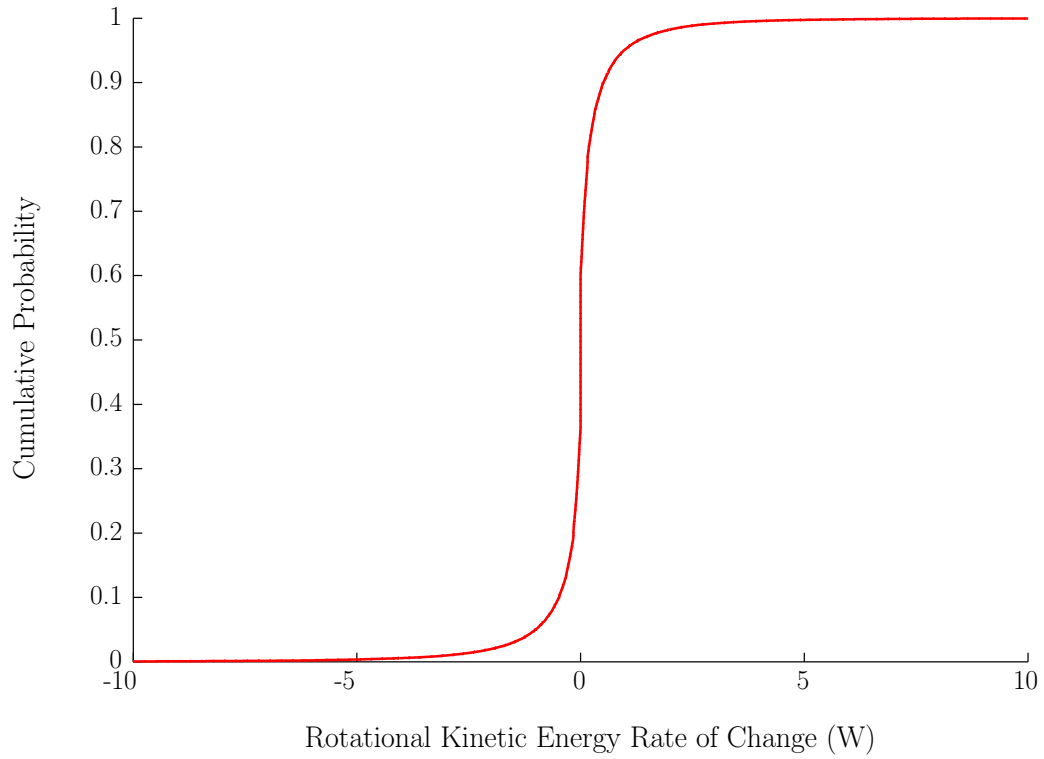


Figure 4–11: The probability distribution of the time rate-of-change of the rotational kinetic energy

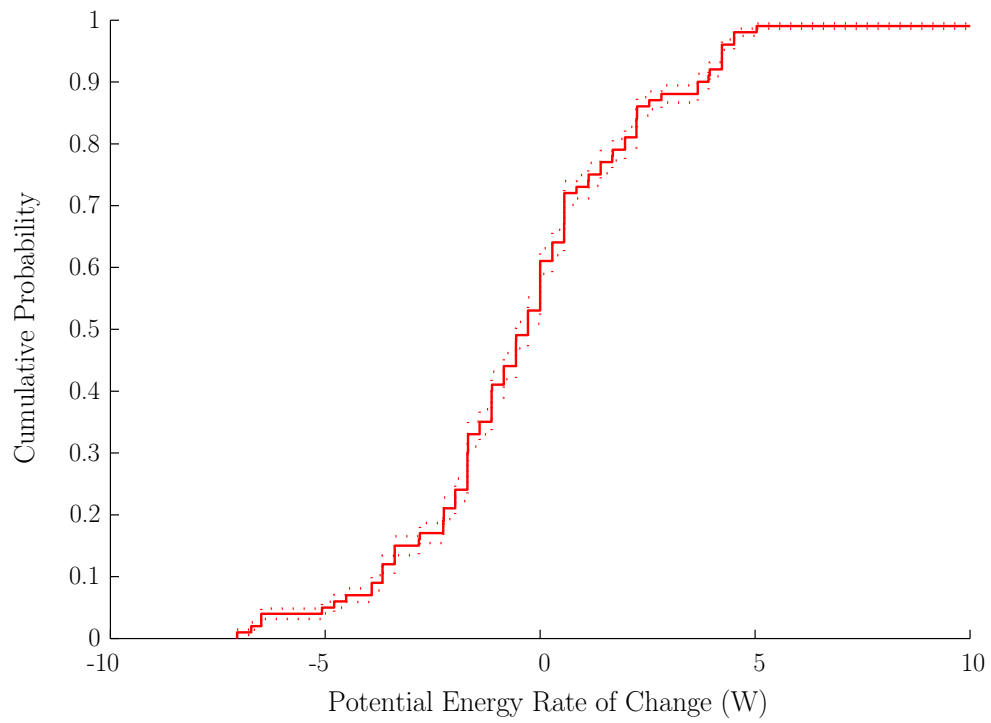


Figure 4–12: The probability distribution of the time rate-of-change of the potential energy

Table 4–5: Initial CORSim model parameters

Model Parameter	Value
Friction	0.35
Normal viscous damping ratio	0.4
Shear viscous damping ratio	0.4
Normal stiffness (N/m)	10000
Shear stiffness (N/m)	10000

On examining the distribution of the rotational kinetic energy (Figure 4–8), a range of energy values, ranging from low (near 0 J) to high (0.04 J), is noted. Were the instrumented ball to rotate at the same rate as the mill, its rotational kinetic energy would be 0.011 J. Therefore, in the mill, the instrumented ball is observed to rotate at rates larger than the rotation rate of the mill. Also, in certain cases, the instrumented ball nearly stops rotating. This result, and the ability to obtain it, with the help of the instrumented ball, is new to tumbling mills.

4.2.6 CORSIM

Parallel to the experimental results, a simulation reproduces the laboratory mill. The simulation parameters are given in Table 4–5. These parameters are based on the recommendation of the simulation specialists at COREM, the developers of CORSim. These values are within the ranges published in the literature [Kre10, LLC99, Rab95, MT61, FLFC98]. One of the elements simulated is the instrumented ball. From the recorded states of the simulated instrumented ball, the translational kinetic energy, the rotational kinetic energy and the potential energy are determined and plotted, as a function of position, in Figures 4–13, 4–14, 4–15, respectively. As is the case for the experimental results, the time rates-of-change of the translational kinetic energy, the

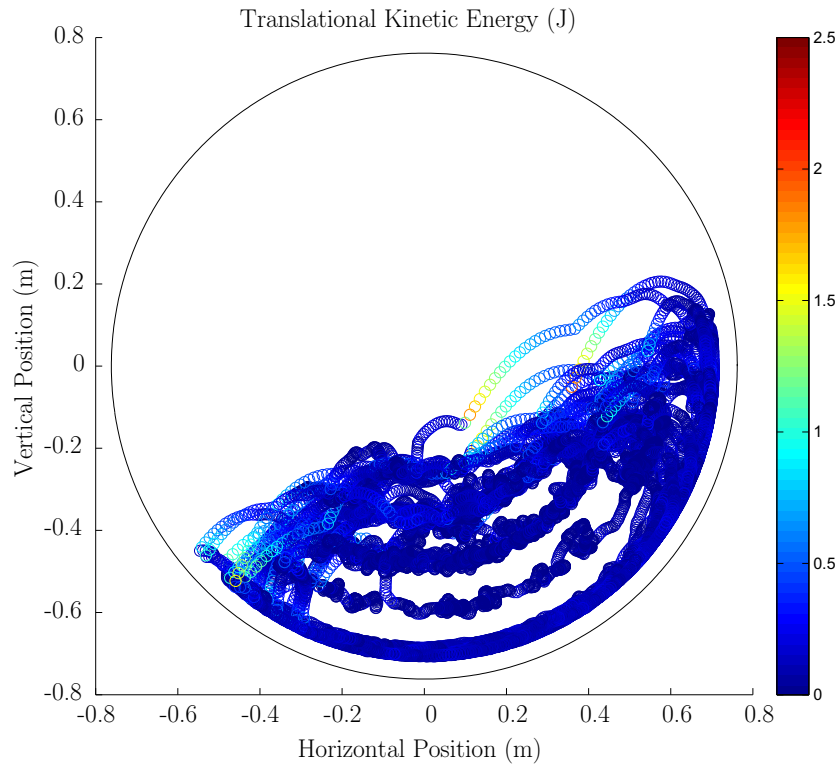


Figure 4–13: The spatial distribution of the translational kinetic energy—CORSim rotational kinetic energy and the potential energy can be calculated. They are plotted in Figures 4–16, 4–17 and 4–18, respectively. The mean and standard deviation of the simulated time rates-of-change are listed in Table 4–6. In keeping with the experimental results, the means of the simulated translational kinetic energy, the simulated rotational kinetic energy and the simulated potential energy are nearly zero, whereas their standard deviations are large. The energy terms fluctuate, at times increasing, at other times decreasing, but over time, the net energy exchange is effectively zero. Again, this observation supports the argument that, similarly to the experimental case, the simulation is steady state.

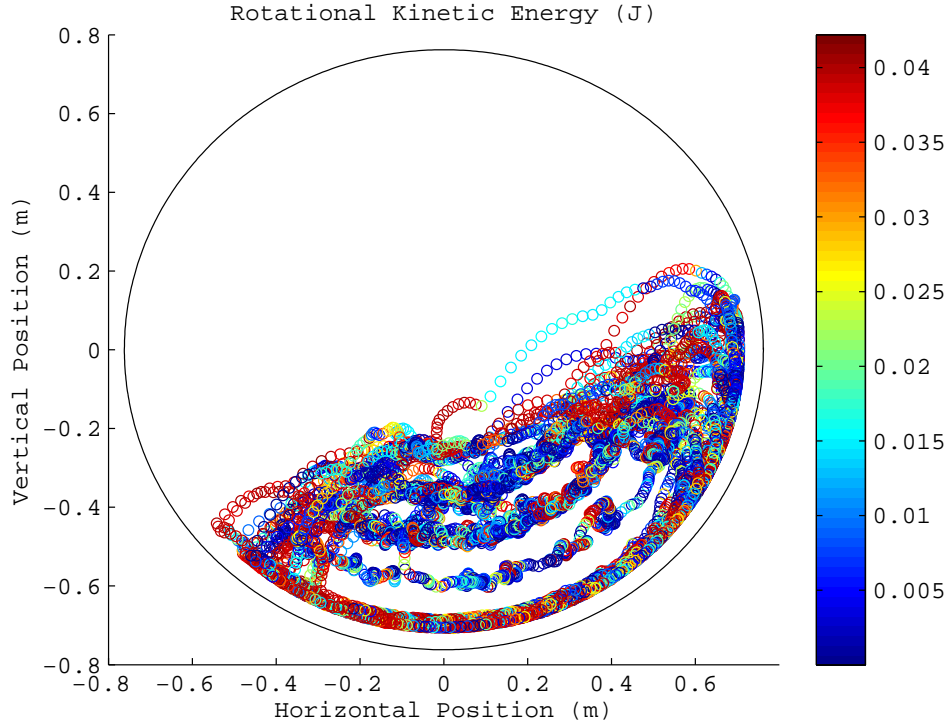


Figure 4–14: The spatial distribution of the rotational kinetic energy—CORSim

Table 4–6: *In-Silico* energy rates-of-change statistics

	$d\bar{E}/dt$ (W)	95 % confidence limits (W) (Equation 3.19)	$S_{dE/dt}$ (W)	95 % confidence limits (W) (Equation 3.21)
E_k	1.1×10^{-4}	(-0.071459, 0.071682)	5.8371	(5.786954, 5.888176)
E_r	-3.8×10^{-5}	(-0.019890, 0.019813)	1.6191	(1.605146, 1.633222)
E_p	-0.0172	(-0.047767, 0.013433)	2.4957	(2.474218, 2.517495)

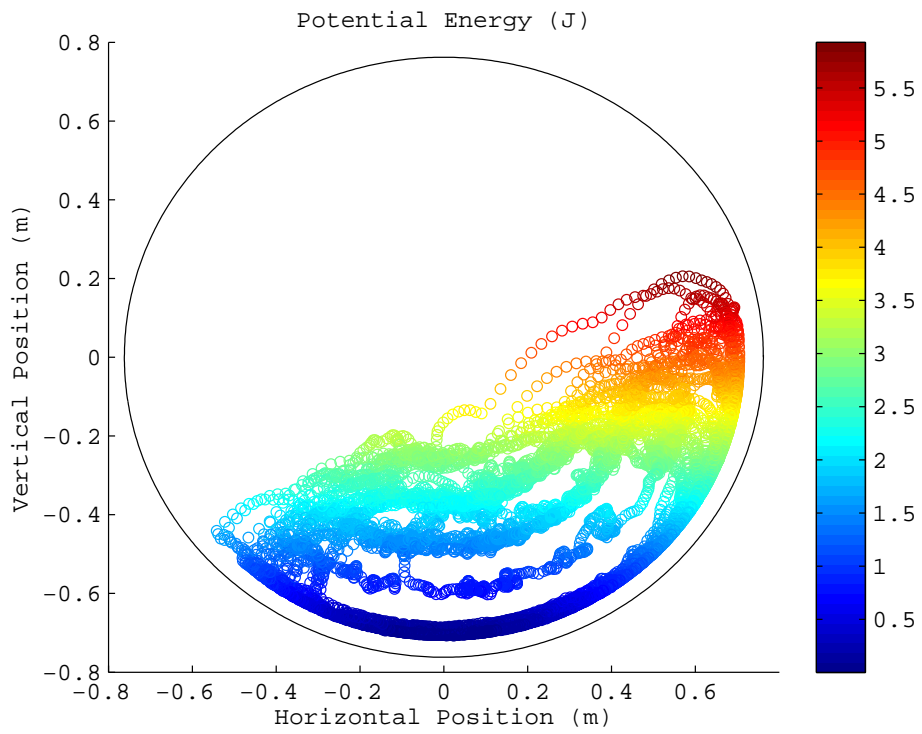


Figure 4–15: The spatial distribution of the potential energy—CORSim

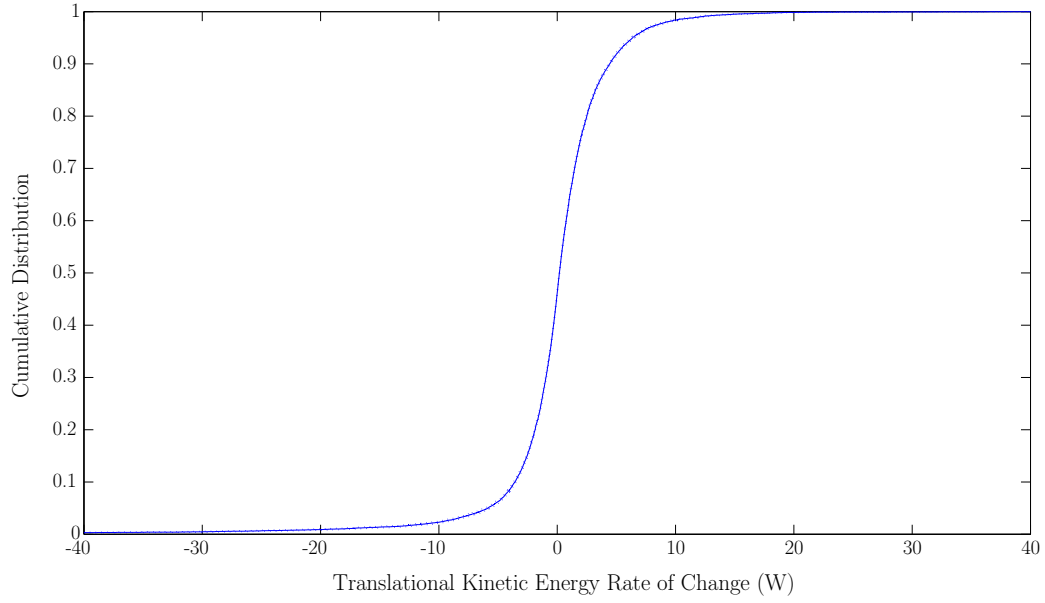


Figure 4–16: The probability distribution of the time rate-of-change of the translational kinetic energy

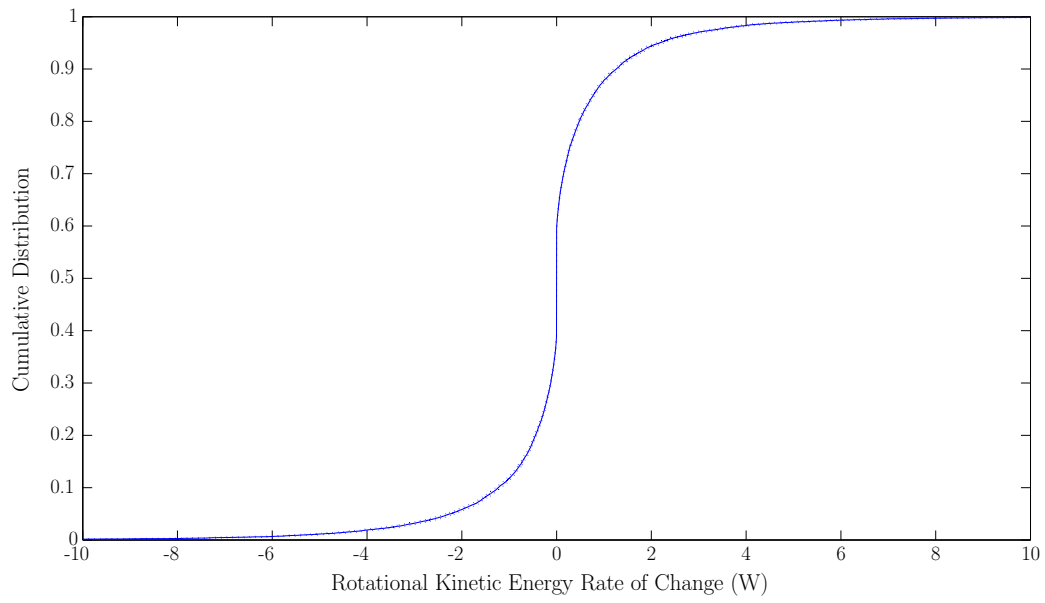


Figure 4–17: The probability distribution of the time rate-of-change of the rotational kinetic energy

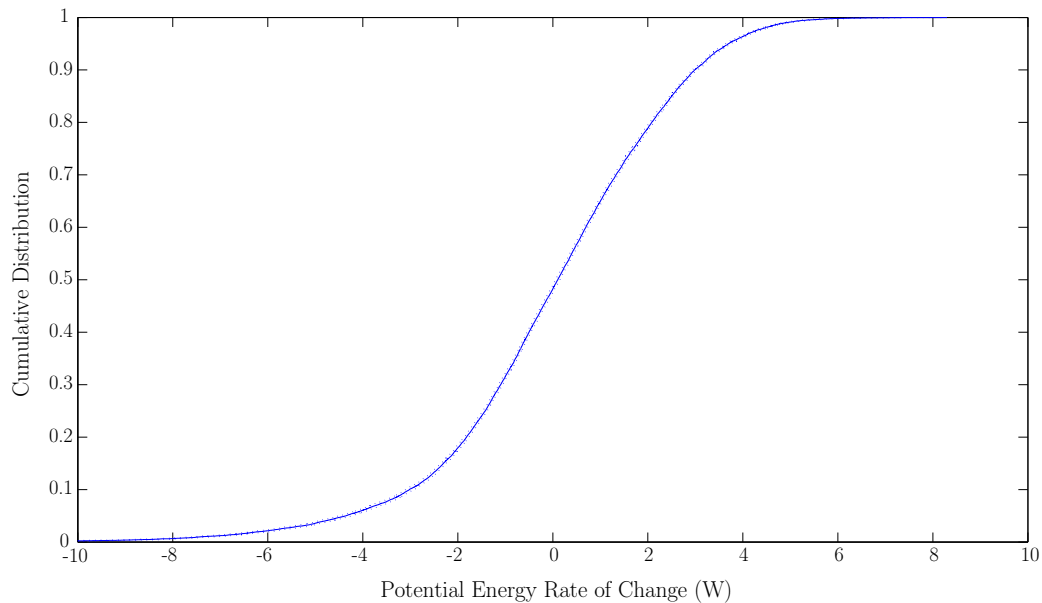


Figure 4–18: The probability distribution of the time rate-of-change of the potential energy

4.2.7 Instrumented Ball and CORSim

For the purpose of comparison, both the experimental and simulated cumulative distributions of the translational kinetic energy, the rotational kinetic energy and the potential energy are plotted in Figures 4–19, 4–20 and 4–21. In all Figures, differences are observed. The differences are confirmed when the measurands are examined, as shown in Tables 4–7 and 4–8. No agreement between *all* measurands can be found—the simulation fails to accurately reproduce the experimental results.

Since the geometry of the mill is simple, the simulation can reproduce it, including the geometry at the ends; it is not considered to be the source of the differences. Transients are not the cause of the differences since, in both the experimental and simulated cases, the condition of steady state has been established. However, the

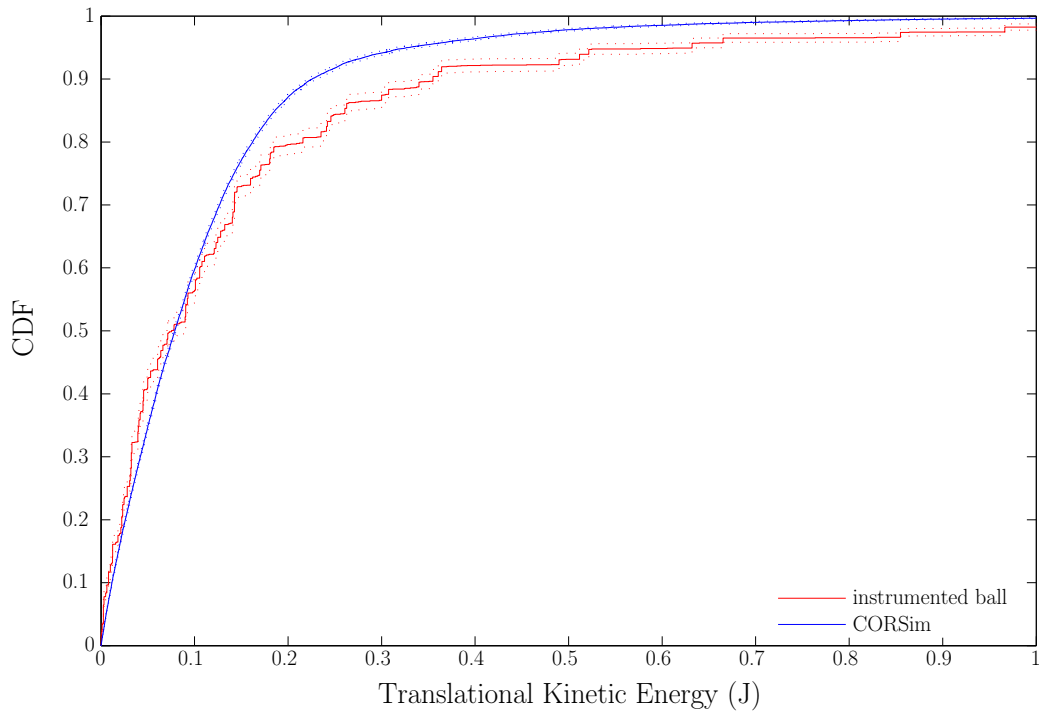


Figure 4–19: The cumulative distribution of the translational kinetic energy

contact model and its parameters may not reflect the forces within the mill. This is addressed in Section 4.2.8.

4.2.8 Free Parameter DEM

The lack of agreement between the laboratory measurements and the simulation is problematic. The methodology described in Section 3.5 was meant to resolve this by identifying the simulations in agreement with the measurements. This is accomplished as follows. First, a set of simulations, over four thousand in this case, is prepared and run. The simulation parameters range over the values given in Table 4–9. Next, the first and second moments are calculated for the translational kinetic energy, the rotational kinetic energy, the potential energy and the specific power,

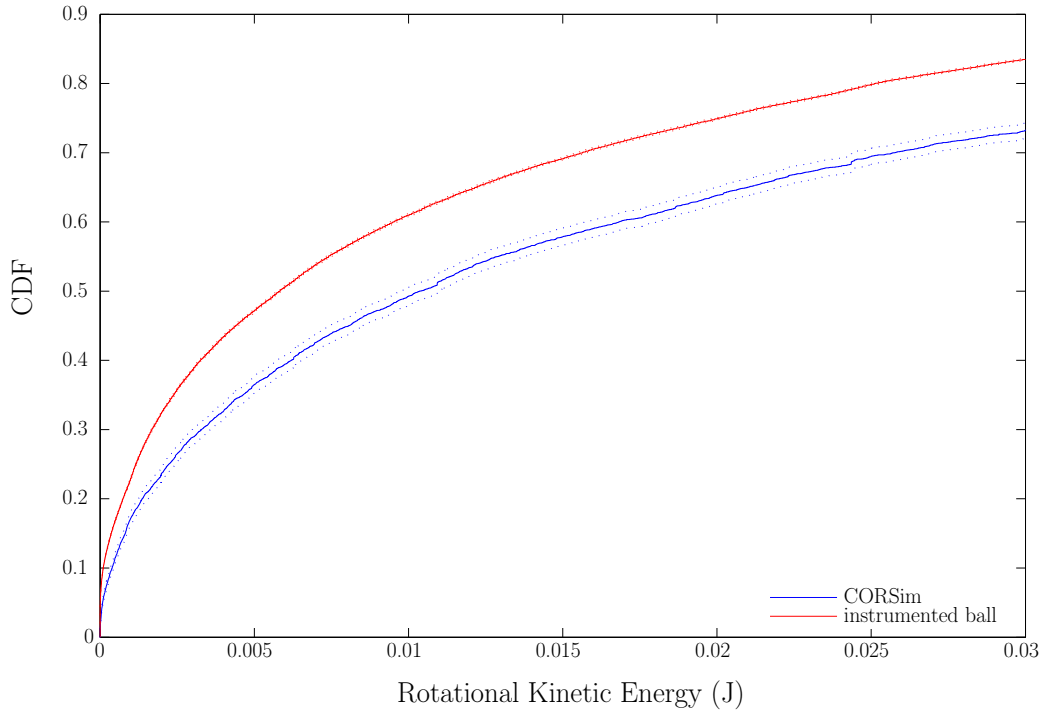


Figure 4–20: The cumulative distribution of the rotational kinetic energy

Table 4–7: *In-Situ* energy and power: mean, standard deviation and confidence limits

	E_p	E_k	E_r
Mean (J)	2.3715	0.1510	0.0165
Mean Confidence Limit (95%) (J)	(2.3103, 2.4326)	(0.1427, 0.1593)	(0.0158, 0.0183)
Standard Deviation (J)	1.5322	0.2075	0.0157
Standard Deviation Confidence Limit (95%) (J)	(1.4901, 1.5766)	(0.2018, 0.2135)	(0.0152, 0.0161)

Mean Specific Power, p_M (W/kg)	3.365
Mean Confidence Limit (95%) (W/kg)	(3.217, 3.512)
Standard Deviation of the Specific Power (W/kg)	4.099
Standard Deviation Confidence Limit (95%) (W/kg)	(3.997, 4.206)

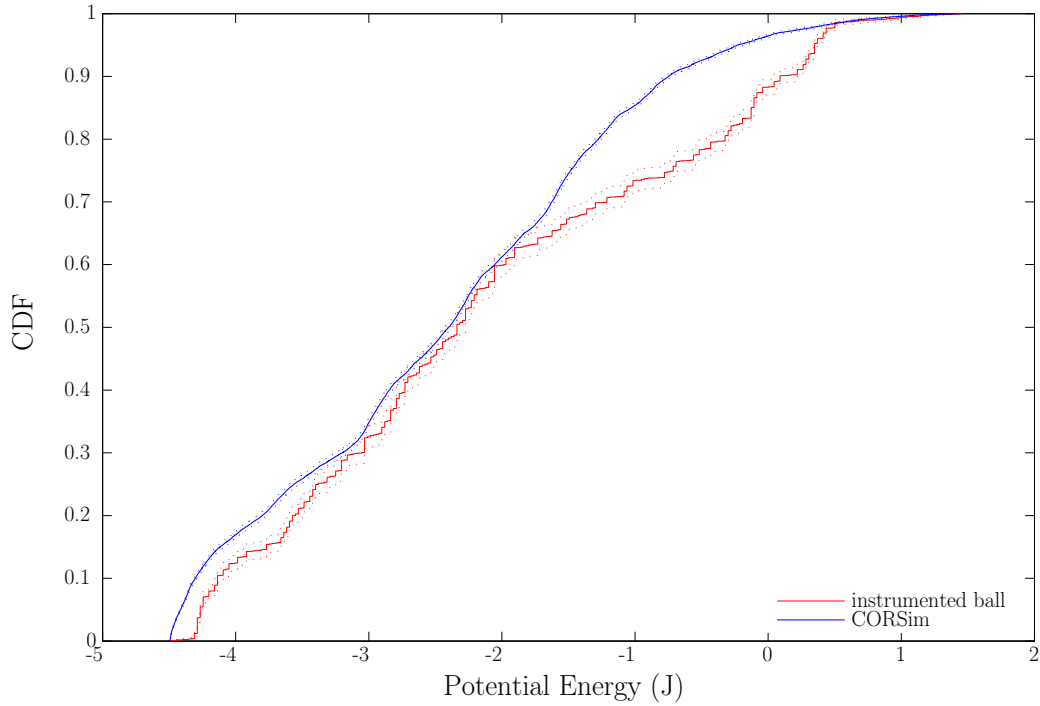


Figure 4-21: The cumulative distribution of the potential energy

Table 4-8: *In-Silico* (initial) energy and power: mean, standard deviation and confidence limits

	E_p	E_k	E_r
Mean (J)	2.1173	0.1461	0.0201
Mean Confidence Limit (95%) (J)	(2.0239 , 2.2107)	(0.13357, 0.15863)	(0.019052, 0.021148)
Standard Deviation (J)	1.3891	0.1864	0.0156
Standard Deviation Confidence Limit (95%) (J)	(1.3257, 1.4578)	(0.1779, 0.19562)	(0.014889, 0.016372)

Mean Specific Power, p_M (W/kg)	3.104
Mean Confidence Limit (95%) (W/kg)	(2.7928,3.4152)
Standard Deviation of the Specific Power (W/kg)	4.631
Standard Deviation Confidence Limit (95%) (W/kg)	(4.4198,4.8601)

Table 4–9: Range of the simulation parameters

Friction coefficient	0.1 ... 0.5
Normal viscous damping ratio	0.1 ... 0.6
Tangential viscous damping ratio	0.1 ... 0.6
Normal stiffness (N/m)	5000 ... 25000
Tangential stiffness (N/m)	5000 ... 25000

both from the experimental results and the simulation. In addition, the confidence limit can be determined for each of the moments. The value of the moments will lie, 95% of the time, within the range defined by the confidence limits. The confidence limit is a reflection of the limitations of sampled data; sampled data only give an *estimate* of the moments, with error.

Finally, each of the *in-silico* moments (the measurands) is compared with its *in-situ* equivalent. These results are presented in Figures 4–23, 4–24 and 4–25. In Figure 4–23, the mean values, and their confidence limits, of the experimental energies are plotted over the mean values, and confidence limits, of the simulated energies. Similarly for Figures 4–24 and 4–25, where the standard deviations and specific power results are plotted, respectively. If the confidence ranges overlap for *all* moments, the simulation is valid—it is in agreement with the experimental results, within error. If this is not the case, the simulation is rejected. From the results, it is seen that a simulation, where the moments match the experimental results, exists. As shown in Figure 4–22, as the number of measurands used increases, the number of simulations capable of reproducing the measurands decreases. With a set of eight measurands, only one solution is found, with model parameters given in Table 4–10. The measurands of this solution are listed in Table 4–11. When these

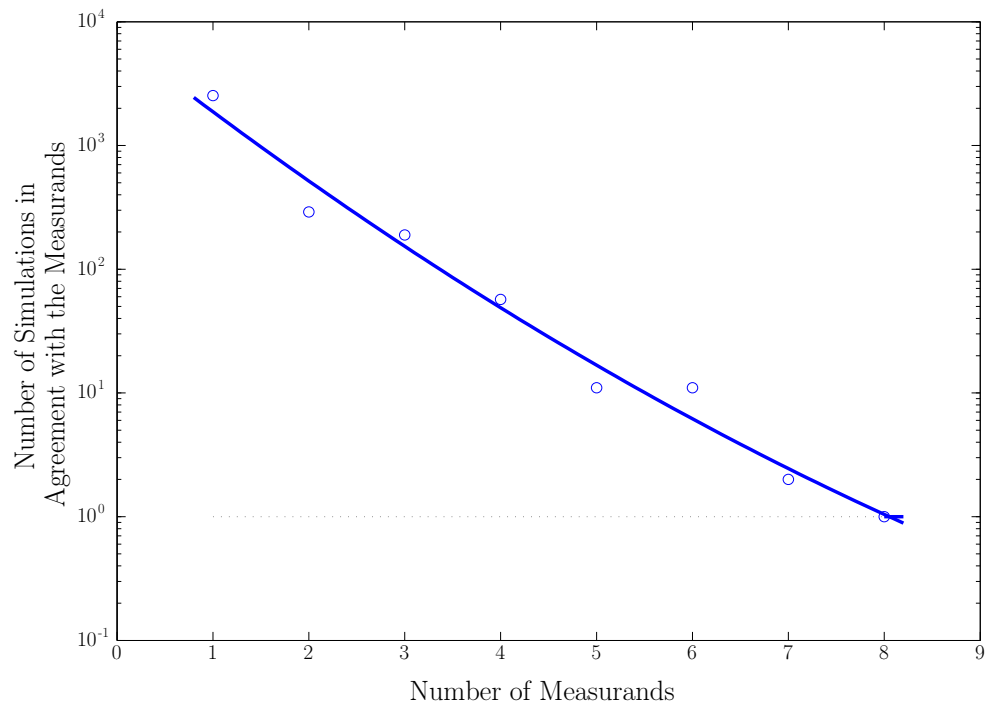


Figure 4-22: Number of valid simulations for a given number of measurands

results are compared with the experimental results (Table 4–7), it is noted that, within error (the confidence limits), there is agreement, in contrast with the initial simulation (Table 4–8). The quality of this best-fit solution is weaker than desired, as illustrated by Figures 4–26, 4–27 and 4–28. There is improved agreement with the translational kinetic energy, as demonstrated in Figure 4–27, as is the case for the potential energy (Figure 4–28). When compared to the initial simulation, the best-fit simulated potential energy distribution is an improvement, but some differences remain. This difference is pronounced at higher potential energies, where the proportion of higher energies in the simulated case is lower than in the experimental case. Since the potential energy increases linearly with height, it is concluded that the simulated charge does not dwell long enough above the center-of-circulation, particularly near the shoulder. Therefore, the behavior of the charge at high positions requires more development. Finally, the rotational kinetic energy is, within error, in agreement with the experimental results. This agreement is tenuous, likely due to sampling errors. From the distribution, as plotted in Figure 4–26, it is observed that the in-silico rotational kinetic energy is higher than the experimental result—that is, the higher values of rotational kinetic energy occur at a higher proportion than is experimentally observed. When compared to a simulation at a *lower* mill speed, a better agreement with the experimental results is observed. Since the kinetic energy is in good agreement, then the velocity evolves appropriately. Therefore, the governing equation (Equation 2.29) adequately describes the dynamics, including the contact forces (ref. Table 2–4 for DEM contact models). The problem lies with the rotational equation of motion, Equation 2.30. If the charge is over-rotating, then the

Table 4–10: Best simulation parameters

Friction coefficient	0.5
Normal viscous damping ratio	0.3
Tangential viscous damping ratio	0.4
Normal stiffness (N/m)	10000
Tangential stiffness (N/m)	20000

applied torques are too high. In the case of CORSim, the torque model is

$$\mathbf{m}_t = \mathbf{R} \times \mathbf{f}_t \quad (4.1)$$

where R is the radius vector of the body (constant magnitude in this case) and \mathbf{f}_t is the tangential contact force. As stated above, inappropriate contact forces would have an effect on the velocity and, consequently, on the translational kinetic energy, which is not the case. The radius vector has a constant magnitude—it is a charge property; it is not expected to have an effect on the dynamics. Therefore, it is concluded that the contact model is appropriate, as it generates translational kinetic energy distributions in agreement, within error, with the experimental results. Furthermore, from the rotational kinetic energy distributions, the contact model induces rotation rates far greater than what is observed in the laboratory. Thus, it is concluded that while the force contact model is adequate, the torque contact model is not.

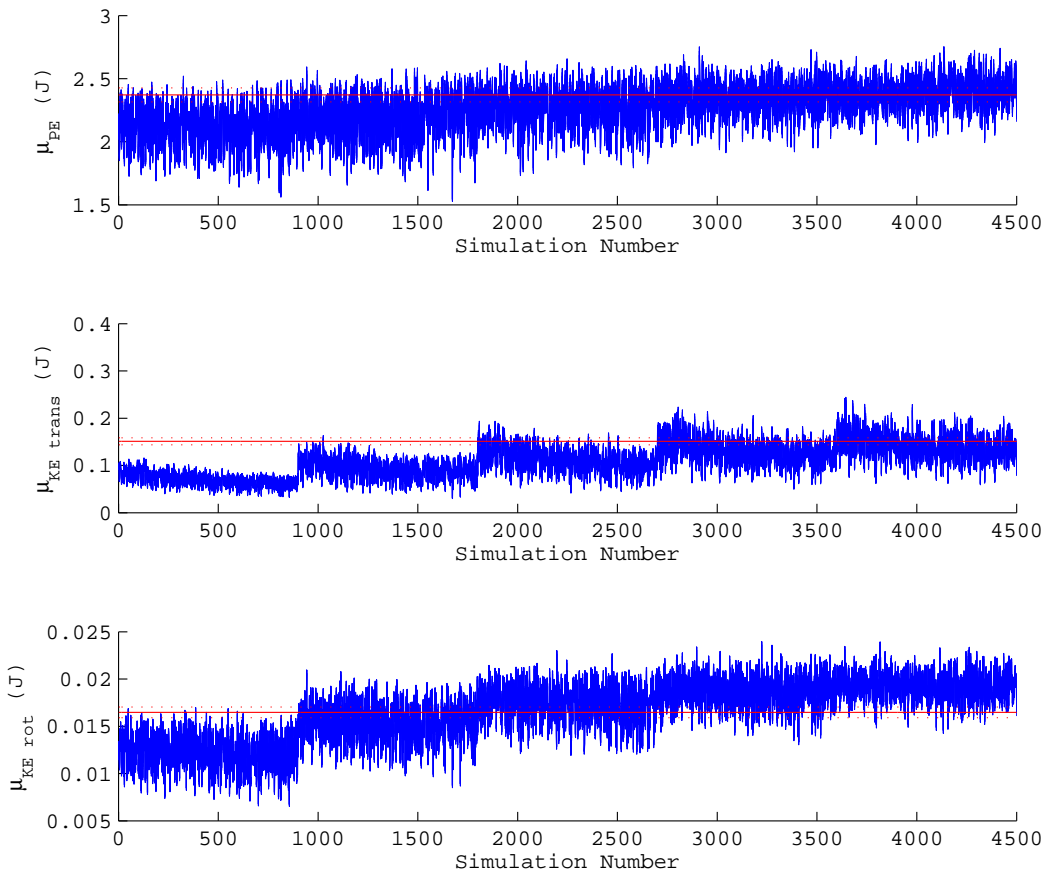


Figure 4-23: The simulated (blue) mean potential and kinetic (translational and rotational) energies compared to the experimental (red) results

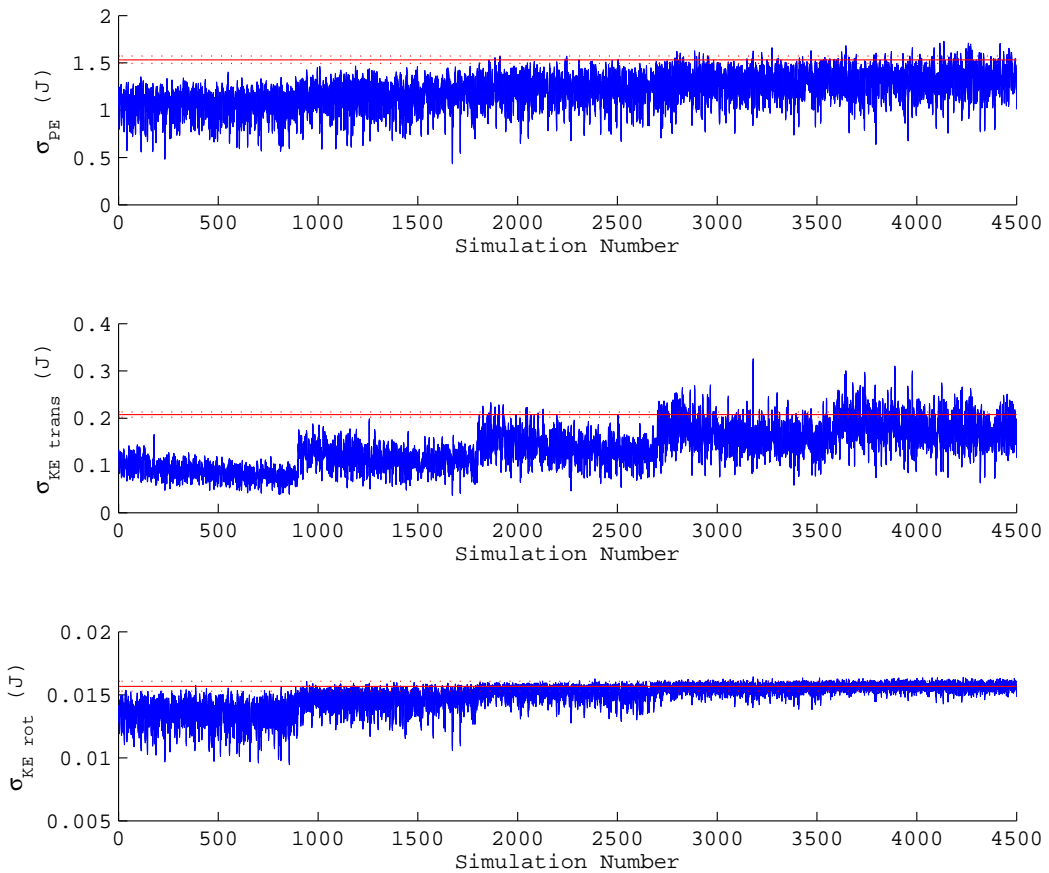


Figure 4–24: The simulated (blue) potential and kinetic (translational and rotational) energy standard deviations compared to the experimental results (red)

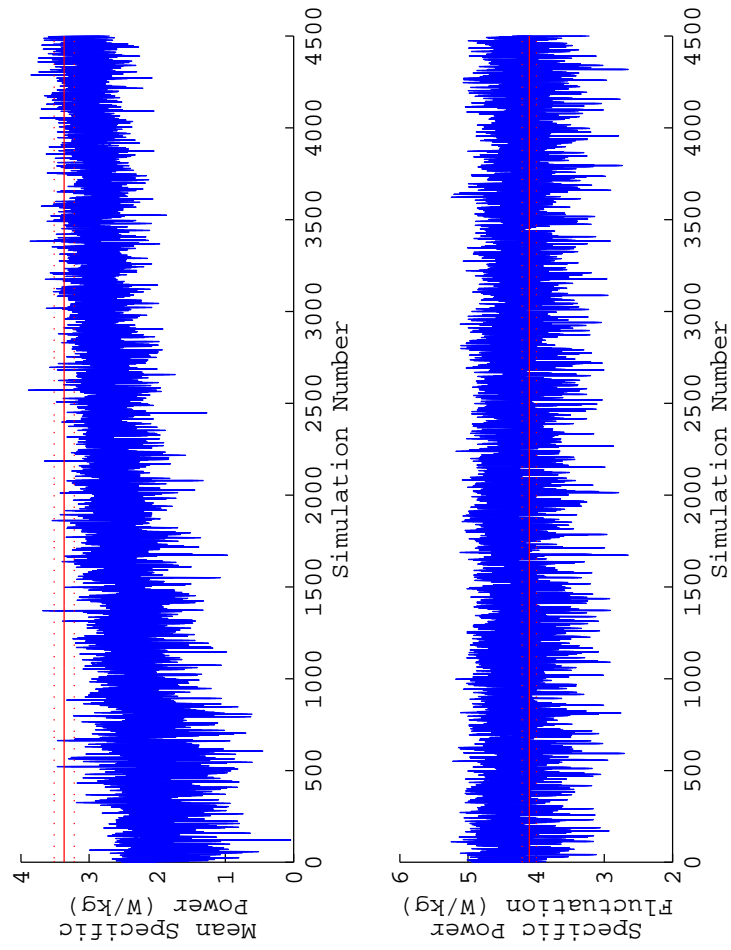


Figure 4–25: The mean and standard deviation (fluctuation) of the simulated (blue) specific power compared to the measured specific power (red)

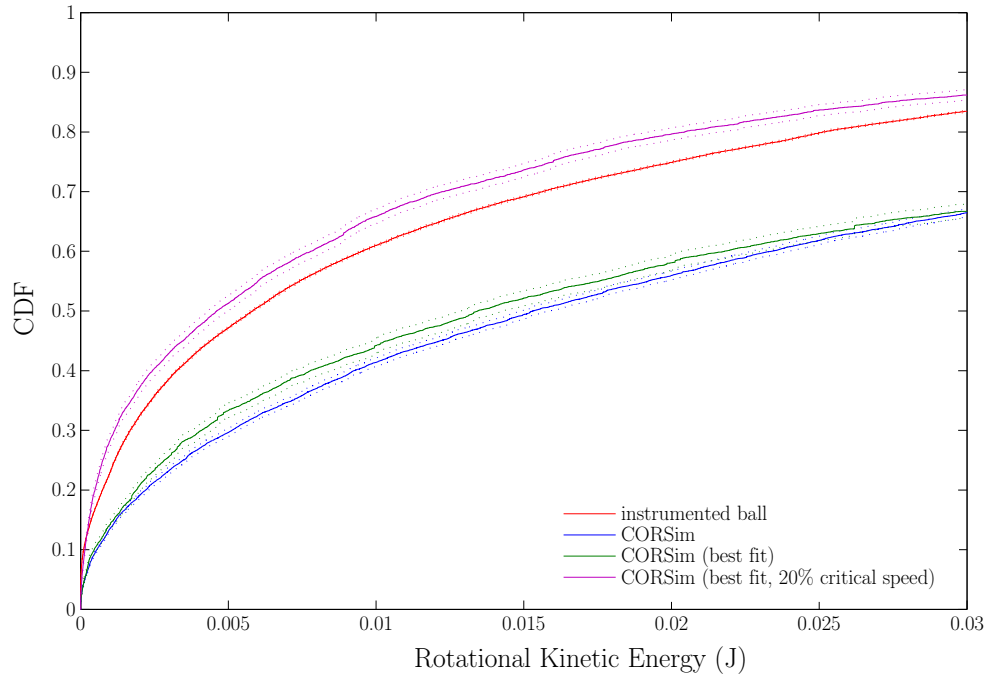


Figure 4–26: Cumulative distribution of the rotational kinetic energy with the COR-Sim best fit

Table 4–11: *In-Silico* (best fit) energy and power: mean, standard deviation and confidence limits

	E_p	E_k	E_r
Mean (J)	2.5202	0.1586	0.0201
Mean Confidence Limit (95%) (J)	(2.4236, 2.6168)	(0.14392, 0.17328)	(0.01827, 0.02193)
Standard Deviation (J)	1.4373	0.2185	0.0158
Standard Deviation Confidence Limit (95%) (J)	(1.3718, 1.5084)	(0.20854, 0.22931)	(0.015079, 0.016582)

Mean Specific Power, p_M (W/kg)	3.172
Mean Confidence Limit (95%) (W/kg)	(2.8805, 3.4635)
Standard Deviation of the Specific Power (W/kg)	4.3367
Standard Deviation Confidence Limit (95%) (W/kg)	(4.1389, 4.5513)

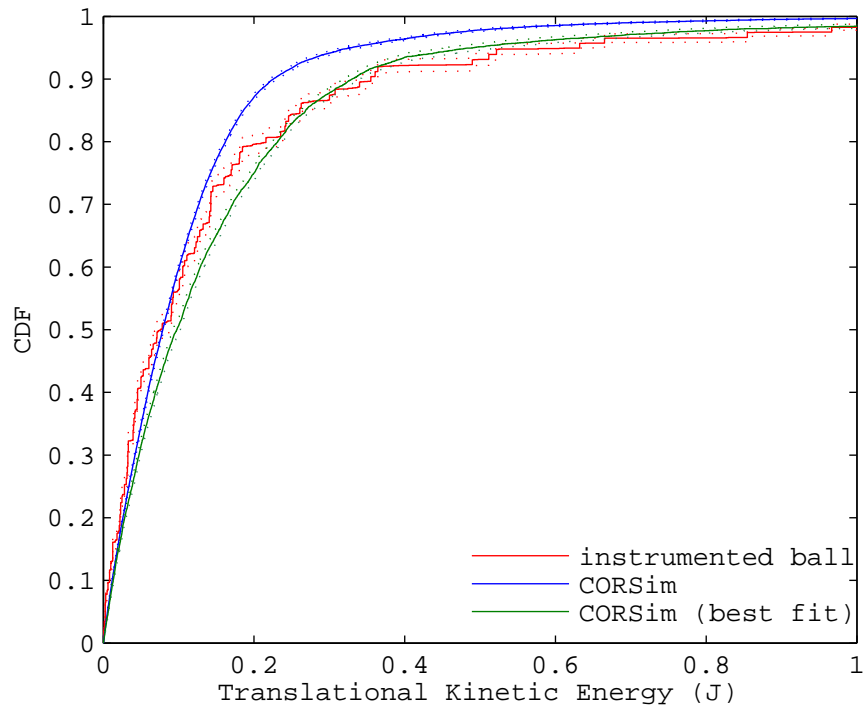


Figure 4-27: Cumulative distribution of the translational kinetic energy with the CORSim best fit

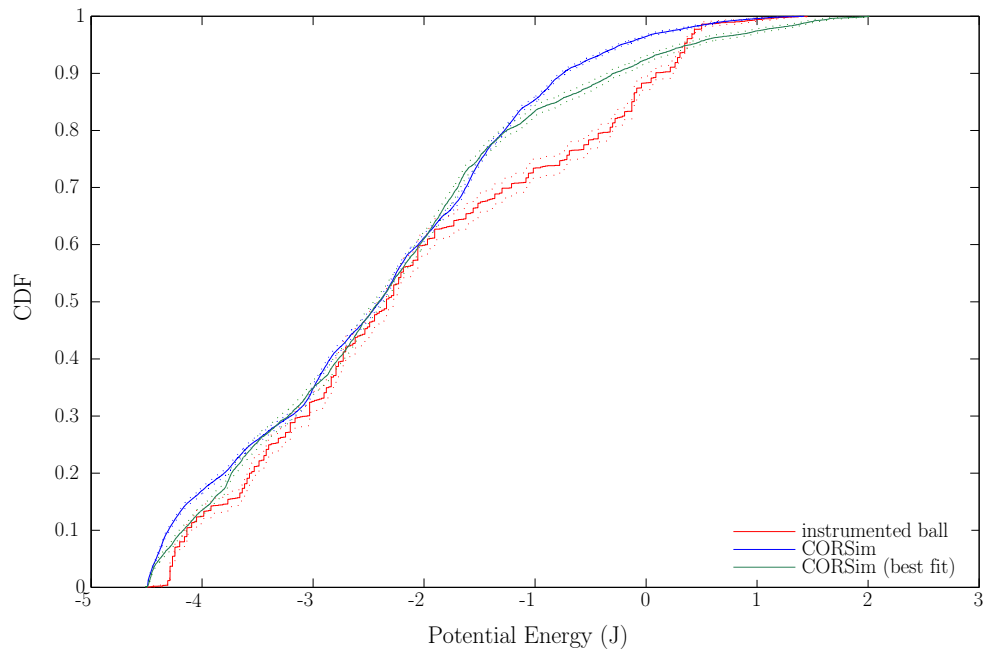


Figure 4–28: Cumulative distribution of the potential energy with the CORSim best fit

4.3 Summary

The instrumented ball is able to operate within an operating mill, and in the process, measure the rotation rates (3-axis), the acceleration (3-axis) and the temperature. For the first time, the instrumented ball permits the measurement of rotation rates of an element of the charge. Furthermore, the instrumented ball is able to produce repeatable results, for identically configured mills, as illustrated in Figure 4–5. The instrumented ball and the camera system allow for the determination of energy distributions, an important variation of past analyses of a tumbling mill. Based on the plots and moments of these distributions, it is possible to compare the *in-silico* and *in-situ* results. Though the distribution curves appear to be similar in nature, significant differences are observed when the initial simulation is compared with the experimental results (Figures 4–19, 4–20 and 4–21). Unlike the McBride *et al.* analysis [MGPC04], the comparison is not between spatial (area) distributions, but between moments—scalars—simplifying the evaluation. A similar analysis shows that both the experimental and simulated results are steady state, supporting a number of assumptions. Based on the comparison of moments (measurands), it is noted that the initial configuration of the simulation is not in agreement with the experimental results. Using the methodology outlined in Section 3.5, the moments are used to identify the DEMs in agreement, within error, with the experimental results. The experimental results are used to tune the DEM. One simulation, out of 4500, is able to match all eight measurands. Therefore, through the measurands obtained with the use of the instrumented ball and the camera system, it is possible to identify the simulation (and its parameters) that best reflects the operation of the mill. Here,

this agreement is found to be marginal. Two fronts are identified as requiring some improvements. Firstly, the instrumented ball does not dwell long enough above the center-of-circulation, particularly near the shoulder, as shown by the distribution of the potential energy (Figure 4–21). Secondly, the differences in the rotational kinetic energy, contrasted with the good agreement between the translational kinetic energy distributions suggest the need for a reduction in the applied torque, without changing the force contact model.

In this chapter, the objectives of this study are met. It is demonstrated that an instrumented ball can be designed and built, with improved electronics, able to measure rotation rates. As part of a sensor suite, a set of measurements are obtained, allowing the determination of the translational kinetic energy, the rotational kinetic energy and the potential energy. From the measurements, distributions are found. Also, the distributions are not associated with the cross-section of the mill, in contrast to, and different from the past work. From these distributions, it is possible to generate a set of measurands (moments), with which the experimental and simulation results can be compared. Though the experimental results are consistent with the DEM results, differences are observed. By varying the DEM parameters, the simulation that best represents the mill is found, tuning the DEM to enhance its accuracy. Finally, from the remaining differences, areas in need of improvement are identified.

In the next chapter, the use of the distribution-based description of the mill is expanded. In addition, a measurand-based metric, for the evaluation of the accuracy of DEMs, is introduced.

CHAPTER 5

Discussion

The functionality and usefulness of the instrumented ball and the camera system, in the understanding of mill dynamics, in parallel with their interaction with DEM models, were shown in the last chapter. Here, the results are used to expand the usefulness of the distribution-based description of the mill dynamics. Moreover, a countable set of measurands is used to constrain the DEM, forcing the elimination of unphysical simulations. This set of measurands is developed into an accuracy metric for DEMs.

5.1 Instrumentation, Measurands and Model Order

The instrumented ball demonstrates the ability to operate within a working mill. In doing so, it is possible to measure the acceleration, the rotation rate and the temperature within the mill [MLRC06a]. Furthermore, the platform is plastic. Most components can be upgraded if need be and, expansion is easily achieved since a number of analog and digital communication channels are presently free. Therefore, more measurands can be added either through the incorporation of another sensor system or by expanding the number of instruments within the instrumented ball. The advantage of the second option is that the instrumented ball evolves with the charge, allowing for internal measurements along the trajectory of the instrumented ball.

By using a *selected* set of sensors, a set of measurands, M , is constructed. Since the measurands are finite, they are countable, as expressed below.

$$\forall M, \exists N \in \mathbb{N} \text{ s.t. } f_c: M \mapsto N \quad (5.1)$$

Furthermore, by using the methodology outlined in Section 3.5, a number of valid DEM solutions, n_s for a particular measurement set, M , can be found.

$$\forall M, \exists n_s \in \mathbb{N} \text{ s.t. } f_v: M \mapsto n_s \quad (5.2)$$

Both these expressions allow for a model order to be defined:

$$\mathcal{O} \equiv \sup[f_c(M)H(f_v(M) - 1)] \quad \forall M \quad (5.3)$$

where H is the right-continuous Heaviside step function. The model order, \mathcal{O} , is a measure of how many measurands a given model can simultaneously satisfy. The larger the model order, the more accurate the model, since it is able to simultaneously agree with more measurements or quantities derived thereof. The measurements used in the determination of the model order must be based on quantities that are characteristics of the system. A single trajectory is not a characteristic of the system since it is not invariant with respect to reproducibility, whereas energy distributions, the toe position, the shoulder position, and the COC position are.

In the case of CORSim, the model used to simulate the laboratory mill, the number of solutions capable of reproducing the measurands rapidly decreases as the number of measurands increases (Figure 5–1). With only one measurand, several thousand simulations are able to reproduce the experimental results. With four

measurands, the number of valid simulation falls to several hundred. For a measurand set with eight elements, only one simulation is able to reproduce the measurands. Therefore, the order \mathcal{O} of the CORSim model is 8. The CORSim model order may be 9 (or higher) but no additional measurand, which gives at least one valid solution, has been identified. Until one is identified, the CORSim model order remains at 8. Possible candidate measurands exist. For instance, an acoustic analysis can give both measured and simulated results [HMR⁺on, MZP⁺06]. As shown in Figures 5–2 and 5–3, the Fourier transforms of the acoustic signal amplitude, both measured in the lab and calculated from the DEM model shell forces, show a number of interesting features that can become measurands. The resonant peaks, present in the *in-situ* and *in-silico* results, are one example. From the acoustic figures, two peaks are observed in both spectra, one at $f/f_{mill} = 1$ and another at $f/f_{mill} = 2$. Quantities such as the relative strength of the two resonances can generate measurands. Also present, but not as visible, is a peak due to the lifters at $f/f_{mill} = 12$. The ratio between the amplitude at this frequency and the peak at the mill frequency, $f/f_{mill} = 1$, may be another measurand. Additionally, during the experiment, the temperature of the instrumented ball is recorded. On examination of the data, it is noted that the temperature increases. Therefore, either the temperature difference or the rate of temperature increase may be a third measurand. Incorporating temperature within this framework would require adding thermal modeling to DEMs [DDT07, FHO07], thereby creating a more detailed model of the mill.

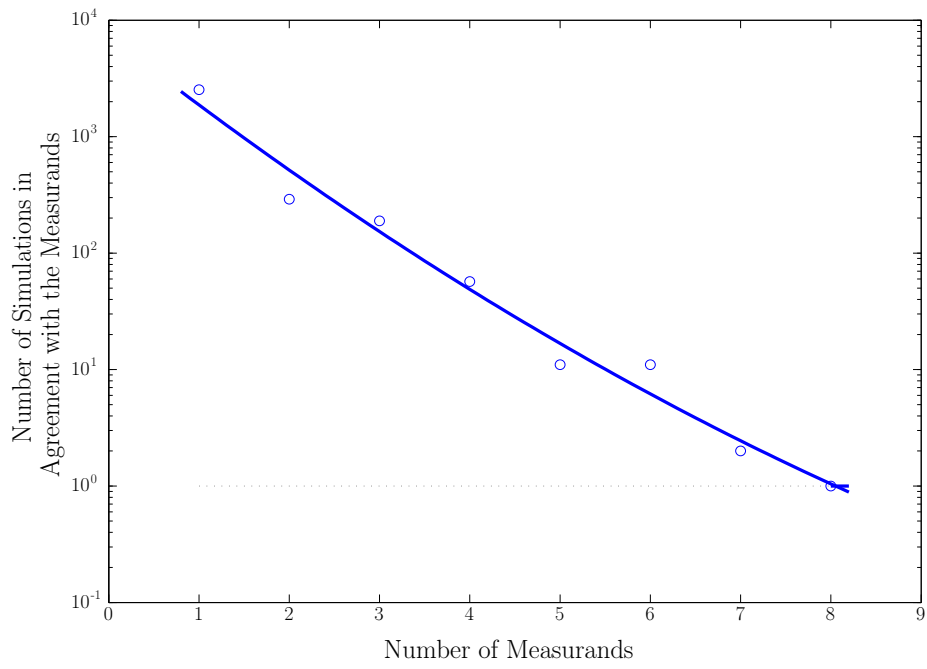


Figure 5–1: Number of valid simulations for a given number of measurands

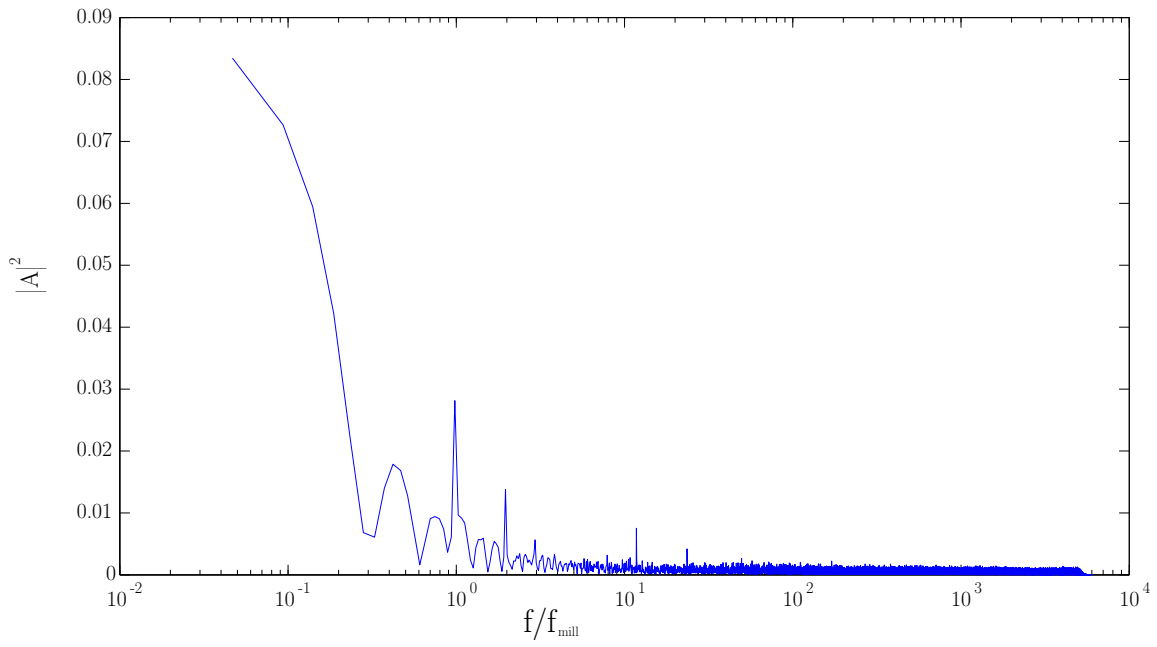


Figure 5-2: Fourier transform of the measured acoustic amplitude [HMR⁺on]. The units of the amplitude, $|A|$ are arbitrary. The value of f_{mill} is 0.4 Hz.

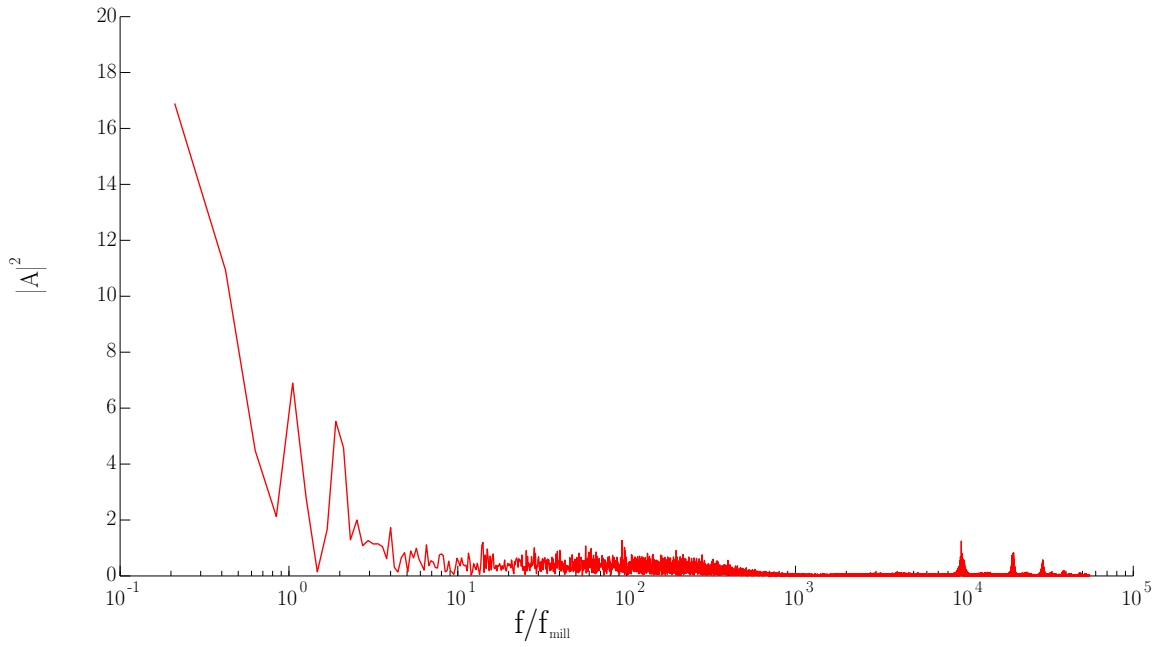


Figure 5–3: Fourier transform of the simulated acoustic amplitude [HMR⁺on]. The units of the amplitude, $|A|$ are arbitrary. The value of f_{mill} is 0.4 Hz.

5.2 Entropy and Energy Fluctuations

In statistical mechanics, the entropy is a measure of the accessible states of the system. The entropy can be interpreted as the quantity of disorder in a system. For discrete systems, the entropy is [Hua87, PM05]

$$S_N/k = - \sum_{i=1}^N P_i \ln(P_i) \quad (5.4)$$

where k is a positive constant, P_i is the probability of being in the state i , and N is the total number of states. For a continuous system, with a density of states $p(x)$, the entropy is generalized by [MNB08]

$$S_c/k = - \int_{\Omega} p(x) \ln(p(x)) dx \quad (5.5)$$

where $\Omega = \{x|p(x) > 0\}$ is the support set of x . The energy distribution of the instrumented ball, $P(E)$, can be interpreted as being the probability of finding the ball in a state with an energy between the values E and $E + \Delta E$. This gives rise to the possibility of estimating the entropy of an element of the charge by applying either Equation 5.4 to the energy distribution, or Equation 5.5 to the energy distribution density. Since the *in-situ* and *in-silico* energies are sampled, the discrete entropy is used (Equation 5.4). To obtain an estimate of the continuous entropy (Equation 5.5), a series of finer bins are used to calculate the discrete entropy.

$$S_c/k \cong - \lim_{N \rightarrow \infty} S_N/k \quad (5.6)$$

A quadratic function, fitting the sequence of S_N/k is found, and plotted, along with the entropy sequence, in Figure 5–4. From the quadratic equation, the maximum

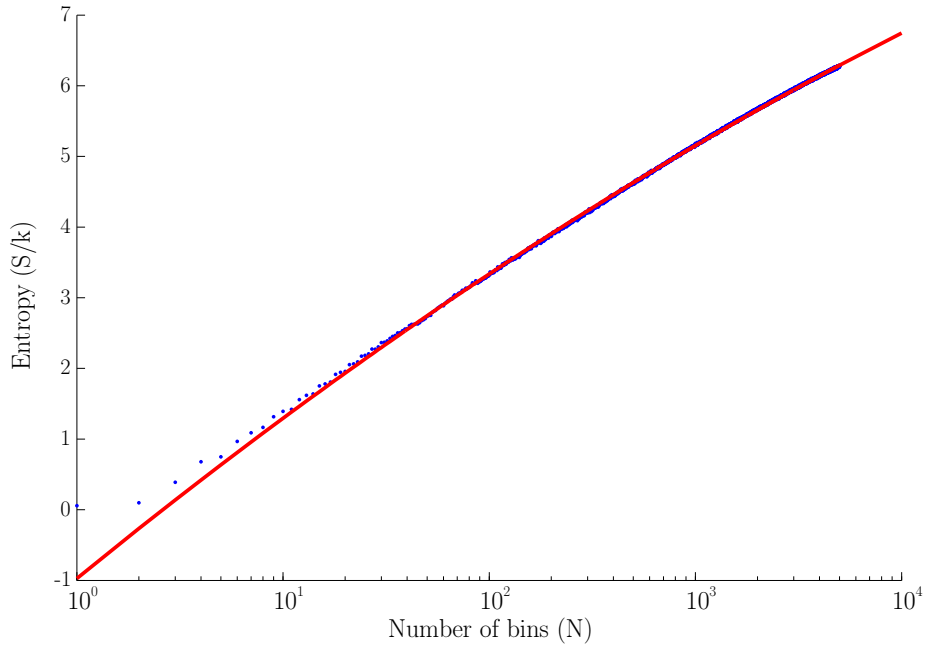


Figure 5-4: entropy estimate as the probability bin number is increased

of the entropy is determined and is used as an estimate for S_c/k . This maximal estimate is extrapolated from the data and will, at present, have a significant error. Nevertheless, it is useful in the discussion of the mill behavior. To reduce the error, a larger data set must be collected, allowing for larger values of N . The entropy and energy fluctuations are two quantities that may potentially allow a more detailed understanding of the internal dynamics of the mill. As support for some of this analysis, the concept of phase transition is presented. A phase transition occurs when there is a singularity or a discontinuity in the free energy or one of its derivatives, such as the heat capacity [Yeo92, Hua87]. Figure 5-5 is an example of a phase transition. As the temperature of argon, T , approaches the critical temperature, T_c , the specific heat, C_v/k , diverges; argon exhibits critical behavior as it approaches the

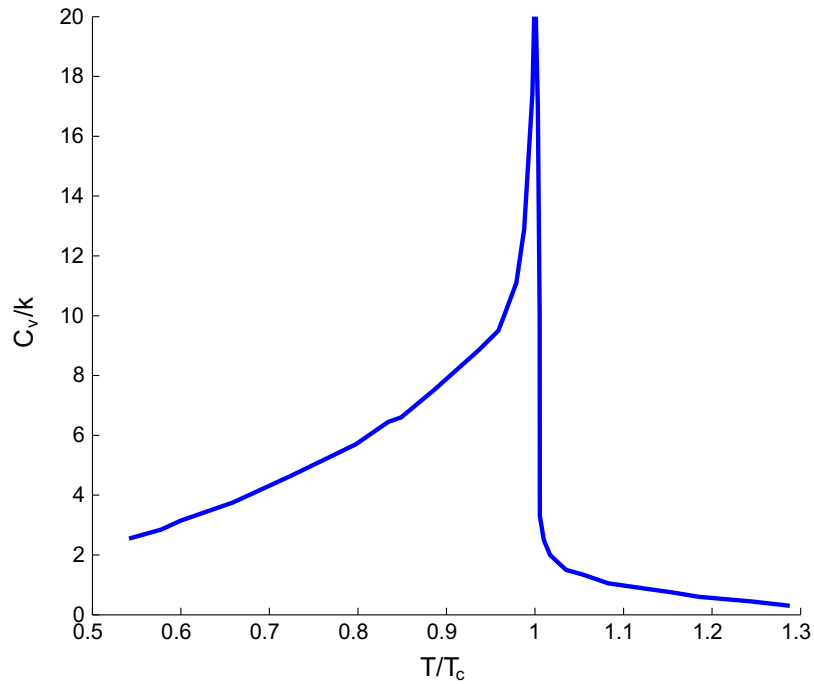


Figure 5–5: An example of a phase transition—specific heat at constant volume of Argon [Yeo92]

critical temperature. Below the critical temperature, one phase of argon is present; above the critical temperature, another phase of argon exists.

Using the CORSim simulator, with the parameters set to the values identified during the process to find agreement between *in-silico* and *in-situ* results (Section 4.2.7), a number of simulations at different mill speeds are compiled. From these simulations, the entropy (S/k), the mean energy (μ_E), which is the mean of the sum of the potential and kinetic energy, and the variance of the energy (σ_E) are calculated. The reason the variance is plotted lies with the relationship, in certain simple thermodynamic system, between energy fluctuations and the heat capacity

Table 5–1: The critical speeds of the laboratory mill

Critical Speed Expression	value (% of $N_{c,Davis}$)
$N_{c,Davis}$	100
$N_{c,Rose}$	104
$N_{c,Watanabe}$	117
$N_{c,Hooke}$	155

[MRdR+09],

$$C_v = \frac{\partial E}{\partial T} = \frac{\sigma_E^2}{k_B T^2} \quad (5.7)$$

where E is the internal energy, T is the temperature, σ_E is the variance of the energy distribution, and k_B is the Boltzmann constant. This simple relation is likely not valid for the case of the mill charge, but underlines a relationship between fluctuations and the heat capacity. Since the heat capacity can have critical behavior, as illustrated in Figure 5–5, the energy fluctuations may also display critical behavior. The results of this analysis are presented in Figure 5–6. Though the number of particles is low in this configuration (two-dimensional), several interesting features are observed in Figure 5–6. As the speed of the mill increases past the critical speed, both the entropy, the mean energy and the variance of the energy exhibit a behavior similar to a phase transition, as illustrated in Figure 5–5. A transition speed, Ω_T , about which both the entropy, the mean energy and the variance of the energy exhibit critical behavior, can be identified. For the configuration of the laboratory mill, as described in Chapter 3, the transition speed, Ω_T , occurs at approximately 150 % critical speed. For the sake of comparison, a table of critical speeds (Table 5–1), as defined in Section 1.3.6, is compiled using the laboratory mill parameters. The onset of centrifuging of the charge, beginning with the smallest sized particles,

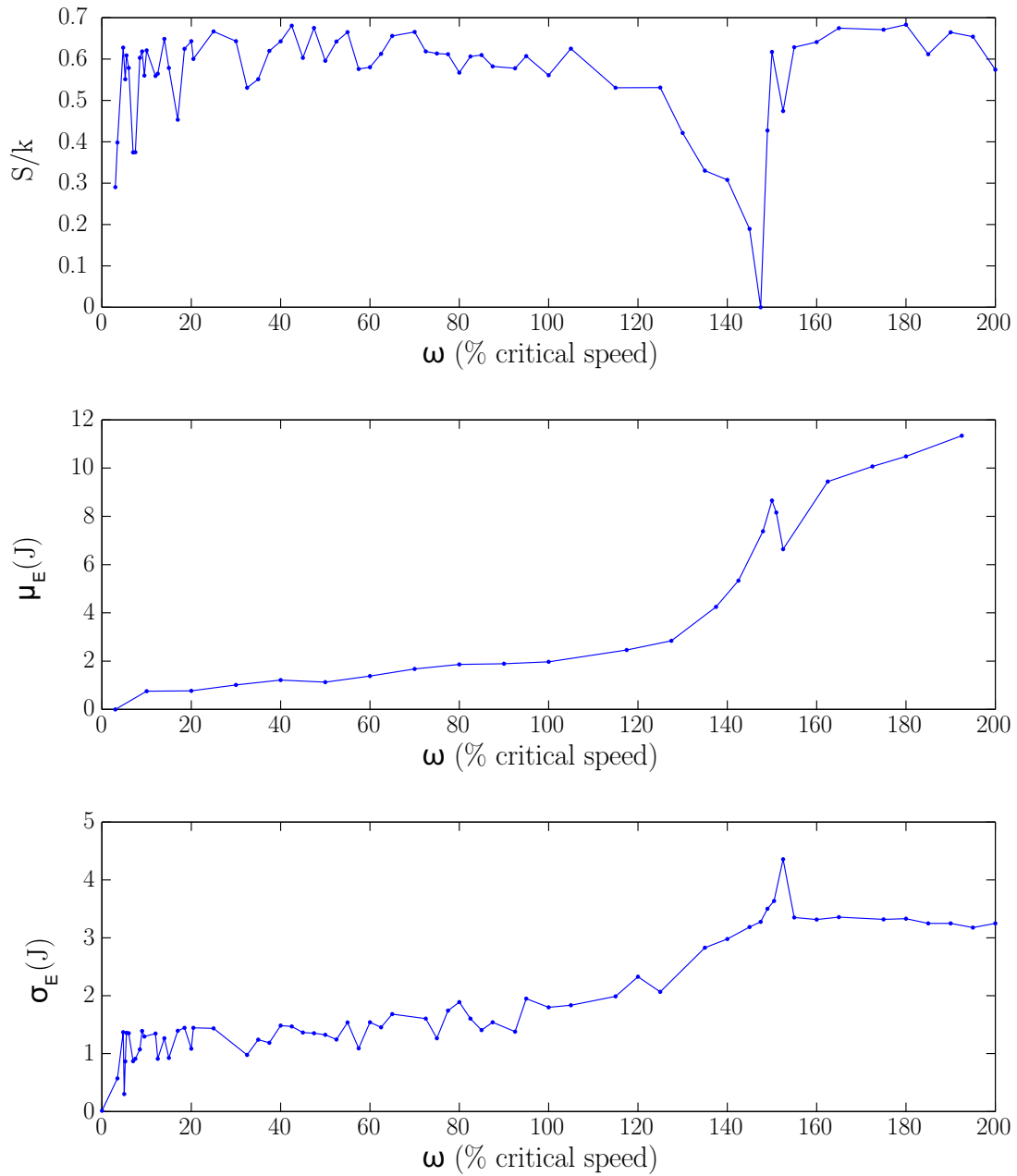


Figure 5–6: Simulation entropy, mean energy and total energy fluctuations as mill speed is increased

occurs at the critical speed (Equation 1.6). Since the particle size of the mill is uniform and well defined (Tables 3–1 and 3–7), the speed at which the actual centrifugal forces begin to dominate is the Rose critical speed, $N_{c,Rose}$ (Equation 1.2). Here, the Rose critical speed is approximately 104 % critical. At this speed, any element of the charge, with a diameter less than 11.5 *cm* and in contact with the wall, is centrifuged to the mill shell. However, this does not prevent sliding along the walls of the shell. Watanabe defines a critical speed at which all of the charge centrifuges (Equation 1.3). For the laboratory mill, this value is approximately 117 % critical. Finally, Hooke defines a critical speed at which the gravitational forces are overcome by centrifugal friction effect (Equation 1.5), even preventing the sliding motion along the shell. Here, the Hooke critical speed has a value of 155 % critical. Based on the behavior of the entropy, the mean energy and the energy fluctuation, a new definition of the critical speed is introduced:

The critical speed of a mill is the speed at which the entropy, the mean energy or the standard deviation of the energy exhibit critical behavior.

Unlike other definitions, which rely on geometric and dynamic analyses of the charge, this new definition is based on distributions and moments (see Section 1.3.6). It is argued that the critical point observed in Figure 5–6 represents a transition point. Moreover, this transition point is possibly the Hooke critical speed. The Hooke speed defines a mill rotation rate at which the charge centrifuges to the extent that the induced frictional force are large enough to prevent any motion. The charge is locked. This configuration may be described as a jammed state. A jammed state occurs when the dynamics slow down dramatically to the point where the system

can no longer relax and becomes rigid [Bir07]. States analogous to jammed states occur in colloidal solutions, glasses and similar amorphous solids. Consequently, a better understanding of mill dynamics may be possible by adopting and leveraging the analysis of these other granular systems [EO89], despite the difficulty of justifying some of this existing formalism from first principles[Her93].

At present, there are no reasons why other critical points would not exist. For example, Rolf and Vongluekiet observe distinct changes in the impact energy distributions as the mill speed increases (see Section 2.3). Below speed of 100 % critical, a number of maxima are found in the distributions. Above the critical speed, the peaks shift to levels below the instrument measurement range (Figure 2–8). This suggests the presence of a second critical point, at either the Davis critical speed or the Rose critical speed. These other critical points may be identified by adopting other techniques from the field of thermal and statistical physics, such as the correlation function [Yeo92]. Eventually, a description of the mill, analogous to a phase diagram, could be developed once more critical points are found. This description of the mill could simplify its operation by synthesizing the states of the mill.

Additionally, through the development of a free energy and an effective temperature, the thermodynamics-inspired description of the mill could be broadened, as illustrated by Equation 5.8, a standard thermodynamic equation [Hua87],

$$A = U - TS \tag{5.8}$$

where A is the free energy, U is the internal energy, T is the effective temperature, and S is the entropy. A possible method to find the effective temperature is the use

of the fluctuation theorem, as described by Equation 5.9 [FM04].

$$\ln \left(\frac{\Pi(p_\tau)}{\Pi(-p_\tau)} \right) = \frac{p_\tau \tau \bar{P}}{T_{eff}} \quad (5.9)$$

where the ratio of probabilities to find both positive and negative power fluctuations, $\Pi(p_\tau)$ and $\Pi(-p_\tau)$ respectively, is related to the dimensionless power fluctuation, p_τ , over a time period, τ , at an average power, \bar{P} , and at an effective temperature, T_{eff} . Using the fluctuation theorem, Feitosa and Menon are able to find an effective temperature for a collection of inelastic beads, maintained in a fluidized steady state by external mechanical driving mechanism. A similar analysis could apply to tumbling mills.

Finally, it is noted that the *in-silico* mean energy, plotted in Figure 5–6 (middle), varies smoothly with the speed of the mill, as does the *in-situ* rotational kinetic energy (Figure 4–6).

5.3 Distributions

The nature of the distribution of particles gives some insight into the dynamics of the particles. From quantum mechanics, an example is the fundamental particles: bosons and fermions. Bosons, such as photons, are the class of particles having the property of being indistinguishable, and having *no restriction* in the number of particles in a given state. On the other hand, fermions, such as electrons, are indistinguishable, but *limit the number of particles in any given state to two*. These properties of these two types of particles gives rise to very different behaviors and dynamics [SMM89]. These differences are reflected in their statistics. For instance, the distribution function for photons in thermal equilibrium at temperature, T , is

described by the Bose-Einstein distribution. The probability of the bosons being in the energy state, E , is

$$f_{BE} = \frac{1}{B e^{E/kT} - 1} \quad (5.10)$$

where B is an appropriate constant. Free electrons follow a different distribution. They follow Fermi-Dirac statistics, where the probability of the fermions being in an energy state, E , is given by

$$f_{FD} = \frac{1}{e^{(E-E_F)/kT} + 1} \quad (5.11)$$

where E_F is the Fermi energy. At $T=0$, all states above the E_F level are empty, all states below are filled. These two classes of particles point to the strong relationship between the nature of the dynamics and the statistics of the particles. Clearly the mill is not a quantum system, but the previous example illustrates how the identification of the distribution could provide some insight into the behavior of the charge. For instance, if the total energy follows a normal distribution, the entropy, as defined by Equation 5.5, becomes

$$S/k = \frac{1}{2} \ln(2\pi e\sigma^2) \quad (5.12)$$

5.4 Moments

Using the methodology outlined in Chapter 2, some differences will remain due to the use of only the first two moments. Although three different distributions may have the same mean and standard deviation, as illustrated in Figure 5–7, they differ since the other moments are not the same. The condition for agreement (Equation 3.24) requires *all* the moments to agree. In practice, this can be relaxed to a condition

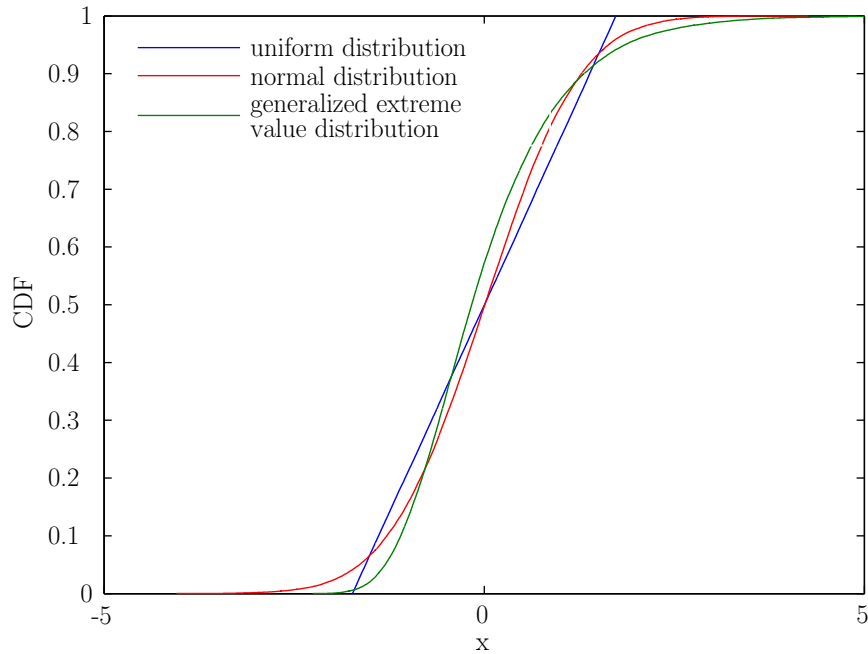


Figure 5-7: Three cumulative distribution with the same mean, $E(x) = 0$, and standard deviation, $E(x^2) = 1$

where the number of moments are chosen such that they are sufficient to have *in-situ* and *in-silico* agreement within tolerable error.

In this case, the distributions do indicate the necessity of higher order moments. The skewness, μ_3 , a measure of the asymmetry about the mean, is defined as

$$\mu_3 = \frac{E((x - \mu)^3)}{\sigma^3} \quad (5.13)$$

where μ is the mean. If the skewness is negative, the random variable is spread out more for values less than the mean than for values greater than the mean; inversely for a positive skewness. For the laboratory mill, some degree of asymmetry exists since the standard deviation of the kinetic energy is larger than the mean value. Without

Table 5–2: The skewness of the *in-situ* rotational kinetic energy, translational kinetic energy and potential energy

Energy Term	Skewness
Rotational kinetic energy	0.997
Translational kinetic energy	10.637
Potential energy	0.3048

any asymmetry or skewness, the larger standard deviation implies the existence of negative energies, which is not the case for the kinetic energy. The skewness of the data collected when the mill is in its cylindrical charge configuration is found in Table 5–2. Having the simulation match the experimental skewness values, within error, is a step to be added to the methodology presented in Section 3.5.

5.5 Summary

The distribution-based description of the mill charge is extended to give some useful results. Firstly, the countable set of simulations satisfying a given and countable set (or subset) of measurands is found. Moreover, the count of valid solution falls as the set of measurands grows. This provides the opportunity to define a measure for model accuracy, the *model order*. The model order is the maximal number of measurands a simulation can satisfy simultaneously. This can be used to guide a user in the selection of DEM implementation. If more accuracy is required, a model with a higher order should be selected. Finally, the set of measurands is not limited to eight. More can be added by adding higher moments or other measurements, such as the acoustic results, to the measurand set.

The distributions of energies are also determined from the measurements. These same distributions can be generated by the simulation. Unlike the distributions over

the cross-section area, these distribution provide a quick means to evaluate the differences between the simulations and the measurements. Furthermore, the distribution description allows for the introduction of a number of concepts from thermodynamics and statistical mechanics. Though not directly applicable, the concepts are nevertheless applied to this system, similar to what is done for colloids and granular flows, where similar applicability problems are present. From the measurement and the distributions, the entropy, the mean energy and the energy fluctuation are calculated. Upon examination of the *in-silico* results, critical behavior, similar to phase transitions, is seen. The critical behavior allows for an additional definition of the critical speed of the mill. The critical speed is defined as the speed at which the entropy, the mean energy or the energy fluctuation exhibit critical behavior. The critical point identified here appears to be related to the Hooke definition of the critical speed. Additionally, this new critical point is not necessarily unique. Therefore, it may be possible to build a state diagram, similar to a phase diagram, as a description of the state of the charge. Finally, identifying the nature of the distribution may help in understanding the nature of the dynamics.

CHAPTER 6

Conclusion

Mineral processing is an important part of human technology, as witnessed by its use throughout human history. It is the principal method used to obtain many of the minerals used today. An essential aspect of mineral processing is the breakdown of the ore. This is done in cases where the valuable mineral is not readily accessible, such as when it is trapped by surrounding material. How the mineral is made accessible is by either crushing or grinding, collectively known as comminution. Machinery such as the grinding mill, are used for such tasks.

The grinding mill operates by lifting the charge and dropping it back onto itself, by virtue of the rotation of the mill, thus creating impact and grinding forces. The complex behavior of the mill, coupled with its low efficiency, drive the interest in studying grinding mills. Unfortunately, the nature of the machine makes embedding instruments within the mill, where the charge properties can be measured, difficult. With the ability to operate within the charge, instrumented balls are a class of instrumentation able to overcome this problem. Therefore, the goal is to develop a better understanding of tumbling mill dynamics through the development and use of an instrumented ball. This is accomplished by addressing the following objectives:

1. To show that an instrumented ball can be designed and built, with improved electronics;

2. To show that it is possible to obtain measurements from the mill interior, particularly measurements that are not impact forces;
3. To show that these measurements allow for a different type of analysis of the mill;
4. To show that the data are comparable to DEM simulation results;
5. To show that the data are helpful with regards to DEMs.
 - (a) The instrument measurements can be used to verify that the DEM results accurately represent the system;
 - (b) The instrument measurements can be used to tune the DEM simulations, enhancing their accuracy; and
 - (c) The instrument measurements can be used to identify aspects of the DEMs in need of improvement.

In this thesis, the objectives are met, as shown in Chapter 4. It is demonstrated that an instrumented ball can be designed and built (Objective 1), with improved electronics, able to measure rotation rates (Objective 2). With the assembly of the sensor suite (instrumented ball and camera system), a set of measurements are obtained, allowing the determination of the translational kinetic energy, the rotational kinetic energy and the potential energy. From the measurements, distributions are found and a set of measurands is generated, with which the experimental and simulation results are evaluated (Objective 3). Though the experimental results are consistent with the initial DEM results, differences are observed (Objectives 4 and 5a). After analysis, it is concluded that the differences are due to the use of an incorrect parameter set when solving the DEM. By systematically varying the DEM

parameters, 4500 simulations results are produced, each calculating the same measurands as the experimental run. Of the 4500 simulations, only one simulation that best represents the mill is found. Since its parameter set is known, this methodology tunes the DEM, enhancing its accuracy (Objective 5b). Finally, from the remaining differences, areas of improvement are identified (Objective 5c). For the CORSim model, the behavior of the charge near the shoulder requires some correction. Also, the charge rotates faster than what is observed. Without changing the contact forces, which leaves the translational kinetic energy distribution unchanged, a reduced torque model is needed to slow the rotation rate.

As an extension to the above results, the set of countable simulations satisfying a given and countable set (or subset) of measurands is found. Moreover, the valid solution count falls as the set of measurands grows. This provides the opportunity to define a measure for model accuracy, the *model order*. The model order is the maximal number of measurands a simulation can satisfy simultaneously. This can be used as a guide when selecting the implementation of the DEM model of the mill. If more accuracy is required, a higher order model should be favored. Finally, the set of measurands is not limited to eight. More measurands can be added by adding higher moments or other measurements, such as the acoustic results, to the measurand set.

As is the case for the measurands, the energy distributions can have another function. The distribution description allows for the introduction of a number of concepts from thermodynamic and statistical mechanics. Disregarding any applicability problems present, as is done in the study of granular flows, the entropy, the mean energy and the energy fluctuation are calculated. From the *in-silico* results,

critical behavior, similar to phase transitions, is seen. The speed about which the critical behavior occurs is significant, and gives an additional definition of the critical speed of the mill. This new critical speed is defined as the speed at which the entropy, the mean energy or the energy fluctuation exhibit critical behavior. The critical point identified here appears to be related to the Hooke definition of the critical speed. Additionally, this new critical point is not necessarily unique. Therefore, it may be possible to build a state diagram, similar to a phase diagram, as a description of the state of the charge.

6.1 Contribution to Knowledge

Several results are to be noted as contributions to knowledge. First, an instrumented ball, capable of measuring accelerations, rotation rates and temperature has been built. Of these measurements, the rotation rates of an element of the charge have never been measured before.

Next, the distributions of the potential energy, the translational kinetic energy and the rotational kinetic energy, and their moments, are used to evaluate the agreement between the *in-situ* and the *in-silico* mills. This permits the identification of DEMs in agreement with the measurements, within error. This method is new to comparing and tuning DEMs to the experimental results.

Furthering this work, the *model order*, a measure of a model's ability to accurately reproduce a number of measurements is defined.

Finally, the use of distributions, in the context of grinding mills, is extended with the introduction of mill entropy, mean energy and energy fluctuation. From these results, critical behavior is observed. Furthermore, a new critical speed is defined:

the critical speed is the mill speed at which critical behavior in the entropy, the mean energy or the energy fluctuation is observed.

6.2 Future Work

The development and use of the instrumented ball have provided another tool for the measurement of mill states. Furthermore, its application, within a sensor suite, provided the basis for an analysis, which adopted a thermodynamics-based formalism. These findings lead to a number of open tasks, which may be the subject of further research.

1. Adding Capabilities to the Sensor System: The sensors used to measure the mill states can be expanded. This includes the addition of the wear sensor to the instrumented ball [RML⁺06], the use of the acoustic sensors as part of the measurement set [HMR⁺on], or the coupling of the instrumented ball to the X-ray or PEPT measurement systems [BGC⁺09, MGPC04]. Also, the inclusion, within the analysis methodology, of all the sensors currently on the instrumented ball—the accelerometer and the temperature sensor—is a step to be taken.
2. Distributions, Entropy and State Diagrams: The determination of the entropy of the mill was an approximation. A more precise way of estimating the entropy must be found. The expansion of this thermodynamics-inspired analysis, through the development of a free energy and an effective temperature, could be the basis of an alternative description of the mill. Also, the search for critical behavior must continue. Perhaps the use of an autocorrelation function may aid in this task[Yeo92]. The result of this work may be a state diagram of the

mill, analogous to the phase diagrams of materials. Finally, the identification of the nature of the distributions is needed, as it provides some clues as to the nature of the dynamics.

3. Pilot Mills: The use of the instrumented ball within a larger, industrial mill is of interest. To accomplish this, a modified shell, capable of protecting the electronics as the instrument evolves within a pilot mill must be constructed. A ball in contact with the mill shell can spin at speeds greater than the maximum rate the sensor can measure. Therefore, prior to pilot mill tests, it may be necessary to find a sensor with a higher range.
4. Measurement Sets: The construction of measurement databases based on different mill fills, mill speeds, mill charge composition and mill configurations (two and three dimensional mill configurations) is another task to be completed. By doing so, a number of DEM results, such as the entropy, can be *experimentally* verified. Furthermore, the collection of more samples, for given mill configurations, will help reduce the experimental errors.
5. *In-Situ* and *In-Silico* Comparison: The application of the present methodology, with an expanded measurand set, to different DEM models, will permit the comparison of DEM accuracies by assigning model order to each DEM. The compilation of model orders will effectively build a list of DEM accuracies, giving other users the ability to quickly evaluate models. Also, the drive to improve the model accuracy will require the addition of more measurands to the *in-situ* and *in-silico* comparison, such as the position of the center of circulation, the toe and shoulder positions, critical points, and the higher order

moments of the distributions. Finally, with the addition of temperature to the measurand set, the DEMs will require more thermal development if it is to account for any observed changes in temperature.

References

- [Ach00] Amit Acharya. Distinct element approach to ball mill mechanics. *Communications in Numerical Methods in Engineering*, 16(11):743–753, 2000.
- [Ano90] Anonymous. Reportage. *Powder Magazine*, 114(10):615, 1990.
- [Aus01] L. G. Austin. Measurement of impact forces in ball mills: a reanalysis. *Minerals & Metallurgical Processing*, 18(4):228–230, November 2001.
- [Bam00] B. Bamjanović, editor. *Canadian Mining Practice*. Canadian Institute of Mining, Metallurgy and Petroleum, 2000.
- [BGC⁺09] A. Buffler, I. Govender, J.J. Cilliers, D.J. Parker, J-P. Franzidis, A. Mainza, R.T. Newman, M. Powell, and A. van der Westhuizen. PEPT Cape Town: a new positron emission particle tracking facility at iThemba LABS. In *International Topical Meeting on Nuclear Research Applications and Utilization of Accelerators*, Vienna, 2009.
- [Bir07] Giulio Biroli. Jamming: a new kind of phase transition? *Nature Physics*, 3(4):222–223, April 2007.
- [CAR⁺06] S. Caron, C. Arekar, D. Roy, P. Radziszewski, I. Orford, and A. Faucher. Sag-tools – an on-line system for monitoring charge characteristics in grinding mills. In M.J. Allan, K. Major, B.C. Flintoff, B. Klein, and A.L. Mular, editors, *International Autogenous and Semi-autogenous Grinding Technology 2006*, volume III, pages 283–299, Vancouver, Canada, 2006.
- [CBBW⁺02] J. Conway-Baker, R. W. Barley, R. A. Williams, X. Ji, J. Kostuch, B. McLoughlin, and D. J. Parker. Measurement of the motion of grinding media in a vertically stirred mill using positron emission particle tracking (PEPT). *Minerals Engineering*, 15(1-2):53–59, 2002.

- [Che07] Tapiwanashe Chenje. *Development and Validation of a Model for Steel Grinding Media Wear in Tumbling Mills*. PhD thesis, McGill University, Department of Mechanical Engineering 816 Sherbrooke Street West Montreal, Quebec, H3A 2K6 Canada, 2007.
- [Chu01] Kai Lai Chung. *A Course in Probability Theory*. Academic Press, San Diego, 3rd edition, 2001.
- [Cle98] P.W. Cleary. Predicting charge motion, power draw, segregation and wear in ball mills using discrete element methods. *Minerals Engineering*, 11(11):1061–1080, 1998.
- [Cle01a] Paul Cleary. Modelling comminution devices using DEM. *International Journal for Numerical and Analytical Methods in Geomechanics*, 25(1):83–105, 2001.
- [Cle01b] Paul W. Cleary. Charge behaviour and power consumption in ball mills: sensitivity to mill operating conditions, liner geometry and charge composition. *International Journal of Mineral Processing*, 63(2):79–114, august 2001.
- [Cle04] Paul W. Cleary. Large scale industrial DEM modelling. *Engineering Computations*, 21(2/3/4):169–204, 2004.
- [CMM03] Paul W. Cleary, Rob Morrisson, and Steve Morrell. Comparison of DEM and experiment for a scale model SAG mill. *International Journal of Mineral Processing*, 68(1-4):129–165, 2003.
- [CR04] S. Caron and D. Roy. Projet R006 Développement d’Indicateurs en Ligne du Comportement de la Charge dans les Broyeurs. Rapport d’Étape : Revue de la Litterature, COREM, 1180, rue de la Minéralogie, Québec (Québec) G1N 1X7 Canada, March 2004.
- [CS79] P. A. Cundall and O. D. L. Strack. A discrete numerical model for granular assemblies. *Geotechnique*, 29:47–65, 1979.
- [Dav19] E.W. Davis. Fine crushing in ball mills. *Transactions of American Institute of Mining and Metallurgy*, 61:250–296, 1919.
- [DDT07] Francesco Paolo Di Maio, Alberto Di Renzo, and Daniela Trevisan. Comparison of heat transfer approaches at the particle scale in fluidized

- beds. In *4th International Conference DEM 2007*, Brisbane, Australia, 2007.
- [DEM09] DEM Solutions, 24 Hanover Street, Suite 10, Lebanon, New Hampshire, 03766, USA. *DEM Solutions Training: Introducing DEM & EDEM*, 2nd edition, 2009.
- [DM78] D.J. Dunn and R.G. Martin. Measurement of impact force in ball mills. *Mining Engineering*, 30(4):384–388, April 1978.
- [DM01] H. Dong and M.H. Moys. A technique to measure velocities of a ball moving in a tumbling mill and its applications. *Minerals Engineering*, 14(8):841–850, 2001.
- [DM03] H. Dong and M.H. Moys. Load behavior and mill power. *International Journal of Mineral Processing*, 69(1-4):11–28, 2003.
- [EO89] S. F. Edwards and R. B. S. Oakeshott. Theory of powders. *Physica A*, 157:1080–1090, 1989.
- [FA02] D.W. Fuerstenau and A.-Z.M. Abouzeid. The energy efficiency of ball milling in comminution. *International Journal of Mineral Processing*, 67(1-4):161–185, 2002.
- [FBM⁺06] T. Freeth, Y. Bitsakis, X. Moussas, J. H. Seiradakis, A. Tselikas, H. Mangou, M. Zafeiropoulou, R. Hadland, D. Bate, A. Ramsey, M. Allen, A. Crawley, P. Hockley, T. Malzbender, D. Gelb, W. Ambrisco, and M. G. Edmunds. Decoding the ancient greek astronomical calculator known as the antikythera mechanism. *Nature*, 444:587–591, 2006.
- [Fer01] Jean-Albert Ferrez. *Dynamic Triangulations for Efficient 3D Simulation of Granular Materials*. PhD thesis, École Polytechnique Fédérale de Lausanne, 2001.
- [FH03] M. Fuerstenau and K. Han, editors. *Principles of Mineral Processing*. Society for Mining, Metallurgy, and Exploration, Inc., Littleton, Colorado, 2003.
- [FHO07] Y. T. Feng, K. Han, and D. R. J. Owen. Discrete thermal element modelling of heat conduction in particulate systems. In *4th International Conference on DEM*, 2007.

- [FKV90] D. W. Fuerstenau, P. C. Kapur, and B. Velamakanni. A multi-torque model for the effects of dispersants and slurry viscosity on ball milling. *International Journal of Mineral Processing*, 28(1-2):81–98, February 1990.
- [FLFC98] E. Falcon, C. Laroche, S. Fauve, and C. Coste. Behavior of one inelastic ball bouncing repeatedly off the ground. *European Physical Journal B*, 3(1):45–57, 1998.
- [FM04] Klebert Feitosa and Narayanan Menon. Fluidized granular medium as an instance of the fluctuation theorem. *Physical Review Letters*, 92(16):164301, 2004.
- [FW87] J.E. Freund and R.E. Walpole. *Mathematical Statistics*. Prentice-Hall, Englewood Cliffs, N.J., 4th edition, 1987.
- [GMP04] I. Govender, A.T. McBride, and M.S. Powell. Improved experimental tracking techniques for validating discrete element method simulations of tumbling mills. *Experimental Mechanics*, 44(6):593–607, December 2004.
- [GPN01] I. Govender, M.S. Powell, and G.N. Nurick. 3D particle tracking in a mill: a rigorous technique for verifying dem predictions. *Minerals Engineering*, 14(10):1329 – 1340, 2001.
- [Gre01] C. E. Gregory. *A Concise History of Mining (Revised Edition)*. A.A. Balkema Publishers, Lisse, The Netherlands, 2001.
- [GT94] R. X. Gao and W. Thelen. Sensor-integrated grinding balls for on-line load distribution measurement in ball mills. *Proceedings of the Institution of Mechanical Engineers. Part B. Journal of Engineering Manufacture*, 208(3):183–190, 1994.
- [GY06] A. Gupta and D.S. Yan. *Mineral Processing Design and Operation, an Introduction*. Elsevier, Amsterdam, 2006.
- [Hab06] F. Habashi. A short history of mineral processing. In *Proceedings XXIII International Mineral Processing Congress*, volume 1, pages 3–8, Istanbul, 2006.

- [Har92] Howard Hartman, editor. *SME Mining Engineering Handbook*. Society for Mining, Metallurgy, and Exploration, Littleton, Colorado, 2nd edition, 1992.
- [Her93] H. J. Herrmann. On the thermodynamics of granular media. *J. Phys. II France*, 3(4):427–433, 1993.
- [HMR⁺on] Poorya Hossein, Sudarshan Martins, Peter Radziszewski, Arnaud Faucher, and Sami Makni. Simulation of emitted acoustic signal of tumbling mills based on charge dynamics. in preparation.
- [Hua87] Kerson Huang. *Statistical Mechanics*. John Wiley & Sons, 2nd edition, 1987.
- [HV86] D.D. Howat and L.A. Vermeulen. The design of linings for rotary mills: a major factor in the throughput and consumption of energy and metal. *Journal of the South African Institute of Mining and Metallurgy*, 86(7):251–259, 1986.
- [Ita03] Itasca Consulting Group, Inc., Minneapolis, USA. *PFC3D Theory and Background, 2ed.*, 2003.
- [Jon06] Stuart M. Jones, Jr. Autogenous and semiautogenous mills 2005 update. In M.J. Allan, K. Major, B.C. Flintoff, B. Klein, and A.L. Mular, editors, *International Autogenous and Semiautogenous Grinding Technology 2006*, volume I, pages 398–425, Vancouver, Canada, September 2006.
- [Kap90] E. Kaptan. Findings related to the history of mining in turkey. *Bulletin of the Mineral Research and Exploration*, 111:75–84, 1990.
- [KESR⁺07] H. Kruggel-Emden, E. Simsek, S. Rickelt, S. Wirtz, and V. Scherer. Review and extension of normal force models for the discrete element method. *Powder Technology*, 171:157 – 173, 2007.
- [KESWS07] H. Kruggel-Emden, E. Simsek, S. Wirtz, and V. Scherer. A comparison and validation of tangential force models for use within discrete element simulations. In *Proceedings of Discrete Element Methods 07 (CD-ROM)*. MEI Online, August 2007.
- [KH74] H. Kinder and W. Hilgemann. *The Anchor Atlas of World History*, volume 1. Doubleday, 1974.

- [Kre10] David E. Kretschmann. *Wood Handbook - Wood as an Engineering Material*, chapter 5: Mechanical Properties of Wood, pages 5-1 – 5-46. General Technical Report FPL-GTR-190. U.S. Department of Agriculture, Forest Service, Forest Products Laboratory, Madison, WI, 2010.
- [Li04] W. Li. Instrumented ball development report. Technical report, McGill University, October 2004.
- [LLC99] CRC Press LLC. CRC handbook of chemistry and physics (online). McGill Online Resource, 1999.
- [LR05] Alban J. Lynch and Chester A. Rowland. *The History of Grinding*. Society for Mining Metallurgy & Exploration, 8307 Shaffer Parkway, Littleton, Colorado, 2005.
- [MC99] Anil Misra and Josephine Cheung. Particle motion and energy distribution in tumbling ball mills. *Powder Technology*, 105(1-3):222 – 227, 1999.
- [McI83] R.E. McIvor. The effect of speed and liner configuration on ball mill performance. *Mining Engineering*, 35(6):617–622, 1983.
- [MGPC04] Andrew McBride, Indresan Govender, Malcolm Powell, and Trevor Cloete. Contributions to the experimental validation of the discrete element method applied to tumbling mills. *Engineering Computations*, 21(2/3/4):119–136, 2004.
- [Mis03] B.K. Mishra. A review of computer simulation of tumbling mills by the discrete element method part II - practical applications. *International Journal of Mineral Processing*, 71:95–112, 2003.
- [MLR⁺08] Sudarshan Martins, Wei Li, Peter Radziszewski, Sylvain Caron, Marc Aguanno, Michael Bakhos, and Emma Lee Petch. Validating the instrumented ball outputs with simple trajectories. *Minerals Engineering*, 21(11):782–788, October 2008.
- [MLRC06a] S. Martins, W. Li, P. Radziszewski, and S. Caron. Instrumented ball development and use. In M.J. Allan, K. Major, B.C. Flintoff, B. Klein, and A.L. Mular, editors, *International Autogenous and Semiautogenous Grinding Technology 2006*, volume I, pages 265–277, Vancouver, Canada, 2006.

- [MLRC06b] S. Martins, W. Li, P. Radziszewski, and S. Caron. Investigating on-the-shell acoustics. In M.J. Allan, K. Major, B.C. Flintoff, B. Klein, and A.L. Mular, editors, *International Autogenous and Semiautogenous Grinding Technology 2006*, volume III, pages 265–277, Vancouver, Canada, 2006.
- [MLRC07] Sudarshan Martins, Wei Li, Peter Radziszewski, and Sylvain Caron. Investigating the differences in charge dynamics due to a variation of the instrumented ball properties. In Claude Bazin, Carl Duchesne, and ric Poulin, editors, *IFAC MMM '07 on Automation in Mining, Mineral and Metal Processing*, pages 463–468, Quebec City, Canada, August 2007.
- [MNB08] Joseph V. Michalowicz, Jonathan M. Nichols, and Frank Bucholtz. Calculation of differential entropy for a mixed gaussian distribution. *Entropy*, 10:200–206, 2008.
- [Mor84] L. Morris. Derek de Solla Price and the Antikythera Mechanism: an appreciation. *IEEE Micro*, 4(1):15–21, Jan/Feb 1984.
- [MPF⁺08] S. Martins, B. Picard, A. Faucher, S. Makni, W. Li, P. Radziszewski, and S. Caron. Instrumented disk dynamics in a 2d tumbling mill. In *Proceedings of the XXIV International Mineral Processing Congress*, volume 2, pages 2448–2457, Beijing, China, September 2008.
- [MR92] B.K. Mishra and Raj K. Rajamani. The discrete element method for the simulation of ball mills. *Applied Mathematical Modelling*, 16(11):598 – 604, 1992.
- [MR94a] B.K. Mishra and Raj K. Rajamai. Simulation of charge motion in ball mills. part 2: numerical simulations. *International Journal of Mineral Processing*, 40:187–197, 1994.
- [MR94b] B.K. Mishra and R. K. Rajamani. Simulation of charge motion in ball mills. part 1: experimental verifications. *International Journal of Mineral Processing*, 40:171–186, 1994.
- [MRdR⁺09] Sean McNamara, Patrick Richard, Sébastien Kiesgen de Richter, Gérard Le Caër, and Renaud Delannay. Measurement of granular entropy. *Physical Review E*, 80(3):031301, September 2009.

- [MRP⁺07] S. Martins, P. Radziszewski, B. Picard, M. Brochu, and U. Seminari. Exploring the feasibility of using a commercial hardware and software physics engine for milling system simulation. In *4th International Conference DEM 2007*, Brisbane, Australia, 2007.
- [MT61] K. G. McLaren and D. Tabor. The frictional properties of lignum vitae. *British Journal of Applied Physics*, 12:118–120, 1961.
- [MX08] Kevin Francis Malone and Bao Hua Xu. Determination of contact parameters for discrete element method simulations of granular systems. *Particuology*, 6:521–528, 2008.
- [MZP⁺06] S. Martins, J. Zepeda, B. Picard, P. Radziszewski, and D. Roy. Investigating on-the-shell acoustics. In M.J. Allan, K. Major, B.C. Flintoff, B. Klein, and A.L. Mular, editors, *International Autogenous and Semi-autogenous Grinding Technology 2006*, volume III, pages 300–310, Vancouver, Canada, 2006.
- [PHSP07] Alexander V. Potapov, John A. Herbst, Ming Song, and William T. Pate. A dem-pbm fast breakage model for simulation of comminution processes. In *4th International Conference on DEM*, Brisbane, Australia, 2007.
- [Piced] Benoit Picard. *Tumbling Mill Charge Motion Slippage Relationship Study*. PhD thesis, McGill University, Department of Mechanical Engineering 816 Sherbrooke Street West Montreal, Quebec, H3A 2K6 Canada, unpublished.
- [PM04] M.S. Powell and A.T. McBride. A three-dimensional analysis of media motion and grinding regions in mills. *Minerals Engineering*, 17:1099–1109, 2004.
- [PM05] A. Pérez-Madrid. Generalized gibbs entropy, irreversibility and stationary states. *Int. J. of Thermodynamics*, 8(4):159–166, Decemeber 2005.
- [PN96] M.S. Powell and G.N. Nurick. A study of charge motion in rotary mills part 2 - experimental work. *Minerals Engineering*, 9(3):343–350, 1996.
- [Pra87] C. L. Prasher. *Crushing and Grinding Process Handbook*. John Wiley & Sons Inc, New York, 1987.

- [Rab95] E Rabinowicz. *Friction and Wear of Materials*. Wiley, 1995.
- [Rad86] P. Radziszewski. Modélisation de la Comminution en Fonction du Concassage, du Cascadage et du Broyage dans un Broyeur Boulets. Master's thesis, Université Laval, 1986.
- [Rad97] P. Radziszewski. Predictive model for ball mill wear. *Canadian Metallurgical Quarterly*, 36(2):87–93, 1997.
- [Rad99] P. Radziszewski. Comparing three DEM charge motion models. *Minerals Engineering*, 12(12):1501–1520, 1999.
- [Rag07] D. Ragland. *Impactograph - Deter and Detect In-Transit Damage*. Impactograph Division, Chatsworth Data Corporation, 20710 Lassen Street, Chatsworth CA, May 2007.
- [Raj07] R. Rajamani. Private communication (DEM'07, Brisbane, Australia). At the conference, Rajamani discussed some of the problems he had with the instrumented ball, September 2007.
- [RBL⁺05] Raj. K. Rajamani, B.K.Mishra, Sanjeeva Latchrieddi, T.N. Patra, and Sravan K Prathy. On the dynamics of charge motion in grinding mills. In J. D. Miller, Courtney Young, Jon J Kellar, Michael L. Free, Jaroslaw Drelich, and R. P. King, editors, *Innovations in Natural Resource Processing - Proceedings of the Jan. D. Miller Symposium*, pages 383–394. SME, 2005.
- [RC04] P. Radziszewski and S. Caron. Towards AG/SAG/ball mill on-line performance monitoring. *CIM Bulletin*, 97(1084):74–78, November/December 2004.
- [RDD06] R. Rajamani, J. Delgadillo, and V. Duriseti. Online SAG mill pulse measurement and optimization semiannual technical progress report. Technical Report FC26-04NT42088, United States Department of Energy, November 2006.
- [RGT06] Peter Radziszewski, Lei Geng, and Ryan Tomicic. A mechanical alternative to the gearless drive? The cam drive. In M.J. Allan, K. Major, B.C. Flintoff, B. Klein, and A.L. Mular, editors, *International Autogenous and Semiautogenous Grinding Technology 2006*, volume II, pages 99–108, Vancouver, Canada, 2006.

- [RH98] M. H. Rheinfurth and L. W. Howell. Probability and statistics in aerospace engineering. Technical Report NASA/TP-1998-207194, National Aeronautics and Space Administration (George C. Marshall Space flight Center), Washington, DC, March 1998.
- [RM98] P. Radziszewski and S. Morrell. Fundamental discrete element charge motion model validation. *Minerals Engineering*, 11(12):1161–1178, 1998.
- [RML⁺06] P. Radziszewski, S. Martins, W. Li, B. Picard, Y. Quan, and S. Caron. Investigating the feasibility of liner wear sensor development. In M.J. Allan, K. Major, B.C. Flintoff, B. Klein, and A.L. Mular, editors, *International Autogenous and Semiautogenous Grinding Technology 2006*, volume III, pages 149–159, Vancouver, Canada, 2006.
- [RMVD00] R.K. Rajamani, B.K. Mishra, R. Venugopal, and A. Datta. Discrete element analysis of tumbling mills. *Powder Technology*, 109:105–112, 2000.
- [Rol99] L. Rolf. Instrumentierung von mahlkugeln zur ermittlung der energieverteilungen in kugelmühlen. *Chemische Technik*, 51(5):238–240, 1999.
- [RS58] H. E. Rose and R. M. E. Sullivan. *A treatise on the internal mechanics of ball, tube, and rod mills*. Chemical Publishing Co., New York, 1958.
- [RS90] L. Rolf and W. Simonis. Energy distribution in ball mills. In *Preprint of 7th European Symposium on Comminution*, pages 543 – 554, 1990.
- [RV83] L. Rolf and T. Vongluekiet. Ermittlung der energieverteilungen in kugelmühlen. *Chemie Ingenieur Technik*, 55(10):800–801, 1983.
- [RV84] L. Rolf and T. Vongluekiet. Measurement of energy distribution in ball mills. *German Chemical Engineering Journal*, 7:287–292, 1984.
- [SKSM05] Kai Sundmacher, Achim Kienle, and Andreas Seidel-Morgenstern. *Integrated Chemical Processes Synthesis, Operation, Analysis, and Control*. John Wiley & Sons, 2005.
- [SMM89] Raymond A. Serway, Clement J. Moses, and Curt A. Moyer. *Modern Physics*. Saunders College Publishing, 1989.

- [Tec08] Teck Cominco Limited. *Teck Cominco 2007 Annual Report*. 600-200 Burrard Street, Vancouver, British Columbia, Canada V6C 3L9, 2008.
- [The08] The McGraw-Hill Companies, Inc. Pebble mill. *McGraw-Hill Encyclopedia of Science and Technology* (<http://www.answers.com/topic/pebble-mill>), April 2008.
- [TR90] Stanislaw Tarasiewicz and Peter Radziszewski. Grinding process simulation in a ballmill. *Mathematical and Computer Modelling*, 14:1072–1074, 1990.
- [Tro08] Desmond Tromans. Mineral comminution: energy efficiency considerations. *Minerals Engineering*, 21:613–620, 2008.
- [VCVQ⁺98] B. C. Vemuri, L. Chen, L. Vu-Quoc, X. Zhang, and O. Walton. Efficient and accurate collision detection for granular flow simulation. *Graphical Models and Image Processing*, 60:403 – 422, 1998.
- [VR01] R. Venugopal and R.K. Rajamani. 3D simulation of charge motion in tumbling mills by the discrete element method. *Powder Technology*, 115:157–166, 2001.
- [VW91] T.J. Veasey and B.A. Wills. Review of methods of improving mineral liberation. *Minerals Engineering*, 4(7-11):747–752, 1991.
- [Wat99] Hiroshi Watanabe. Critical rotation speed for ball-milling. *Powder Technology*, 104:95–99, 1999.
- [Wil97] B. A. Wills. *Mineral Processing Technology, an Introduction to the Practical Aspects of Ore Treatment and Mineral Recovery, 6th. Edition*. Butterworth-Heinemann, 1997.
- [Wri07] M. T. Wright. The Antikythera Mechanism reconsidered. *Interdisciplinary Science Reviews*, 32(1):27–43, 2007.
- [WS08] Carl Wassgren and Avik Sarkar. *Discrete Element Method (DEM) Course Module*. <https://pharmahub.org/resources/113>, December 2008.
- [Yeo92] J. M. Yeomans. *Statistical Mechanics of Phase Transitions*. Oxford University Press, 1992.

- [YYMB08] R.Y. Yang, A.B. Yu, L. McElroy, and J. Bao. Numerical simulation of particle dynamics in different flow regimes in a rotating drum. *Powder Technology*, 188:170–177, 2008.
- [ZZRA08] H.P. Zhu, Z.Y. Zhou, R.Y. Yang, and A.B. Yu. Discrete particle simulation of particulate systems: a review of major applications and findings. *Chemical Engineering Science*, 63:5728–5770, 2008.
- [ZZYY07] H.P. Zhu, Z.Y. Zhou, R.Y. Yang, and A.B. Yu. Discrete particle simulation of particulate systems: theoretical developments. *Chemical Engineering Science*, 62:3378–3396, 2007.